UC San Diego
UC San Diego Electronic Theses and Dissertations

Title
Nitride semiconductor Surface and interface characterization and device design

Permalink
https://escholarship.org/uc/item/5z94j969

Author
Zhang, Hongtao

Publication Date
2006

Peer reviewed|Thesis/dissertation

eScholarship.org Powered by the California Digital Library
University of California

UNIVERSITY OF CALIFORNIA, SAN DIEGO

Nitride Semiconductor Surface and Interface Characterization and Device Design

A dissertation submitted in partial satisfaction of the requirements for the degree of

Doctor of Philosophy

in

Electrical Engineering (Applied Physics)

by

Hongtao Zhang

Committee in charge:

Professor Edward T. Yu, Chair
Professor Peter M. Asbeck
Professor Andrew C. Kummel
Professor S. S. Lau
Professor Vitali F. Nesterenko

2006

Copyright

Hongtao Zhang, 2006

All rights reserved.

The dissertation of Hongtao Zhang is approved, and it is

accepted in quality and form for publication on microfilm:

____

____

____

____

____

Chair

University of California, San Diego

2006

To my family

TABLE OF CONTENTS

Signature Page……………………………………………………………………iii

Dedication……………………………………………………………………........iv

Table of Contents……………………………………………………………………..v

List of Abbreviations and Symbols…………...………………………………….....viii

List of Figures and Tables……….…………………………………………………..ix

Acknowledgements……………………………………………………………….xii

Vita…………………………………………………………………………………..xiv

Abstract………………………………………………………………………….....xvi

1. **Introduction**…...…………………………………………………………………..1

1.1 Motivation and Background.....………………………………………..……..…1

1.2 Thesis Organization....……………………………………………...……4

2. **Capacitance-Voltage (C-V) Measurement of Polarization Charge Density and Conduction Band-offset at GaN/$In_yGa_{1-y}N$ Heterojunction Interface**...............6

2.1 Introduction….………………………………………………………………....6

2.1.1. Motivation and Outline………………………………..…………….6

2.1.2. Polarization Charges and Band Offsets for Nitrides Semiconductors....7

2.2 Experiment Techniques….……………………………………………………11

2.2.1 General Description of Capacitance Voltage Profiling Techniques...11

2.2.2 Improvement on Band-offset Calculation.……………………….....14

2.2.3 Heterostructure Design and Nitride Growth………………………….15

2.3 Schottky Diode Fabrication, C-V Measurement and Schottky Diode Modeling……………………...17

2.3.1 Schottky Diode Fabrication on n-type GaN…………………………..17

2.3.2 Leakage Current Blockade Prior to C-V Measurement………………18

2.3.3 C-V Measurement and Comprehensive Schottky Diode Modeling…..19

2.4 Experiment Results and Discussion……………………………………..22

2.4.1 C-V Measurement Results………………………………………………22

2.4.2 Results and Discussion on Polarization Charge Density……………..24

2.4.3 Results and Discussion on Conduction Band Offset……….………28

2.5 Conclusion……..………………………………………………………….30

3. **Analysis of Leakage Current Mechanisms in Schottky Contacts to GaN and $Al_{0.25}Ga_{0.75}N$/GaN Grown by Molecular-Beam Epitaxy**………………………32

3.1 Introduction……………………………………………………………...32

3.2 Experiment Description…………………………………………………33

3.3 Results and Discussion…….…………………………………………….35

3.3.1 Low Temperature Behavior….…………………………………….35

3.3.2 Room and High Temperature Behavior….……………………………...39

3.4 Conclusion………………………………………………………………47

4. **Demonstration and Analysis of Reduced Reverse-bias Leakage Current Via Design of Nitride Semiconductor Heterostructures Grown by Molecular-Beam Epitaxy**…...49

4.1 Motivation……..………………………………………………………...49

4.2 Experiment Description…..……………………………………………..51

4.3 Results and Discussion…...……………………………………………...53

4.3.1 Macroscopic Demonstration and Explanations…...…………………..53

4.3.2 Microscopic Demonstration and Explanations...........................60

4.4 Conclusion...64

5. **Conclusion**..66

Appendix—Negative Index Material Application, Fabrication and Characterization......69

A.1 Introduction...69

A.2 Possible Application of Negative Index Material (NIM) in Cavity Resonator.......70

A.2.1 Review: 1-D DPS-DNG Cavity..71

A.2.2 3D DPS-DNG Cascaded Structure.......................................75

A.2.3 3D Partially Loaded Resonant Structure...............................78

A.2.4 Mixed Double DPS-DNG 3-D Resonator...................................80

A.2.5 Summary—Resonator Analysis...82

A.3 Negative Index Material Design, Fabrication and Characterization...........83

A3.1 Design of Single Split Ring With Overlapped Arms Structure.............83

A3.2 Electroplating Fabrication...88

A3.3 Proposed Characterization Method.......................................93

A.4 Conclusion...98

References..100

LIST OF ABBREVIATIONS AND SYMBOLS

2DEG	Two Dimensional Electron Gas
AFM	Atomic Force Microscopy
C-AFM	Conductive Atomic Force Microscopy
C-V	Capacitance-Voltage
DH	Double Heterojunction
DNG	Double Negative
DPS	Double Positive
DSR	Double Split Ring
DUT	Device Under Test
EM	Electromagnetic
HFET	Heterojunction Field Effect Transistor
HEMT	High Electron Mobility Transistor
HFSS	High-Frequency Structure Simulator
LED	Light Emitting Diodes
LH	Left Handed
MOCVD	Metal-Organic Chemical Vapor Deposition
MBE	Molecular Beam Epitaxy
M-S	Metal-Semiconductor
NIM	Negative Index Material
SSROA	Single Split Ring with Overlapped Arms
SR	Split Ring
TL	Transmission Line

LIST OF FIGURES AND TABLES

Fig. 2.1 Crystal structure, spontaneous polarization and piezoelectric polarization for GaN/$In_yGa_{1-y}N$ heterojunction. The structure is coherently stained to GaN (0001).......9

Fig. 2.2 Schematic diagram of the GaN/$In_yGa_{1-y}N$/GaN epitaxial layer structure and the corresponding equivalent circuit models used in this study. The silicon oxide layer as present only for the y=0.09 sample to reduce the leakage current. There is no oxide on y=0.054 sample because the leakage current is small enough for the measurement. The two element parallel model was assumed during the measurement but was later corrected using the three element model to remove the series resistance effect r_s……………………………………………………………………………………16

Fig. 2.3 Measured C_p and the derived capacitance C after consideration of the effect of series resistance r_s for GaN/$In_{0.09}Ga_{0.91}N$/GaN (top diagram) and for GaN/$In_{0.054}Ga_{0.946}N$/GaN (bottom diagram)…………………………………………21

Fig. 2.4 Apparent carrier concentration profiles (a) for the $In_{0.09}Ga_{0.91}N$/GaN heterostructure, derived from C-V data obtained at frequencies of 100 kHz (■), 450 kHz (♦), and 800 kHz (▲) (top diagram) and (b) for the $In_{0.054}Ga_{0.946}N$/GaN heterostructure, derived from C-V data obtained at frequencies of 300 kHz (■), 600 kHz (♦), and 1 MHz (▲) (bottom diagram)....………………………………………..23

Fig. 2.5 Simulated band structure and electric field for Ref. 37. The indium content is 16% and the assumed polarization charge density is 9.0×10^{12} e/cm^2. The electric field thus deduced is about 1.2 MV/cm.…………………..…………………….........25

Fig. 2.6 $In_yGa_{1-y}N$/GaN polarization charge densities from this work (■), and inferred from Ref. 36 (▲), Ref. 37 (●), Ref. 38 (▼), Ref. 39 (Δ), Ref. 40 (□) and Ref. 41 (○). Calculated polarization charge densities (Ref. 7) are also shown in a straight line......26

Fig. 2.7 Reported values (from Ref. 7 (Δ), Ref. 45 (○) and Ref. 48 (∇)) and our measured values (■) for ΔE_C for the $In_yGa_{1-y}N$/GaN heterojunction....……….............29

Fig. 3.1 Current density vs. bias voltage for Schottky diodes fabricated on (a) GaN and (b) $Al_{0.25}Ga_{0.75}N$/GaN HFET epitaxial layer structures, for temperatures ranging from 110K to 400K. At low temperatures (T<150 K), leakage currents are independent of temperature and the J-V curves overlap each other……...………………………37

Fig. 3.2 Measured current density divided by the square of the electric field v. inverse electric field for Schottky diodes fabricated on (a) GaN and (b) $Al_{0.25}Ga_{0.75}N$/GaN HFET epitaxial layer structures, for temperatures ranging from 110K to 150K. The straight line fitting demonstrates that at low temperatures (T<150 K), leakage current follows the Fowler-Nordheim model…………………………………………………38

Fig. 3.3 (a) Topographic and (b) current images of the $Al_{0.25}Ga_{0.75}N$/GaN HFET structure, obtained by conductive AFM……………………………………………40

Fig. 3.4 Measured current density divided by the electric field v. square root of electric field, for Schottky diodes fabricated on (a) GaN and (b) $Al_{0.25}Ga_{0.75}N$/GaN HFET epitaxial layer structures, for temperatures ranging from 250K to 400K……..41

Fig. 3.5 Slopes $m(T)$ of the curves shown in (a) for GaN, and (b) for $Al_{0.25}Ga_{0.75}N$/GaN. Intercepts $b(T)$ of the curves shown in (c) for GaN, and (d) for $Al_{0.25}Ga_{0.75}N$/GaN. Data from curves not shown in Fig. 3.4 are also included……...43

Fig. 3.6 Energy band diagram showing conduction- and valence-band-edge energies and postulated trap-state and dislocation-state energies for GaN and $Al_{0.25}Ga_{0.75}N$ based on measured emission barrier heights and reported Schottky barrier heights and band offsets…………………………………………………………………...46

Fig. 4.1 Epitaxial layer structure and schematic energy-band-edge diagram for (a) conventional $Al_{0.25}Ga_{0.75}N$/GaN HFET structure, and (b) GaN/$Al_{0.25}Ga_{0.75}N$/GaN HFET structure incorporating a GaN cap layer. The two structures have the same Al content, almost identical barrier thickness and doping……………………………52

Fig. 4.2 Reverse-bias current-voltage characteristics at temperatures ranging from 250K to 400K for (a) conventional $Al_{0.25}Ga_{0.75}N$/GaN HFET structure, and (b) GaN/$Al_{0.25}Ga_{0.75}N$/GaN HFET structure incorporating a GaN cap layer. Leakage currents in GaN-capped HFET structure are reduced by approximately 3 to 4 orders of magnitude and the reduction is most prominent at biases between 0 V and -4 V…....54

Fig. 4.3 (a) Conduction-band-edge energy profile for the GaN-capped HFET structure at bias voltages of 0V, -2V, and -4V. (b) Electron sheet concentration in the channel of the conventional and GaN-capped HFET structures, as functions of bias voltage. (c) Vertical electric field at the metal-semiconductor Schottky interface of the conventional and GaN-capped HFET structures, as functions of bias voltage……....57

Fig. 4.4 Current density as a function of inverse temperature for the GaN-capped HFET structure at bias voltages of (a) -8V and (b) -3V……………………….......59

Fig. 4.5 Topographic (left) and current (right) images of conventional and GaN-capped HFET structures obtained via conductive atomic force microscopy. (a) conventional HFET structure at -8V bias. (b) conventional HFET structure at -12V bias. (c) GaN-capped HFET structure at -8V bias. (d) GaN-capped HFET structure at -12V bias………………………………………………………………………61

Fig. A.2.1 1-D DPS-DNG resonant structure……………………………………...71

Fig. A.2.2 Total thickness d vs. DPS layer thickness d_1 for 1D DPS-DNG resonator structure. Large negative n_2 reduces system size……………………………………..73

Fig. A.2.3 3-D cascaded DPS-DNG resonant cavity……………………………75

Fig. A.2.4 H-field distribution in x-z plane for 3D cascaded structure when (a) $k_{z1}d_1>\pi/2$; (b) $k_{z1}d_1=\pi/2$; (c) $k_{z1}d_1<\pi/2$……………………………………………...77

Fig. A.2.5 3-D partially-loaded DPS-DNG resonant cavity……………………….78

Fig. A.2.6. 3-D mixed double DPS-DNG resonant cavity…………………………81

Fig. A.3.1 Equivalent *LCR* resonant circuit for split ring……………………………83

Fig. A.3.2 Structure of single split ring with overlapped arms (SSROA)…………..84

Fig. A.3.3 Top view and front view of the SSROM arrays on planar structure…..87

Fig. A.3.4a Electroplated Au (magnification: 10X), with a=60 µm, b=360 µm, d=20 µm, h= 20 µm, and L_a=600 µm; A.3.4b electroplated Ni (magnification: 50X) with a=30 µm, b=180 µm, d=10 µm, h= 10 µm, and L_a=250 µm…………………………92

Fig. A.3.5 The fundamental limit on D is when Δx=D/2……………………………93

Fig. A.3.6 Reflection of s-wave and p-wave by planar structure………………….94

Fig. A.3.7 Schematic plot of multireflection at each interfaces……………………97

Table A.3.1 Electroplating conditions and measured results……………………….91

ACKNOWLEDGMENTS

First, I would like to thank my advisor, Professor Edward Yu, for his continued encouragement, guidance and support all through the years. His insightful judgment is very important to my completion of the research work. I would also like to thank other professors in UCSD; especially those have taught me in class and those who have offered me valuable suggestions and instructions in my preliminary and qualifying examinations.

I must also thank my colleagues, friends and people who I have collaborated with. It is of great help to be able to have meaningful discussions with people working in the same area. And friends have always given me something more than mental support.

Finally, I should thank my family. The continuous family bonding and care hold me up in face of challenging times. It is through this mutual share and care that I have learned to grow and to contribute.

Part of Chapter 2 was published in *Journal of Vacuum Science & Technology B Microelectronics &Nanometer Structures Processing Measurement & Phenomena* 2004, H. Zhang, E. J. Miller, E. T. Yu, C. Poblenz, and J. S. Speck. The dissertation author was the first author of this paper.

Part of Chapter 2 was published in *Applied Physics Letters* 2004, H. Zhang, E. J. Miller, E. T. Yu, C. Poblenz, and J. S. Speck. The dissertation author was the first author of this paper.

Most of Chapter 3 was published in *Journal of Applied Physics* 2006, H. Zhang, E. J. Miller, and E. T. Yu. The dissertation author was the first author of this paper.

Most of Chapter 4 was published in *Journal of Applied Physics* 2006, H. Zhang, and E. T. Yu. The dissertation author was the first author of this paper.

VITA

2001	B. S., Applied Physics, Tsinghua University, Beijing, P. R. China
2004	M. S., Electrical Engineering, University of California, San Diego, CA
2005	C. Phil., Electrical Engineering, University of California, San Diego, CA
2006	Ph. D., Electrical Engineering, University of California, San Diego, CA

PUBLICATIONS

1. **H. Zhang**, E. J. Miller, E. T. Yu, C. Poblenz, and J. S. Speck, "Analysis of interface electronic structure in $In_xGa_{1-x}N/GaN$ heterostructures", *Journal of Vacuum Science & Technology B Microelectronics & Nanometer Structures Processing Measurement & Phenomena*, **22**, no.4, July 2004, pp.2169-74

2. **H. Zhang**, E. J. Miller, E. T. Yu, C. Poblenz, and J. S. Speck, "Measurement of polarization charge and conduction-band offset at $In_xGa_{1-x}N/GaN$ heterojunction interfaces", *Applied Physics Letters,* vol. **84**, no.23, 7 June 2004, pp.4644-6

3. **H. Zhang**, E. J. Miller and E. T. Yu, "Analysis of leakage current mechanisms in Schottky contacts to GaN and $Al_{0.25}Ga_{0.75}N/GaN$ grown by molecular-beam epitaxy", *Journal of Applied Physics,* **99**, 023703 (2006)

4. **H. Zhang**, and E. T. Yu, “Demonstration and analysis of reduced reverse-bias leakage current via design of nitride semiconductor heterostructures grown by molecular-beam epitaxy”, *Journal of Applied Physics,* **99**, 014501 (2006)

5. B. Simpkins, **H. Zhang** and E. T. Yu, “Defects in nitride semiconductors: from nanoscale imaging to macroscopic device behavior”, *Materials Science in Semiconductor Processing,* in press (electronic version published online 7 February, 2006)

ABSTRACT OF THE DISSERTATION

Nitride Semiconductor Surface and Interface

Characterization and Device Design

by

Hongtao Zhang

Doctor of Philosophy in Electrical Engineering (Applied Physics)

University of California, San Diego, 2006

Professor Edward T. Yu, Chair

With the rapid improvement of nitride semiconductor epitaxial growth technology, the precise and accurate electrical characterization of MBE grown nitride semiconductors and its alloys is essential for nitride device analysis and design.

In the first part of the dissertation, a variant of the conventional capacitance-voltage profiling technique is developed and applied to deduce interface charge densities and band-offset values at $In_xGa_{1-x}N$/GaN heterojunction interfaces grown by molecular beam epitaxy (MBE). Conduction-band offsets of 0.09 ± 0.07 eV and 0.22 ± 0.05 eV, and polarization charge densities of $(1.80 \pm 0.32) \times 10^{12}$ e/cm^2 and $(4.38 \pm 0.36) \times 10^{12}$ e/cm^2 are obtained for x=0.054 and x=0.09, respectively. The measured polarization charge densities are lower than those predicted theoretically,

but are in good agreement with values inferred from optical data reported for $In_xGa_{1-x}N/GaN$ quantum-well structures.

The second part of the dissertation focuses on reverse-bias leakage current analysis of Schottky diode fabricated on MBE-grown GaN and $Al_{0.25}Ga_{0.75}N/GaN$ heterojunction field effect transistor (HFET) devices. By combining temperature-dependent current-voltage measurements with conductive atomic force microscopy and analytical modeling, we conclude that below 150K, the leakage current is dominated by tunneling transport; while at higher temperatures, it is dominated by dislocation-assisted Frenkel Poole emission mechanism.

In the third part of the dissertation, we develop heterostructure design strategy, implemented using a GaN cap layer atop a conventional MBE $Al_xGa_{1-x}N/GaN$ HFET structure, based on engineering the electric field at the metal-semiconductor interface of a Schottky contact. The Frenkel Poole emission of electrons into conductive screw dislocations is thus suppressed and the measured reverse-bias leakage currents are reduced by one to three orders of magnitude. Scanned probe measurements of local, nanoscale current distributions confirm directly that current flow via conductive dislocations is suppressed in structures incorporating the GaN cap layer.

In the appendix, possible applications of negative index material (NIM) in resonator structures are analyzed and followed by a discussion of a new NIM structural design and preliminary fabrication studies.

1. Introduction

1.1 Motivation and Background

Information Technology (IT), enabled largely by revolutions in semiconductor fabrication technology and advancements in microwave theory and practice, has become pervasive in modern society. Hardly anyone can escape the impact brought about by its concepts, products and services at any moment of our lives. It has greatly changed the way how we think in the engineering world. The evolution of this science and technology is accelerating at a dazzling pace and is feeding back more and more stringent demand on the development of this technology. Fundamentally, the future of this technology is restricted by material limitations, so more and more materials are tested and engineered for their unique properties to fit our needs.

GaN and its alloys have attracted considerable attention recently because of their potential applications not only in optoelectronic devices such as blue/ultraviolet light emitting diodes, ultraviolet detectors,[1,2] and blue lasers—a key component in high-density optical storage—but also in electronic devices such as heterojunction field effect transistor (HFET), heterojunction bipolar transistor (HBT),[3-5] and power switches and rectifiers, many of which are expected to serve as building blocks in high speed microwave communication circuits.

Optical devices based on ternary alloys of GaN and InN cover the entire visible spectrum from infrared to ultraviolet due to the wide range of direct band gaps available, which is from 0.7-0.8 eV for InN[6] to 3.42 eV for GaN[7]. The success of many of these devices such as multiple-quantum-well (MQW) lasers depends on the detailed and precise knowledge of material properties and properties of GaN/InGaN

heterojunction interface such as conduction band offsets and polarization charges. The variations of conduction band offsets and polarization charge densities with Indium content have a tremendous influence on spectrum shift and emission efficiency. The heterojunction polarization charges, which induce electric fields inside quantum well structures or at a heterojunction interface, are exceptionally large in the nitride semiconductors and are coming from two sources, the major part of which for GaN/InGaN heterostructure is the piezoelectric polarization resulting from the large lattice mismatch between GaN and InGaN. The unequal spontaneous polarizations of GaN and InGaN, resulting from the inherent asymmetry of nitride unit cells, contribute the other portion of the charges. The conduction band offset at the interface can be considered to originate from the differences of the electron affinity in the nitride families, and plays a key role in carrier confinement in optoelectronic and electronic devices. Understanding and control of the polarization charge densities leads to a new degree of freedom in device design and engineering. However, given the difficulties of growing high quality nitride materials, especially high quality InGaN materials, and also due to the difficulties of measurement per se, InGaN/GaN heterojunction interface properties are often extremely hard to measure, if not impossible. In the second chapter, I demonstrate how this problem was addressed and describe successful measurements of polarization charges and band offsets in GaN/InGaN heterojuctions with high precision by careful design of the heterojunction structure, pretreatment of the material surface, and proper modeling and analysis of DUT (Device Under Test).

Because GaN has a large energy band gap of 3.4 eV, a high critical breakdown field of 3×10^{6} V/cm[8] a high thermal conductivity of 1.3W/cm and high peak and saturated electron velocities of 3×10^{7} cm/s and 2×10^{7} cm/s,[9] the promise of GaN applications in high frequency, high power amplifiers and circuits is very bright, especially for the AlGaN/GaN heterojunction field effect transistor (HFET), which has a high-density two dimensional electron gas (2DEG) with high mobility formed at the AlGaN/GaN heterojunction interface. The GaN-base HFET devices have achieved output power densities over 10W/mm[10,11] in the C- and X-band. However, the prospect of its application is dependent on the availability of high quality materials: the performance and reliability of current AlGaN/GaN HFET devices remain limited by problems associated to a large degree with material growth and quality.

The most commonly used methods to grow nitride semiconductors are metal-organic chemical vapor deposition (MOCVD) and molecular beam epitaxy (MBE). For both growth methods, the lack of native substrates has a tremendously negative effect on the material quality, although in MBE growth, this problem is more prominent. In MBE-grown nitrides, typical dislocation density is around $10^{8}-10^{9}cm^{-2}$ [12], which can severely affect device uniformity, reproducibility and reliability. As device dimensions are scaled down, device uniformity gets poorer since the uniformity and reproducibility are strongly correlated to the distribution of defects and dislocations in the device.

However, for HFET devices in high speed systems, 2DEG density and mobility are the most important figures of merit. The 2DEG density is largely determined by the polarization charge density, which is not directly influenced by

growth method. However, 2DEG mobility is largely determined by growth method and growth condition.

MBE is considered a desirable growth method for GaN based HFET devices because MBE achieves higher 2DEG mobility in AlGaN/GaN heterostructures on GaN template at low temperature (as high as 75,000 cm^2/Vs[13] at 4.2K) as well as at room temperature. In addition, MBE also provides low background impurity concentrations and precise control of layer thickness at the atomic scale. MBE-grown films produced under Ga-rich conditions (referring to having Ga-droplet formation on the surface during growth) generate the highest 2DEG mobility[14] and have the smoothest surface with only monolayer steps, and dislocations appear as hillocks.[15] However, the growth method and stoichiometry also strongly influence the electrical activity and core structures of dislocations.[15] Reverse leakage current of Schottky diode on Ga-rich samples is 2 to 3 orders of magnitude higher than it is on Ga-lean samples at a fixed bias due to conductivity differences of dislocations. Reverse bias leakage current reduces HFET current-voltage handling ability, increases its power consumption and degrades its device noise performance. In the third chapter, I describe a detailed analysis of the mechanism of leakage current in GaN and AlGaN/GaN systems and its correlation with dislocations. In the fourth chapter, I will demonstrate how to reduce leakage current based on information and understanding derived from the studies presented in the third chapter.

1.2 Thesis Organization

The Schottky barrier is one of the fundamental building blocks for electronic devices. It is widely used for fast switching circuits, due to the fast response from majority carriers and low diffusion capacitance. It is used as the controlling gate to modulate the field effect transistor (FET) channel current. It is also used as a powerful tool in studying material electrical properties. Much of this thesis has been conducted using Schottky diodes fabricated on the nitride semiconductors. I will demonstrate how we have extracted GaN/$In_yGa_{1-y}N$ heterojunction band offsets and polarization charge densities from GaN/$In_yGa_{1-y}N$ Schottky diodes in the second chapter while in the third and fourth chapters I will show how we have analyzed and reduced leakage currents in GaN and $Al_xGa_{1-x}N$/GaN Schottky diode.

The appendix discusses recent work on a somewhat different topic in solid-state electronics—the negative index material (NIM). The concept of NIM was first discussed by Veselago in 1967-1968[16]. Through the work of Pendry[17] and Smith[18] it has gained broad recognition as a potential new material for near field optical components as well as in microwave devices such as transmission lines[19,20] or antennas.[21,22] The appendix discusses analytical studies of the application of NIM in highly compact microwave resonators, and novel schemes for design and fabrication of NIM structural building blocks.

2. Capacitance-Voltage (C-V) Measurement of Polarization Charge Density and Conduction Band-offset at GaN/$In_yGa_{1-y}N$ Heterojunction Interface

2.1 Introduction

2.1.1 Motivation and Outline

GaN/$In_yGa_{1-y}N$ heterostructures are of outstanding current interest for both electronic[23,24] and optoelectronic[25] device applications. The design, analysis, and optimization of such devices require a detailed, quantitatively accurate understanding of electronic structure at the GaN/$In_yGa_{1-y}N$ heterojunction interface, and in particular require accurate knowledge of parameters such as the interfacial polarization charge densities and the conduction- and valence-band offsets. However, the measurement of polarization fields and charge densities is often complicated by the influence of free-carrier screening effects, and the experimental determination of band offsets is fraught with a variety of experimental and modeling perils that can lead to inaccurate or highly uncertain results.

In this study, we have used capacitance-voltage (C-V) profiling through GaN/$In_yGa_{1-y}N$ heterojunction interfaces to measure the polarization charge densities and conduction band offsets for GaN/$In_yGa_{1-y}N$ heterojunctions with y=0.054 and y=0.09. Our results yield a conduction- to valence-band offset ratio $\Delta E_C : \Delta E_V = 58{:}42$ in this range of compositions, and polarization charge densities of $(1.80 \pm 0.32) \times 10^{12}$ e/cm^2 and $(4.38 \pm 0.36) \times 10^{12}$ e/cm^2, respectively—somewhat lower than theoretical predicted values but consistent with results inferred from several optical experiments reported with literature. We have also developed and applied a variant of the conventional analysis technique used to derive interfacial charge density and band-

offset values from capacitance-voltage profiling data that substantially reduces susceptibility to noise and, hence, allows more straightforward and reliable extraction of these parameters. The measured results, especially the measured polarization charge densities for GaN/$In_yGa_{1-y}N$ heterojunction interface, provide important information to design engineers. The functions and performances of GaN/$In_yGa_{1-y}N$ based HFET and quantum well devices depend critically on the accurate knowledge of the heterojunction interface properties, which relies on the precise and detailed characterization of the polarization charge densities and band-offsets.

2.1.2 Polarization Charges and Band-offsets for Nitride Semiconductors

One of the very unique properties of nitride semiconductors is the presence, due to the wurtzite crystal structure, of large spontaneous polarization, which originates from the lack of inversion symmetry in the nitride semiconductor hexagonal unit cell in which the positive and the negative electric charge centers are separate. This spontaneous polarization is always along the $[000\bar{1}]$ direction,[7] which is defined by a vector pointing from a N atom to a nearest-neighbor Ga atom or other III-element atom along the *c*-axis. But the magnitude of the spontaneous polarization is not the same in different nitride semiconductors. So at the nitride semiconductor heterojunction interface, the spontaneous polarization discontinuity leads to a net polarization charge. Depending on the relative magnitude of each individual spontaneous polarization, this net charge density can be either positive or negative. A related and also very important property of wurtzite nitrides is the exceptionally large piezoelectric effect. For epitaxially growed nitride thin film (thinner than critical

length), due to its lattice mismatch with the substrate, the lattice deformation of the thin film in the (0001) plane causes the lattice deformation along the *c*-axis, which changes the separation of the electric charge centers and generates what we call the piezoelectric polarization $P_{pz,z}$ along the *c*-axis whose magnitude depends on the relative change of the lattice constant a in the (0001) plane. Theoretically, the piezoelectric polarization is related to the strain field by:[26]

$$P_{pz,z} = 2d_{31}(c_{11} + c_{12} - 2\frac{c_{13}^2}{c_{33}})\varepsilon_1 , \quad (2.1)$$

where d_{ij} is the piezoelectric moduli, c_{ij} is the elastic constant of the crystal (i, j=1,2,3) and strain ε_1 is given by:

$$\varepsilon_1 = \frac{a_{GaN} - a}{a} , \quad (2.2)$$

where we assume a GaN substrate for the thin film.

Because $d_{31}<0$ and $c_{11} + c_{12} - 2\frac{c_{13}^2}{c_{33}} > 0$ for nitrides, the piezoelectric polarization in the thin film is pointing in the $[000\bar{1}]$ direction ($P_{pz,z}<0$) under biaxial tensile strain($\varepsilon_1>0$) while pointing in the [0001] direction ($P_{pz,z}>0$) under biaxial compressive strain($\varepsilon_1>0$), At the nitride heterojunction interface between epitaxial layers, the total polarization charges, which are in the order of $10^{12} - 10^{13}$ e/cm^2, are coming from the unbalanced spontaneous polarization of the film and the substrate and the piezoelectric polarization in the film induced by the lattice-mismatch. The polarization charge density ρ_i (which we refer to as the interface charge density Q_i in

the C-V measurement) can be related to the total polarization field $\vec{P}$ according to Maxwell equation:

$$\nabla\vec{P} = -\rho_i\,, \tag{2.3}$$

where $\nabla\vec{P}$ gives the divergence of the spontaneous polarization discontinuity and the piezoelectric polarization.

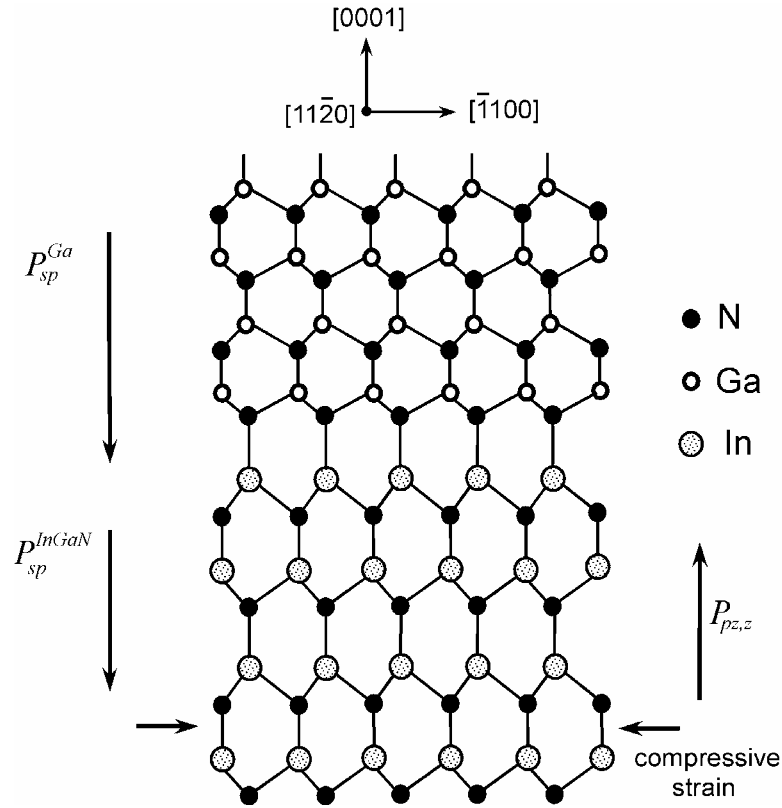

Fig. 2.1 Crystal structure, spontaneous polarization and piezoelectric polarization for GaN/$In_yGa_{1-y}N$ heterojunction. The structure is coherently stained to GaN (0001)

The crystal structure, spontaneous polarization and piezoelectric polarization for GaN/$In_yGa_{1-y}N$ heterojunction is depicted in Fig. 2.1 as an example, assuming a GaN substrate. Because the spontaneous polarization in GaN P_{sp}^{GaN} is relatively larger

than the spontaneous polarization P_{sp}^{InGaN} in $In_yGa_{1-y}N$, unbalanced spontaneous charges at the interface are positive. Because the $GaN/In_yGa_{1-y}N$ epi-layer are grown on the GaN substrate and because the lattice constant of $In_yGa_{1-y}N$ is larger than that of GaN, the $In_yGa_{1-y}N$ epi-layer is under compressive strain, having a polarization vector pointing in the [0001] direction. The piezoelectric polarization charges are therefore also positive at the interface. The combined total polarization charges at $GaN/In_yGa_{1-y}N$ interfaces are positive and theoretically the dominant part of the net charges is from the piezoelectric polarization.

The theoretical predictions[7] of the polarization charge density for $Al_xGa_{1-x}N/GaN$ heterojunction interface matches quite well with the experimental measurement.[27] However, for $GaN/In_yGa_{1-y}N$ heterojunction interface, we found the theoretical prediction[7] can not agree with the experimentally measured results. This has a great implication in $GaN/In_yGa_{1-y}N$ heterojunction devices design and engineering because the polarization charge density is such a vital parameter that it fundamentally influences the characteristics and the performance of the devices.

The polarization charges induce strong electric field at nitride heterojunction and attract a large number of electrons, if the polarization charges are positive, or holes, if otherwise, at the heterojunction to compensate this electric field. These electrons or holes are confined inside the quantum wells formed by the conduction band offset or valence band offset, within a few nanometers away from the heterojunction interface. Because of the large polarization charge densities and the band offset confinement, the electron or hole concentration is very high, forming a

sheet of two-dimensional electron or hole gas (2DEG or 2DHG). The accurate and precise knowledge of the variations of the polarization charge densities and band offsets for different nitride semiconductors is critical for accurate predicament of the magnitude of the electric field inside the quantum wells and the sheet charge density at the heterojunction. This knowledge allows us to understand the fundamental physics and the opto-electronic operations of the nitride semiconductor quantum well devices, and it is also the basis in designing and engineering the electrostatic barriers in nitride semiconductor heterojunction devices. We will later discuss in details in this chapter how our results for the polarization charge densities and conduction band-offsets measurement would influence the design and the engineering of the HFET devices and the quantum well optical devices.

2.2 Experiment Techniques

2.2.1 General Description of Capacitance Voltage Profiling Techniques

The capacitance–voltage (C-V) technique is based on measurement of the capacitance of the space charge region. A DC bias is applied to change the width of the space charge region, and a small AC bias is added to measure the capacitive response from the edge of the space charge region due to the free carriers. By sweeping the DC bias voltage, and therefore changing the location of the edge of the space charge region inside the semiconductor, detailed information of about the free carrier distribution can be obtained. The capacitive response comes from charging and discharging effect of free carriers dQ_s at the edge of the depletion region due to the small AC signal dV:

$$C = -\frac{dQ_s}{dV} = -\frac{qnSdw}{dV}, \tag{2.4}$$

where n is the free carrier density, q is electron charge unit and dw is the change of depletion width due to dV. By modeling the space charge region, which is usually formed from the Schottky contact at the metal-semiconductor interface, as a parallel plate capacitor, the depletion width w and the capacitance C are related according to the expression:

$$C = \frac{\varepsilon S}{w}, \tag{2.5}$$

where S is the area under the Schottky contact, and ε is the dielectric constant of the semiconductor.

Combining Eqs. (2.4) and (2.5), the electron charge density at the depletion edge w can thus be derived as[28]:

$$n^* = -\frac{2}{q\varepsilon S^2 d(1/C^2)/dV}, \tag{2.6}$$

with the depletion width w calculated from Eq. (2.5) being the depth for what n^* is obtained. Here, n^* is called 'apparent carrier concentration' to differentiate it from the actual electron density n. n^* is different from n because of the Debye length smearing, which limits the spatial resolution of the calculated profile, but it is a good approximation provided that the carrier potential energy of concentration are not varying rapidly at length scales comparable to or smaller than the Debye length.

To probe the electronic structure of the heterojunction, which consists of different semiconductor material—upper layer 1 and lower layer 2—and whose

depletion region starts from the Schottky contact at the metal-semiconductor layer 1 interface, Eq. (2.5) should be modified as:

$$\begin{aligned} w &= \frac{\varepsilon_1 S}{C} & & w < w_h \\ & & if \quad & \quad , \\ w &= \frac{\varepsilon_2 S}{C} + (1 - \frac{\varepsilon_2}{\varepsilon_1}) w_h & & w > w_h \end{aligned} \tag{2.7}$$

where, ε_1 and ε_2 are the dielectric constants of the semiconductor materials in the upper and lower layers respectively, and w_h is the heterojunction position. Eq. (2.6) should remain unchanged.

Once the apparent carrier concentration profile has been determined, the interface charge density Q_i and the conduction band offset ΔE_C at the heterojunction interface are given by[29]

$$Q_i = q \int_{w_1}^{w_2} (n^*(w) - N_d^+(w)) dw, \tag{2.8}$$

$$\begin{aligned} \Delta E_C &= -q^2 \int_{w_1}^{w_2} \{\frac{1}{\varepsilon(w)} [N_d^+(w) - n^*(w)](w - w_h)\} dw \\ &- kT[\ln(\frac{n_1 / N_{C1}}{n_2 / N_{C2}}) + \frac{1}{\sqrt{8}} (\frac{n_1}{N_{C1}} - \frac{n_2}{N_{C2}})] \end{aligned} , \tag{2.9}$$

where $N_d^+(w)$ is the ionized donor concentration at depth w below the metal-semiconductor interface, N_{C1} and N_{C2} are the conduction-band effective densities of states of the first and second layer of semiconductor material, respectively, and n_1 and n_2 are the free electron concentrations in the corresponding layers. The integration limits w_1 and w_2 are chosen to be far from the heterojunction, where the electric field is negligible. The physical meaning of these two equations is self-evident. Eq. (2.8) is the integration of the carrier and donor charges near the heterojunction. Due to the

charge neutrality condition, integration of these charges yields the fixed charge at the heterointerface, which for nitride heterojunction interfaces we assume to be dominated by the polarization charge. The first part of Eq. (2.9) is the first moment of the carrier and donor charges, and gives the total built-in potential within these two layers. The second part of Eq. (2.9) accounts for the Fermi-level variations in each layer, with the combination of these two terms yielding the conduction band offset ΔE_C. The apparent carrier concentration was used instead of the real carrier concentration, however, the integration or the first momentum integration should remain unmodified.[29]

2.2.2 Improvement on Band-offset Calculation

While the approach introduced in the previous section allows, in principle, straightforward determination of Q_i and ΔE_C from capacitance-voltage spectra, the accurate construction of the apparent carrier concentration profile $n^*(w)$ typically requires considerable care as a numerical differentiation of the capacitance-voltage curve must be performed. This differentiation can magnify any noise present in the capacitance data, potentially leading to inaccuracies or at least increased uncertainty in $n^*(w)$, Q_i, and ΔE_C. An alternate approach that largely circumvents these difficulties can be derived by noting that, from Eq. (2.7), $dw=-(\varepsilon_1 S/C^2)dC$. With this relationship, Eqs. (2.8) and (2.9) can be transformed with Q_i and ΔE_C then given by

$$Q_i = \frac{1}{S}\int_{V_1}^{V_2} CdV - q[n_1(w_h - w_1) + n_2(w_2 - w_h)], \tag{2.10}$$

$$\Delta E_C = -q^2[\frac{1}{2\varepsilon_2} n_2 (w_2 - w_h)^2 - \frac{1}{2\varepsilon_1} n_1 (w_h - w_1)^2]$$

$$+q[V_2 - V_1 - \frac{w_h}{\varepsilon_1 S}\int_{V_1}^{V_2} CdV] - kT[\ln(\frac{n_1/N_{C1}}{n_2/N_{C2}}) + \frac{1}{\sqrt{8}}(\frac{n_1}{N_{C1}} - \frac{n_2}{N_{C2}})], \qquad (2.11)$$

where V_1 and V_2 are the voltages at which the depletion layer width reaches w_1 and w_2, respectively. From Eqs. (2.10) and (2.11) we see that the apparent carrier concentration profile $n^*(w)$ plays only an intermediary role mathematically in the determination of Q_i and ΔE_C, which can be obtained by direct integration of the capacitance-voltage curve. This approach allows numerical challenges associated with the computation of $d(1/C^2)/dV$ to be avoided, and enables a more straightforward and robust calculation of Q_i and ΔE_C. We have used both Eqs. (2.8)-(2.9) and Eqs. (2.10)-(2.11) to calculate polarization charge densities and conduction band offsets, and with proper care using the former approach, both computations yield very consistent results.

2.2.3 Heterostructure Design and Nitride Growth

The general approach is using C-V spectroscopy to probe the properties of semiconductor heterojunction interface is to construct a metal-semiconductor (M-S) Schottky contact on top of the upper layer of the structure and to apply bias on this Schottky-barrier-induced space charge region. This space charge region has to be thinner than the thickness of the upper material at zero bias to allow its information to be probed without forward biasing the junction. On the other hand, it has to be able to extend deeply across the heterojunction with reasonably small reverse biases. Both requirements are aiming at the same condition: small current flow in the measurement. We will discuss the necessity of this condition in section 2.3.2. For obvious reasons,

the reverse bias can not exceed the breakdown voltage limit imposed by the inherent properties of the material.

In this study, the heterojunction layer thicknesses as well as the doping concentrations in the epitaxial layers were carefully designed to meet the requirements mentioned above. In addition, the structures were designed such that the epi-layers on both sides of the heterojunction were not fully depleted at zero bias to allow the dopant concentrations on both sides to be extracted directly during the C-V measurement.

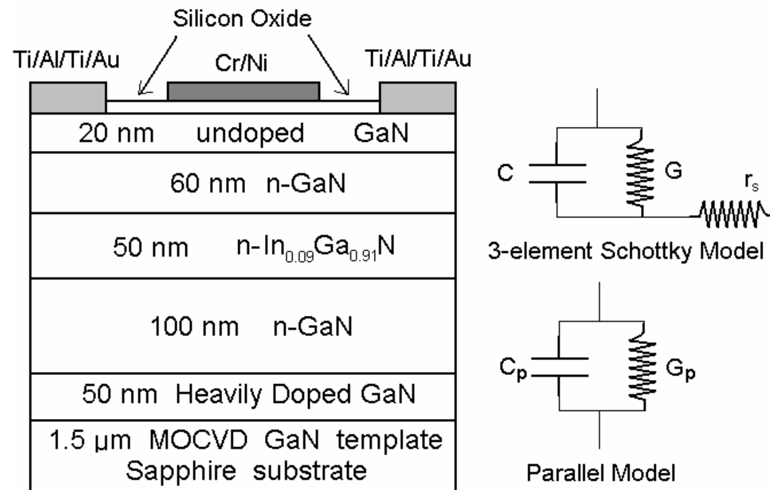

Fig. 2.2 Schematic diagram of the GaN/$In_yGa_{1-y}N$/GaN epitaxial layer structure and the corresponding equivalent circuit models used in this study. The silicon oxide layer as present only for the y=0.09 sample to reduce the leakage current. There is no oxide on y=0.054 sample because the leakage current is small enough for the measurement. The two element parallel model was assumed during the measurement but was later corrected using the three element model to remove the series resistance effect r_s.

The epitaxial layer structure of the $In_yGa_{1-y}N$/GaN samples used in this study is shown schematically in Fig. 2.2. Two samples were characterized, one with a 50nm $In_{0.09}Ga_{0.91}N$ layer and the other with a 30nm $In_{0.054}Ga_{0.946}N$ layer. As mentioned

above, the epitaxial layer structures employed layer thicknesses and dopant concentrations designed to ensure that undepleted regions with negligibly small electric field were present above and below each heterojunction interface. This requirement is necessary because it is the condition for Eq. (2.8) and Eq. (2.9) or Eq. (2.10) and Eq. (2.11) to be valid and therefore it is also the condition for the accurate calculation based on the C-V measurement. To achieve this, n-type doping of $\sim 10^{18}$ cm^{-3} in the $In_yGa_{1-y}N$ layer and the surrounding GaN layers shown in Fig. 2.2 was targeted. Both samples were grown by rf-plasma assisted molecular beam epitaxy (MBE) on a ~1.5 μm thick metal organic chemical vapor deposition (MOCVD) GaN template deposited on a sapphire substrate.[30] The MBE epitaxial layers were grown at 650ºC and the crystal polarity was determined to be Ga-face, based on cross-sectional TEM and AFM measurements. The polarity, which is influenced by growth method, growth condition and substrate,[31] determines the orientation of the spontaneous and piezoelectric polarization inside the material and therefore has a drastic effect on the heterojunction interface properties, two-dimensional electron gas (2DEG) densities[32], and various other aspects of device performance.[33] Since Indium content affects both spontaneous and piezoelectric polarization and strain relaxation reduces the magnitude of piezoelectric polarization, X-ray reciprocal space mapping measurements were used to determine the composition of the $In_yGa_{1-y}N$ layers and to confirm that the heterostructures were fully strained.

2.3 Schottky Diode Fabrication, C-V Measurement and Schottky Diode Modeling

2.3.1 Schottky Diode Fabrication on n-type GaN

Optical lithography was used to define the ohmic contact region, within which the PECVD-grown oxide was removed using buffered oxide etch (BOE) before ohmic metal deposition. Ti/Al/Ti/Au (330Å/770Å/300Å/1000Å) ohmic contact metallization was deposited using electron beam evaporation and then annealed in forming gas (15% H_2 and 85% N_2) at 650 °C for 1 minute. Cr/Ni (200Å/1200Å) metallization was then used for the Schottky contact with Cr serving to enhance the adhesion of Ni to the oxide layer. For the $In_{0.054}Ga_{0.946}N$ sample, the leakage current density is about 150 A/cm^2, small enough to allow accurate C-V characterization, and therefore no oxide was deposited. 1500Å Ni was directly evaporated on the sample surface to form the Schottky contact with Ti/Al/Ti/Au metallization used to form the ohmic contact as described above.

2.3.2 Leakage Current Reduction Prior to C-V Measurement

A key prerequisite of the capacitance-voltage profiling method is the steady-state condition, and the incremental charge assumption underlying this technique is rigorously justified only if there is zero or negligible current flow in the device under DC bias.[34] This requirement can be problematic for nitride semiconductor material grown by MBE, for which leakage currents in Schottky contacts can be very high.[35,36] For the GaN/$In_{0.09}Ga_{0.91}N$/GaN sample, a thin layer of silicon oxide (30-130Å) was deposited on the $In_{0.09}Ga_{0.91}N$ sample, as indicated in Fig. 2.2, by plasma-enhanced chemical vapor deposition (PECVD) to reduce the current density from several hundred amperes per square centimeter to approximately 10 amperes per square centimeter. A preparatory surface treatment[37] was required to reduce the oxide-GaN

interface state density. The specific procedure employed was as follows: the sample was first cleaned in supersonic agitated organic solvents (TCE, acetone, isopropanol alcohol and methanol) and then soaked in an NH_4OH solution at 50 °C for 15 minutes. After each step, the sample was thoroughly rinsed in deionized water. An N_2 plasma treatment was performed at 300 °C with an excitation power of 30 watts for 5 minutes. The oxide was then immediately deposited in the same chamber at a lower temperature to avoid contamination. The deposited oxide reduced the reverse-bias leakage current by 1-2 orders of magnitude, which was sufficient for these measurements. The combination of a very thin oxide layer with the plasma and chemical surface treatment prior to oxide deposition allowed us to avoid hysteresis effects associated with interface states in our C-V measurement. Numerical simulations were used to confirm that the effect of the oxide layer on the potential drop across the semiconductor depletion layer was not significant.

2.3.3 C-V Measurement and Comprehensive Schottky Diode Modeling

Capacitance-voltage measurements were performed using an HP 4285A Precision LCR Meter at frequencies ranging from 100 kHz to 1 MHz, at room temperature under ambient lighting conditions using the parallel circuit mode of the HP4285A. The presence of the insulating oxide layer in one diode structure as described above leads to a high series resistance, which must be properly accounted for in the analysis of the capacitance-voltage spectra. As shown in Fig. 2.2, a three-element circuit incorporating the depletion capacitance C, conductance G, and a parametric series resistance r_s is used to model the behavior of the Schottky diode. r_s is

assumed to include the resistance of the undepleted bulk material, contacts, and insulating oxide layer. Measurements were obtained in the parallel mode of operation of the HP4285A, and therefore yielded capacitance C_p and conductance G_p. A simple circuit analysis yields the following relationships[28] among C_p, G_p, C, G, r_s and the measurement angular frequency ω:

$$C_p = \frac{C}{(1+r_s G)^2 + (\omega r_s C)^2}, \tag{2.12}$$

$$G_p = \frac{G(1+r_s G) + r_s(\omega C)^2}{(1+r_s G)^2 + (\omega r_s C)^2}. \tag{2.13}$$

As is evident from Eqs. (2.12) and (2.13), the measured capacitance and conductance, C_p and G_p, respectively, can exhibit substantial frequency dependence and can deviate significantly from the actual capacitance and conductance of interest when r_s is large compared to $1/G$ or $1/\omega C$. Analysis of and correction for these effects of series resistance were therefore essential in our investigation.

The series resistance r_s was assumed to be constant and was determined from the measured conductance G_p under forward bias. For sufficiently large forward bias, G becomes large compared to ωC and $1/r_s$, and Eq. (2.13) can be written approximately as

$$\frac{1}{G_p} \approx \frac{1}{G} + r_s \approx r_s . \tag{2.14}$$

Once r_s was determined in this manner, C and G were obtained from the measured values of G_p and C_p using Eqs. (2.12) and (2.13). Fig. 2.3 shows measured capacitances C_p for each sample structure at selected frequencies ranging from 100

kHz to 1 MHz. The frequency-dependent nature of C_p is especially obvious under small forward bias when r_s is much larger than $1/G$. After the correction for series

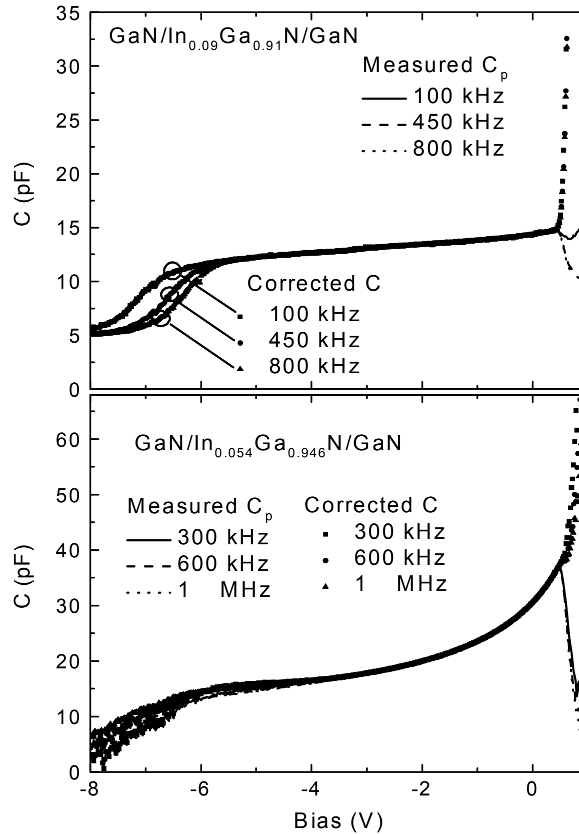

Fig. 2.3 Measured C_p and the derived capacitance C after consideration of the effect of series resistance r_s for GaN/$In_{0.09}Ga_{0.91}N$/GaN (top diagram) and for GaN/$In_{0.054}Ga_{0.946}N$/GaN (bottom diagram).

resistance effects, this frequency-dependence disappears and the corrected C-V curves, also shown in Fig. 2.3, can be more directly associated with the properties of the semiconductor heterostructure under investigation. There remains a dependence of the C-V curves on frequency at large negative bias voltage, possibly due to interface

statesat the GaN/$In_yGa_{1-y}N$ heterojunction. At higher frequencies, trapped charges at the interface may not be modulated and therefore the capacitance is lower than that obtained at lower frequencies. However, the frequency dependence of the capacitance at these voltages has only a very small effect on the determination of the interface polarization charge density and conduction-band offset, described in Section III. The series resistance correction has a substantial influence in determining the carrier concentration near the surface of the diodes, particularly in the GaN/$In_{0.09}Ga_{0.91}N$/GaN sample, which has a much larger series resistance r_s because of the oxide layer, but has a relatively minor effect in determining the carrier concentrations farther below the surface. Values for r_s ranged from 50-80 Ω for the GaN/$In_{0.054}Ga_{0.946}N$/GaN sample to 1200-1300 Ω for the GaN/$In_{0.09}Ga_{0.91}N$/GaN sample.

2.4 Experimental Results and Discussion

2.4.1 C-V Measurement Results

Fig. 2.4 shows apparent carrier concentration profiles computed using Eqs. (2.6) and (2.7) for both heterojunction structures employed in these studies. Electron accumulation at the upper GaN/$In_yGa_{1-y}N$ interfaces is clearly evident, and the carrier concentration profiles determined in this manner are seen to be very consistent for frequencies ranging from 100 kHz to 1 MHz, although the background dopant concentrations obtained are generally somewhat lower than targeted. The scatter in the apparent carrier concentration profile is due primarily to noise in the C-V data, which is magnified in the profile of n^* due to the need to numerically differentiate the C-V profile. However, this scatter has little effect on the subsequent determination of Q_i

and ΔE_C. The origin of the dip that appears within the concentration peak in Fig. 2.4 (a) is not certain, but maybe related to the occupation of multiple quantum confined

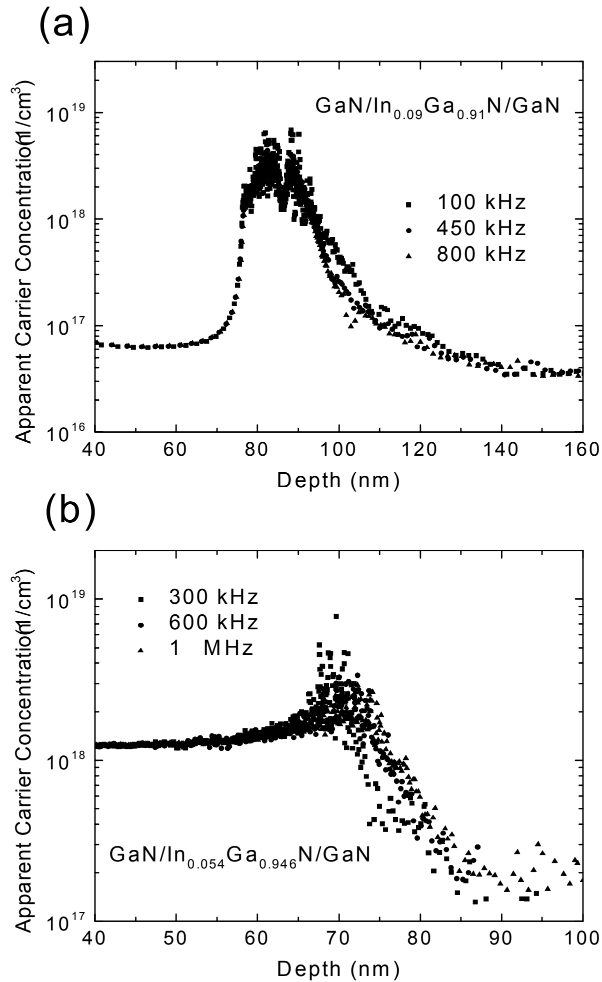

Fig. 2.4 Apparent carrier concentration profiles (a) for the $In_{0.09}Ga_{0.91}N/GaN$ heterostructure, derived from C-V data obtained at frequencies of 100 kHz (■), 450 kHz (♦), and 800 kHz (▲) (top diagram) and (b) for the $In_{0.054}Ga_{0.946}N/GaN$ heterostructure, derived from C-V data obtained at frequencies of 300 kHz (■), 600 kHz (♦), and 1 MHz (▲) (bottom diagram).

states at the $GaN/In_{0.09}Ga_{0.91}N$ interface. Solutions of Poisson and Schrödinger

equations for this structure suggest that more than one quantum-confined state may be occupied, leading to an electron concentration profile such as that shown in Fig. 2.4 (a).

2.4.2 Determination of Polarization Charge Density

The polarization charge densities at the $In_{0.054}Ga_{0.946}N$/GaN and $In_{0.09}Ga_{0.91}N$/GaN interfaces deduced from our measurements using Eq. (2.10) are $(1.80 \pm 0.32)\times 10^{12}$ *e*/cm^2 and $(4.38 \pm 0.36)\times 10^{12}$ *e*/cm^2, respectively. In comparison, theoretical calculations yield substantially higher values, ranging from 4.43×10^{12} to 5.25×10^{12} *e*/cm^2 for x=0.054 and from 6.84×10^{12} to 8.74×10^{12} *e*/cm^2 for x=0.09, depending on the different elastic, piezoelectric, and lattice constants assumed.[7] Although few direct measurements of the $In_xGa_{1-x}N$/GaN interface polarization charge densities are readily available, polarization charge densities can be inferred from values of the electric field magnitude within $In_xGa_{1-x}N$/GaN quantum-well structures deduced from photoluminescence(PL),[38-41] electroabsorption,[42]and electrotransmission (ET)[43] experiments. Because of the polarization charges present at each heterojunction interface, a large internal electric field is induced within the $In_{\backslash y}Ga_{1-y}N$/GaN quantum well. Due to carrier screening effects, however, determination of the polarization charge density corresponding to a reported value for the electric field requires a self-consistent solution of the Poisson and Schrödinger equations for the full quantum well structure. Thus, by assuming the quantum-well structure to be known a priori and taking the polarization charge density at the heterojunction interface as a variable parameter, we have used a 1D Poisson/Schrödinger solver [44] to compute the

corresponding electric field, as shown in Fig. 2.5 for the multiple-quantum-well structure of Ref. 38. Failure to account for carrier screening effects can result in an underestimate of the polarization charge corresponding to a measured quantum-well electric field of as much as 20%. By adjusting the polarization charge density until

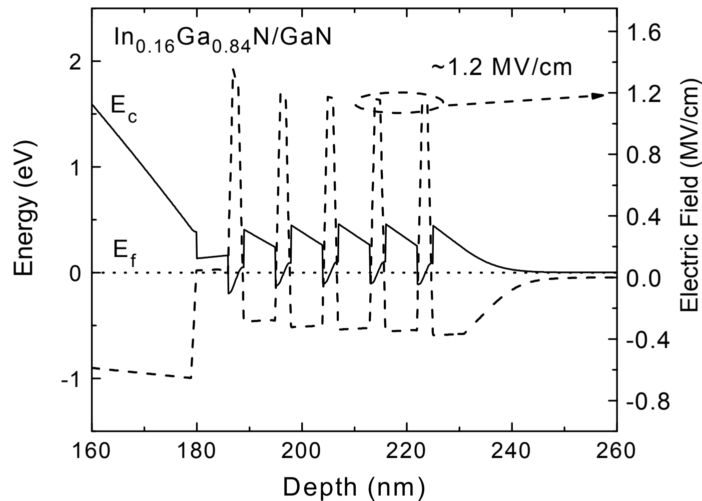

Fig. 2.5 Simulated band structure and electric field for Ref. 39. The indium content is 16% and the assumed polarization charge density is 9.0×10^{12} e/cm^2. The electric field thus deduced is about 1.2 MV/cm.

good agreement is achieved between the simulated and optically measured values of the electric field, the polarization charge density can be inferred, as shown in Fig. 2.6. From Fig. 2.6, we see that the majority of measurements yield polarization charge densities somewhat lower than those predicted theoretically, but in good agreement with our measured values. The measured values and the predicted variations of polarization charge densities against the indium content, much smaller than the theoretical expectations, would have to be taken seriously into considerations in the

analysis, design and engineering of the $GaN/In_yGa_{1-y}N$ heterojunction devices or quantum well devices. Several examples can be demonstrated here: first, polarization charge density as an important parameter has been used to engineer $Al_xGa_{1-x}N/GaN$ or $GaN/In_yGa_{1-y}N$ electrostatic barriers.[45] Recently, a new AlGaN/GaN/InGaN/GaN

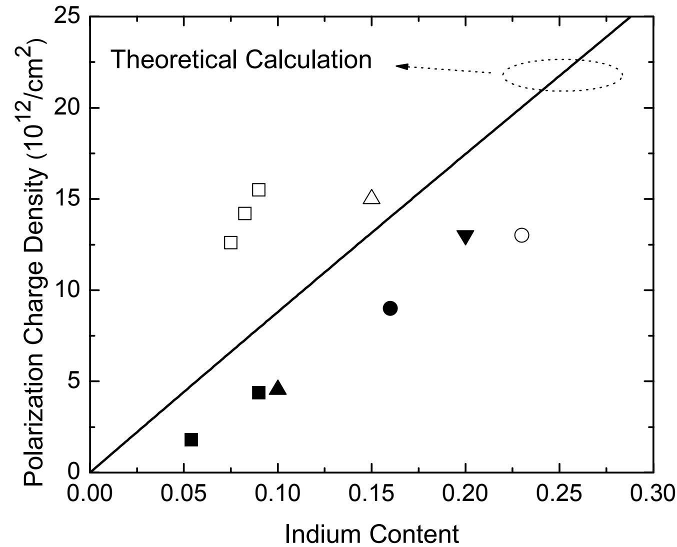

Fig. 2.6 $In_yGa_{1-y}N/GaN$ polarization charge densities from this work (■), and inferred from Ref. 38 (▲), Ref. 39 (●), Ref. 40 (▼), Ref. 41 (Δ), Ref. 42 (□) and Ref. 43 (○). Calculated polarization charge densities (Ref. 7) are also shown in a straight line.

double heterojunction-high electron mobility transistor (DH-HEMT) has been designed and evaluated.[46] This structure employs a GaN/InGaN heterojunction to form a notch in the conduction band. And this modification of the quantum well structure can further confine the electrons inside the GaN channel layer, preventing 2DEG from 'spilling over' into the AlGaN barrier layer and GaN buffer layer, which in turn improves the electron mobility and helps reduce the leakage current in the buffer

layer. The improved isolation of 2DEG and the reduced buffer layer leakage current result in an enhancement on the maximum oscillation frequency f_{max}. However, the accurate knowledge of the polarization charge density at GaN/InGaN heterojunction is critical in this type of device design: if the polarization charge density is too low, the induced polarization field would not be strong enough to bend the band such that there is little 2DEG density waveform tailing into the buffer layer and we would not be able to achieve the improved mobility and the reduced leakage current; if the polarization density is too high, the induced polarization field would bend the conduction band of InGaN below the Fermi-level, forming a minor channel alongside the GaN major channel, creating unexpected and undesired device behaviors. Since the only way to control the GaN/InGaN polarization charge density is to control the indium content in the InGaN layer, what we have found out and summarized in Fig. 2.6 would provide an important guideline in designing and engineering the barrier height of the GaN/InGaN heterojunction devices. Another application of the results from Fig. 2.6 can be found in the GaN/InGaN quantum well light emitting diodes (LEDs).[47] Quantum well LEDs localize electron and hole pairs and therefore improve the quantum efficiency of the emitting diodes. By using InGaN with different indium contents, therefore changing the bandgap of InGaN, a wide range of spectrum can be covered, including green, blue, and ultraviolet. However, this spectrum is also influenced by the polarization charges at GaN/InGaN heterojunction, which induce a strong electrical field inside the quantum wells, reshaping the conduction and valence band structures. This band-bending due to the polarization field would red-shift the spectrum and lower the quantum efficiency by spatially separating the electron-hole

pairs. Therefore, Fig. 2.6 provides the indispensable information to accurately estimate the indium content needed in the GaN/InGaN quantum wells for the desired spectrum. Incorrect knowledge on the GaN/InGaN interface polarization charge density would lead to spectrum deviations from the targeted values. The information obtained from Fig. 2.6 can also be used to estimate the quantum efficiency and the output power of LEDs.

2.4.3 Determination of Conduction Band Offset

By analyzing data acquired at measurement frequencies varying from 100 kHz to 1 MHz, and obtained from several different diodes, we have determined the conduction band offsets to be ΔE_C=0.09 $\pm$ 0.07 eV and ΔE_C=0.22 $\pm$ 0.05 eV for the GaN/$In_yGa_{1-y}N$ heterojunction with y=0.054 and y=0.09, respectively. The uncertainty in ΔE_C for y=0.054 is relatively large partly due to the small value of the conduction band offset itself and partly due to the difficulty in achieving relatively uniform Indium distribution at this composition. Using energy band gaps of 3.42 eV for GaN, 3.225 eV for $In_{0.054}Ga_{0.946}N$ and 3.06 eV for $In_{0.09}Ga_{0.91}N$ [48,49] coherently strained to GaN, and based on the relative uncertainties in our measured conduction-band offsets, we compute a weighted average of the band offset ratio ΔE_C : ΔE_V and obtain ΔE_C : ΔE_V =58:42. In comparison, an analysis of deep yellow photoluminescence[50] in GaN and $In_yGa_{1-y}N$ alloys yielded a conduction-to-valence band offset ratio of 62:38 for y $\leq$ 0.14, corresponding to ΔE_C=0.11 eV and ΔE_C=0.18 eV for the $In_{0.054}Ga_{0.946}N$/GaN and $In_{0.09}Ga_{0.91}N$/GaN interfaces, respectively. This approach assumes the existence of a shallow donor level that follows the conduction band edge and a pinned deep

acceptor level that maintains a constant absolute energy in the $In_yGa_{1-y}N$ and GaN systems; determination of the corresponding luminescence energy as a function of composition in $In_yGa_{1-y}N$ alloys therefore allows the absolute conduction-band edge energy, and consequently conduction-band offsets, to be deduced. X-ray

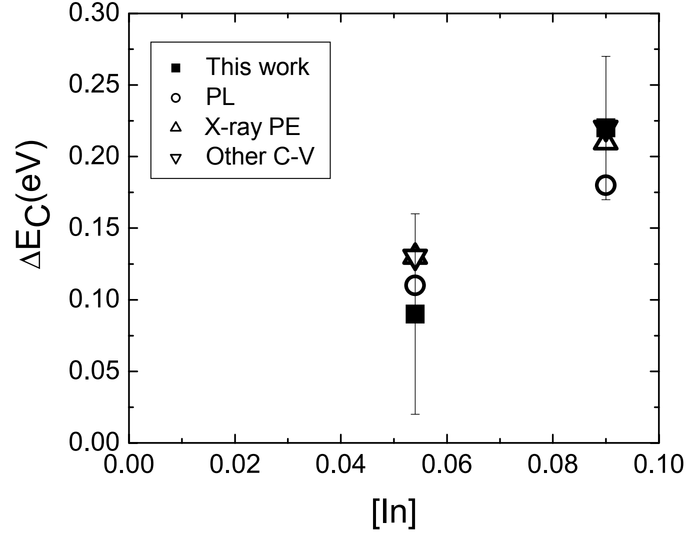

Fig. 2.7 Reported values (from Ref. 7 (Δ), Ref. 50 (○) and Ref. 53 (∇)) and our measured values (■) for ΔE_C for the $In_yGa_{1-y}N$/GaN heterojunction.

photoemission spectroscopy has yielded[51,52] a valence-band offset for the InN/GaN heterojunction of 1.05 eV, which in Ref. 7 is taken to imply a ratio $\Delta E_C : \Delta E_V$ =63:37. The conduction-band offsets corresponding to this ratio are 0.13 eV and 0.21 eV for y=0.054 and y=0.09, respectively. A capacitance-voltage analysis[53] of a p-$In_yGa_{1-y}N$/n-GaN diode to obtain the valence-band offset ΔE_V implies values for ΔE_C of 0.13 eV and 0.22 eV for the $In_{0.054}Ga_{0.946}N$ and $In_{0.09}Ga_{0.91}N$/GaN interfaces, respectively. Thus, we see that the conduction-band offsets obtained from these different

experiments, as summarized in Fig. 2.7, show very good consistency and all the results fall within the range of measurement uncertainty of this work.

2.5 Conclusion

We have described in detail the conventional capacitance-voltage profiling method and our modifications. We have introduced a comprehensive measurement model and a correction mechanism accounting for the series resistance. And we have developed a concise and more direct calculation method for determining polarization charge densities and conduction band offsets, having greatly reduced the noise effect and enhanced the calculation precision. We obtain conduction band offsets of 0.09 ± 0.07 eV and 0.22 ± 0.05 eV, respectively for $In_{0.054}Ga_{0.946}N$/GaN and $In_{0.09}Ga_{0.91}N$/GaN heterojunction interface, which are in good agreement with other reported experimental results. The band offset ratio $\Delta E_C : \Delta E_V$ is inferred to be 58:42 in this range of In composition. The polarization charge densities at the interfaces are $(1.80 \pm 0.32)\times 10^{12}$ e/cm^2 and $(4.38 \pm 0.36)\times 10^{12}$ e/cm^2, smaller than the theoretical predictions but in good agreement with values inferred from a substantial body of optical data. These results can be directly applied in $In_yGa_{1-y}N$/GaN based heterojunction structures, accounting for the small-than-expected electric field existing in the multi-quantum well structures.

Part of this chapter was published in *Journal of Vacuum Science & Technology B Microelectronics &Nanometer Structures Processing Measurement & Phenomena* 2004, H. Zhang, E. J. Miller, E. T. Yu, C. Poblenz, and J. S. Speck. The dissertation author was the first author of this paper.

Part of this chapter was published in *Applied Physics Letters* 2004, H. Zhang, E. J. Miller, E. T. Yu, C. Poblenz, and J. S. Speck. The dissertation author was the first author of this paper.

3. Analysis of Leakage Current Mechanisms in Schottky Contacts to GaN and $Al_{0.25}Ga_{0.75}N$/GaN Grown by Molecular-Beam Epitaxy

3.1 Introduction

As mentioned in the first two chapters, excessive reverse-bias leakage current in n-type Schottky contacts remains an outstanding challenge in the development of electronic devices, most notably $Al_xGa_{1-x}N$/GaN heterostructure field-effect transistor (HFET) structures, based on nitride semiconductor material grown by molecular-beam epitaxy (MBE).[54] Excessive reverse-bias leakage current through an HFET gate Schottky contact reduces device power efficiency, causes an enormous amount of heat, and also degrades device noise performance, as gate noise is typically magnified through transistor gain. Leakage conduction associated with threading screw dislocations, which are generally present in high concentrations in epitaxially grown nitride semiconductor material, has been shown to be the dominant source of high leakage currents at room temperature.[55-57] A variety of methods have been developed to suppress the influence of conductive dislocations on reverse-bias leakage currents in Schottky contacts to n-type GaN grown by MBE, including electrochemical surface treatment and conductive AFM (c-AFM) passivation.[35,36] Both methods are aiming at the blockade of each individual leakage route. The electrochemical surface treatment works well on pure GaN surface but has not been successful yet on AlGaN surface. The c-AFM passivation, however, is not suitable for industrial applications. Therefore, more detailed characterization and a more complete understanding of the relevant mechanisms of current transport are desirable both on fundamental scientific grounds

and to inform the development of simpler and more effective methods for minimizing Schottky contact leakage current in devices.

In each studies, tunneling transport appeared to be dominant at low temperatures on MBE-grown n-type GaN Schottky diodes;[58] however, it was not possible to pinpoint a single mechanism responsible for leakage current transport at room temperature, although trap-assisted tunneling and one-dimensional variable-range hopping was suggested as prominent possibilities. In this chapter, through temperature-dependent current-voltage analysis, our studies include Schottky diodes formed on $Al_xGa_{1-x}N$/GaN HFET structures as well as on n-type GaN. By confirming the role of conductive dislocations in leakage currents for both GaN and $Al_xGa_{1-x}N$/GaN structures, and enabling a single model to describe reverse-bias leakage current flow in both structures, it is possible at any given temperature between 110K and 400K to identify a single conduction mechanism – tunneling at low temperature and Frenkel-Poole emission at higher temperatures – that correctly describes current transport in both structures.

3.2 Experiment Description

All samples used in these studies were grown by MBE. The GaN sample consisted of 350 nm GaN deposited at 660°C near the upper crossover point in the Ga droplet growth regime[59] on a 2μm GaN template layer grown by metal organic chemical vapor deposition (MOCVD) on a sapphire substrate. The Ga droplet-cross over regime condition has been shown to be able to generate the highest 2DEG mobility for GaN based HFET devices. The MOCVD layer was used to relax the

dislocations formed due to the lattice mismatch between sapphire and GaN. The MBE-grown GaN layer was n-type with a dopant concentration in the mid-10^{16} cm^{-3} range. The $Al_xGa_{1-x}N$/GaN HFET structure consisted of 25nm $Al_{0.25}Ga_{0.75}N$ grown on a 1.3μm GaN layer; both layers were nominally undoped and were deposited on a 4H semi-insulating SiC substrate at 720°C. The Al content and layer thickness are typical for $Al_xGa_{1-x}N$/GaN HFET devices. SiC has better heat dissipation capabilities and better lattice match to GaN than sapphire (lattice mismatch between GaN and SiC[60] is 3% compared with 13.8% between GaN and sapphire[61]) and is often used in the HFET or HBT devices, but is also more expensive. Ti/Al metallization annealed either at 750°C for 30 sec (on GaN) or at 800°C for 3 min (on $Al_{0.25}Ga_{0.75}N$/GaN) was employed to form Ohmic contact rings, within which 125μm-diameter Ni dots were used to form Schottky contacts. Higher annealing temperature and longer annealing time are typically used for Ohmic contacts on $Al_xGa_{1-x}N$ with increasing Al content due to the reduced electron affinities of $Al_xGa_{1-x}N$ and increasing difficulty of forming good Ohmic contacts. The Ohmic contacts on both structures have shown good linearity and low resistance. Current-voltage characteristics were measured for all Schottky diodes fabricated in this manner at temperatures ranging from 110K to 400K.

Local conductivity measurements were carried out by conductive atomic force microscopy (AFM) in a modified Digital Instruments Nanoscope® IIIa MultiMode™ microscope under ambient atmospheric conditions (~20 °C with 50% relative humidity). A detailed description of the conductive AFM technique can be found in Ref. 35. Briefly, an AFM with a conductive probe tip is operated in contact mode: a highly doped diamond-coated tip is held in contact with the sample surface, keeping a

constant cantilever deflection, and acts as a Schottky contact to the sample. The tip diameter is typically about 20 nm. While scanning across the surface, forward (reverse) bias conditions are established through the application of a negative (positive) bias to an Ohmic contact on the n-type sample surface and the current through the tip is measured with an external current amplifier; in this manner, correlated topographic and current images are obtained.

3.3 Results and Discussion

3.3.1 Low Temperature Behavior

Given the large n-type barrier heights typical for Schottky contacts to GaN and $Al_xGa_{1-x}N$, we assume that thermionic emission over the Schottky barrier makes only a negligible contribution to reverse-bias current flow; otherwise, Richardson's constant would have to be unrealistically large. Fig. 3.1 shows the current density as a function of bias voltage for the GaN and $Al_{0.25}Ga_{0.75}N$/GaN Schottky diodes. At temperatures below approximately 150K, the reverse-bias leakage current is nearly independent of temperature, suggesting that tunneling is the dominant source of current flow. Because the electric field profile within the $Al_{0.25}Ga_{0.75}N$/GaN HFET structure differs from that in a conventional Schottky contact to an n-type semiconductor, we describe the current density as a function of the electric field in the barrier, which is then calculated as a function of bias voltage in each structure. In this approach, the current density is given by the Fowler-Nordheim tunneling expression,[62,63]

$$J = AE_b^2 \exp(-\frac{B}{E_b}), \qquad (3.1)$$

$$A = \frac{q^2 (m_e / m_n^*)}{8\pi h \phi_b} = 1.54 \times 10^{-6} \frac{(m_e / m_n^*)}{\phi_b} [\frac{\mathrm{A}}{\mathrm{V}^2}], \tag{3.1a}$$

$$B = \frac{8\pi \sqrt{2 m_n^* (q\phi_b)^3}}{3qh} = 6.83 \times 10^7 \sqrt{(m_n^* / m_e)(q\phi_b)^3} [\frac{\mathrm{V}}{\mathrm{cm}}], \tag{3.1b}$$

where E_b is the electric field in the semiconductor barrier, q is the fundamental electronic charge, m_e is the free electron mass, m_n^* is the conduction-band effective mass in the semiconductor, h is Planck's constant, and ϕ_b is the effective barrier height at the Schottky contact, taking into account image-force lowering of the barrier. For the GaN Schottky diode, m_n^* is taken to be that of GaN, while the electric field in Eq. (3.1a) is assumed to be that at the metal-GaN interface. For the $Al_{0.25}Ga_{0.75}N$/GaN HFET structure, m_n^* is taken to be that of $Al_{0.25}Ga_{0.75}N$ and the electric field is calculated assuming that the field is constant within the $Al_{0.25}Ga_{0.75}N$ barrier layer.

Fig. 3.2 shows a log-scale plot of J/E_b^2 as a function of $1/E_b$ for both the GaN and $Al_{0.25}Ga_{0.75}N$/GaN HFET Schottky diodes, at temperatures between 110K and 150K. The two curves shown for each diode structure are nearly identical, confirming the very weak temperature dependence of the current in this range of temperatures. From Eq. (3.1) we see that, according to the Fowler-Nordheim tunneling model, the slope of $\log(J/E_b^2)$ vs. $1/E_b$ should be independent of temperature – in good agreement with the data shown in Fig. 3.2 – and proportional to $\sqrt{m_n^* \phi_b^3}$. Assuming effective barrier heights of 0.84 eV for GaN and 1.17eV for $Al_{0.25}Ga_{0.75}N$,[7] we derive effective masses from the data in Fig. 3.2 of $(3.4 \pm 0.3) \times 10^{-3} m_e$ and $(1.8 \pm 0.2) \times 10^{-3} m_e$ for GaN and $Al_{0.25}Ga_{0.75}N$, respectively. While these effective mass values are much

smaller than typically measured or estimated values of $0.22m_e$ for GaN and $\sim 0.4m_e$ for

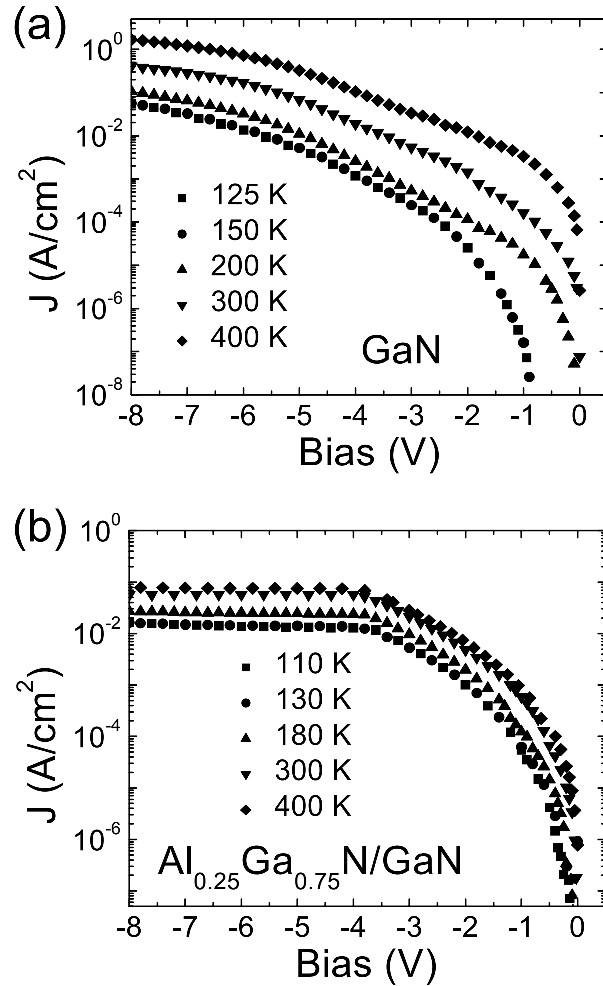

Fig. 3.1 Current density vs. bias voltage for Schottky diodes fabricated on (a) GaN and (b) $Al_{0.25}Ga_{0.75}N/GaN$ HFET epitaxial layer structures, for temperatures ranging from 110K to 400K. At low temperatures (T<150 K), leakage currents are independent of temperature and the J-V curves overlap each other.

$Al_{0.25}Ga_{0.75}N$, [64,65] they are consistent with those obtained in other, similar analyses of tunneling transport in Schottky contacts to n-type nitride semiconductors. The small

effective mass values inferred from these and other transport measurements are most

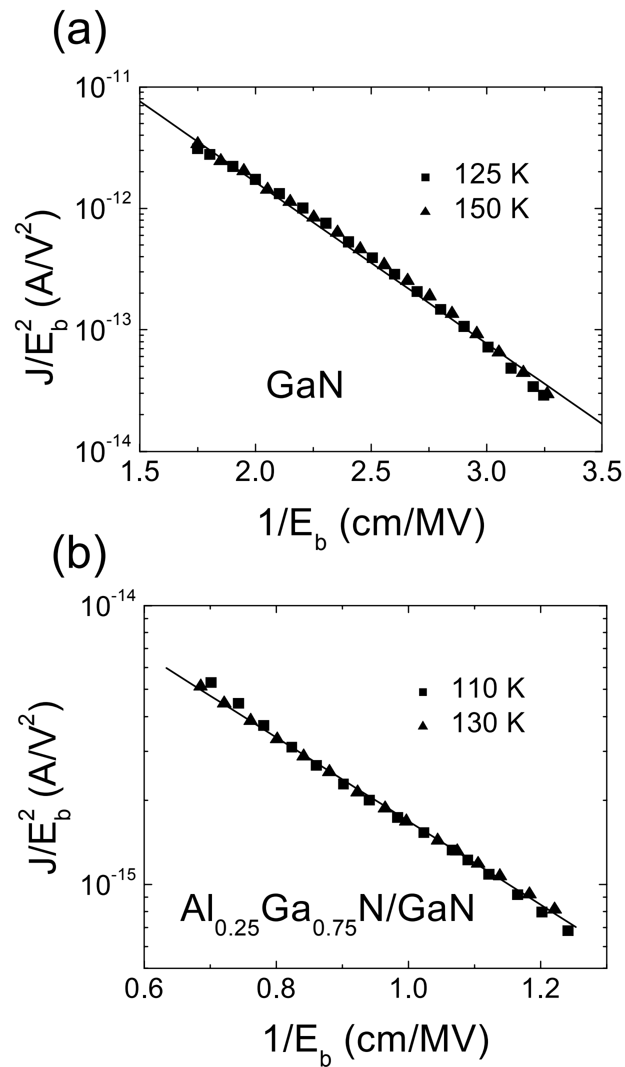

Fig. 3.2 Measured current density divided by the square of the electric field v. inverse electric field for Schottky diodes fabricated on (a) GaN and (b) $Al_{0.25}Ga_{0.75}N/GaN$ HFET epitaxial layer structures, for temperatures ranging from 110K to 150K. The straight line fitting demonstrates that at low temperatures (T<150 K), leakage current follows the Fowler-Nordheim model.

likely indicative of the presence of additional mechanisms of current transport such as

defect-assisted tunneling, which would tend to decrease the apparent value of the effective mass in an analysis of transport by tunneling. The smaller value of effective mass inferred for $Al_{0.25}Ga_{0.75}N$ compared to GaN suggests that these defect-related tunneling transport mechanisms are more prevalent in $Al_{0.25}Ga_{0.75}N$ than in GaN, as might be expected. However, the observed dependence of the current densities on electric field and their very weak dependence on temperature indicate that tunneling is, in fact, the dominant mechanism of current transport at temperatures below approximately 150K.

3.3.2 Room and High Temperature Behavior

At room temperature, reverse-bias leakage currents in Schottky contacts to n-type nitride semiconductor material grown by MBE are typically associated with the presence of conductive screw dislocations.[35,36,55,56] Fig. 3.3 shows an AFM topograph and a conductive AFM image of corresponding areas for $Al_{0.25}Ga_{0.75}N$/GaN epitaxial layer structures. The conductive AFM images were obtained under reverse-bias conditions, with a voltage of +12V applied to the sample. The leakage paths are indicated by the small dark spots in the plot and the magnitude of the leakage current is proportional to the darkness of the spots. Localized regions of high current flow associated with conductive dislocations are clearly visible, with density of approximately 1×10^{9} cm^{-2}. The conductive AFM measurement on the GaN sample has been performed by Miller,[66] with density of about 3×10^{7} cm^{-2}. The observation of these conductive dislocations confirms their role, at room temperature, in reverse-bias leakage current flow in both structures. For temperatures above 250K, the measured

macroscopic current densities in both GaN and $Al_{0.25}Ga_{0.75}N$/GaN Schottky diodes are observed to be dependent on both electric field and temperature. Specifically, as

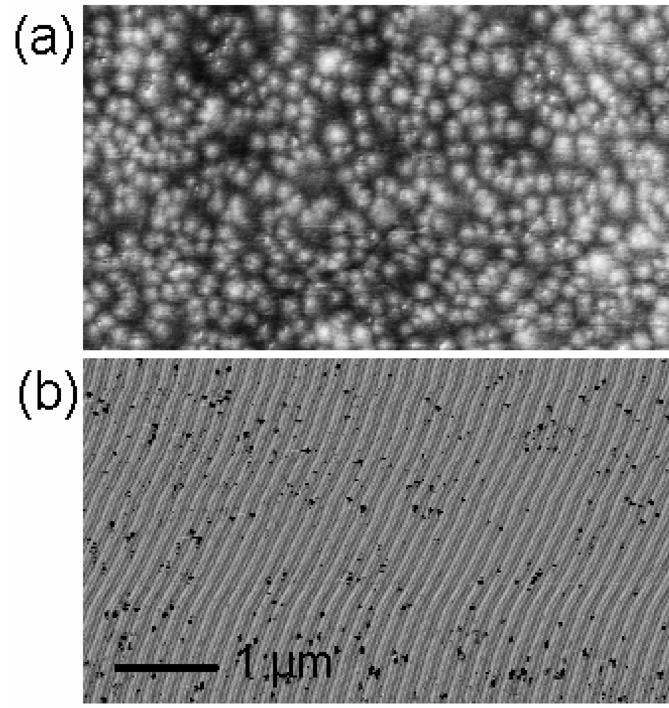

Fig. 3.3 (a) Topographic and (b) current images of the $Al_{0.25}Ga_{0.75}N$/GaN HFET structure, obtained by conductive AFM.

shown in Fig. 3.4, we observe for both diode structures a linear dependence of $\log(J/E_b)$ on $\sqrt{E_b}$, where J is the current density and E_b the electric field at the semiconductor surface; J is also observed to increase rapidly with increasing temperature. Given the dominance of dislocation-related conductivity in the leakage current at room temperature for both the GaN and the $Al_{0.25}Ga_{0.75}N$/GaN Schottky diodes, we require in our analysis that a single transport mechanism accurately describe current flow in both (although the physical parameters may differ for each, corresponding in one case to GaN and the other to $Al_{0.25}Ga_{0.75}N$). Of numerous

possibilities evaluated, only a transport model based on Frenkel-Poole emission

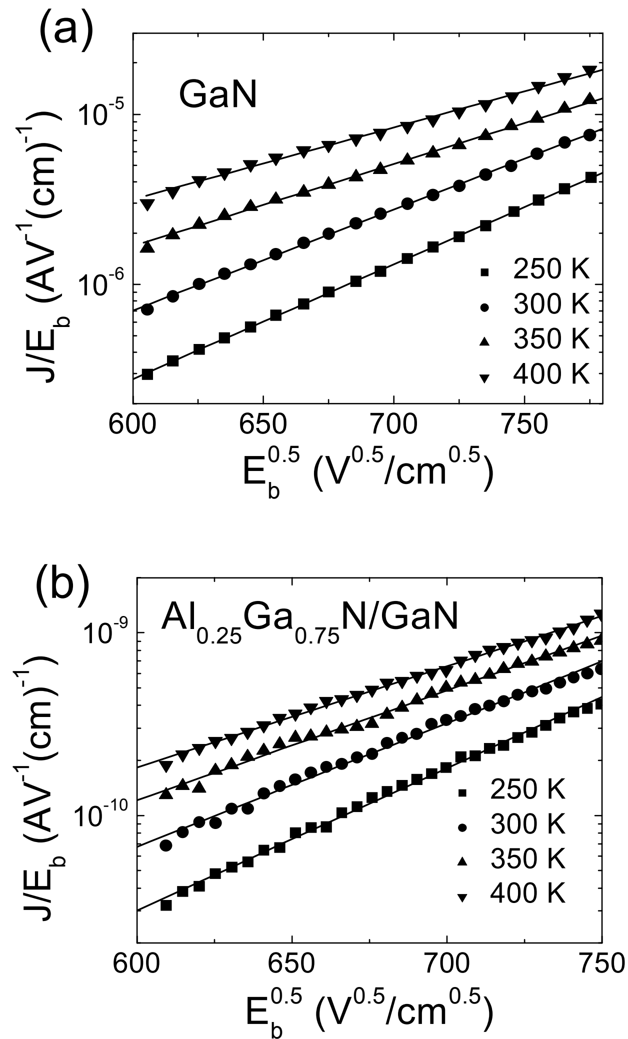

Fig. 3.4 Measured current density divided by the electric field v. square root of electric field, for Schottky diodes fabricated on (a) GaN and (b) $Al_{0.25}Ga_{0.75}N/GaN$ HFET epitaxial layer structures, for temperatures ranging from 250K to 400K.

satisfied this criterion while yielding realistic values for the necessary physical parameters.

Frenkel-Poole emission refers to electric-field-enhanced thermal emission from a trap state into a continuum of electronic states – usually, but not necessarily, the conduction band in an insulator. The current density associated with Frenkel-Poole emission is given by[67-69]

$$J = CE_b \exp\left[-\frac{q(\phi_t - \sqrt{qE_b/\pi\varepsilon_0\varepsilon_s})}{kT} \right], \tag{3.2}$$

where E_b is the electric field in the semiconductor barrier at the metal-semiconductor interface, ϕ_t is the barrier height for electron emission from the trap state, ε_s is the relative dielectric permittivity at high frequency, T is temperature, ε_0 is the permittivity of free space, and k is Boltzmann's constant. Because the electrons emitted from the trap states do not polarize the surrounding atoms, the relevant dielectric constant is that at high frequency, rather than the static dielectric constant.[68]

From Eq. (3.2) we see that, for current transport by Frenkel-Poole emission, $\log(J/E_b)$ should be a linear function of $\sqrt{E_b}$, i.e.,

$$\log(J/E_b) = \frac{q}{kT}\sqrt{\frac{qE_b}{\pi\varepsilon_0\varepsilon_s}} - \frac{q\phi_t}{kT} + \log C \equiv m(T)\sqrt{E_b} + b(T), \tag{3.3}$$

$$m(T) \equiv \frac{q}{kT}\sqrt{\frac{q}{\pi\varepsilon_0\varepsilon_s}}, \tag{3.3a}$$

$$b(T) \equiv -\frac{q\phi_t}{kT} + \log C. \tag{3.3b}$$

As shown in Fig. 3.4, the current densities in both the GaN and the $Al_{0.25}Ga_{0.75}N$/GaN diode structures are well described by the electric-field dependence of Eqs (3.2) and (3.3). Fig. 3.5 shows the functions $m(T)$ and $b(T)$, as defined in Eqs (3b) and (3c),

respectively, plotted as functions of $1/T$ for both diode structures. We see from these plots that the measured current densities exhibit both the electric field and

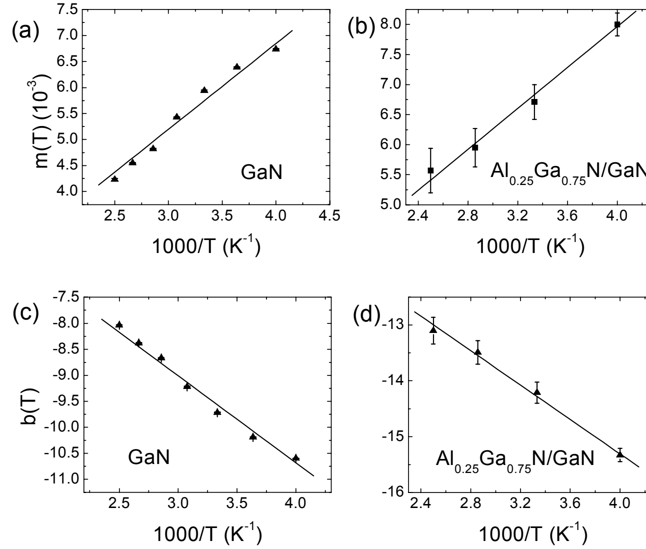

Fig. 3.5 Slopes $m(T)$ of the curves shown in (a) for GaN, and (b) for $Al_{0.25}Ga_{0.75}N$/GaN. Intercepts $b(T)$ of the curves shown in (c) for GaN, and (d) for $Al_{0.25}Ga_{0.75}N$/GaN. Data from curves not shown in Fig. 3.4 are also included.

the temperature dependence expected in Frenkel-Poole emission. Furthermore, it is possible to extract from these data values for the high-frequency relative dielectric constant ε_s and the emission barrier height ϕ_t for both the GaN and the $Al_{0.25}Ga_{0.75}N$/GaN diodes. From the slopes of $m(T)$ vs. $1/T$, plotted in Fig. 3.5(a) and Fig. 3.5(b), we obtain $\varepsilon_s^{\rm GaN} = 5.4 \pm 0.1$ and $\varepsilon_s^{\rm AlGaN} = 5.1 \pm 1.0$, and from the slopes of $b(T)$ vs. $1/T$, plotted in Figures 5(c) and 5(d), we obtain $\phi_t^{\rm GaN} = 0.33 \pm 0.01{\rm V}$ and $\phi_t^{\rm AlGaN} = 0.30 \pm 0.03{\rm V}$.

The values obtained for $\varepsilon_s^{\mathrm{GaN}}$ and $\varepsilon_s^{\mathrm{AlGaN}}$ are in good agreement with reported values[70,71] of 5.35 for GaN and 4.77 for AlN, further supporting the validity of the Frenkel-Poole emission model in describing current transport in these structures. The interpretation of the emission barrier height is less straightforward. However, given the established prominence of conductivity associated with dislocations in producing leakage currents in this range of temperatures, it is reasonable to postulate that emission either into or from dislocation-related trap states, or conduction along dislocation lines, should be the dominant factor determining the electric-field and temperature dependence of the leakage current density.

Given the emission barrier height of ~0.3V measured for both diode structures, it is unlikely that the process governing the leakage current density is emission of carriers from a dislocation-related trap state into the semiconductor conduction band. Such a scenario would require the relevant trap state to be located ~0.3eV below the conduction band-edge of GaN and $Al_{0.25}Ga_{0.75}N$ in the GaN and $Al_{0.25}Ga_{0.75}N$/GaN diode structures, respectively, which would be unexpected based on the manner in which the emission energies of specific deep-level traps typically vary among different semiconductor materials.[72] Furthermore, at the metal-semiconductor interface the trap level would be located 0.5-0.6eV above the metal Fermi level in the GaN diodes and 0.8-0.9eV above the metal Fermi level in the $Al_{0.25}Ga_{0.75}N$/GaN diodes, in which case thermal emission of carriers from the metal into the dislocation-related trap state would most likely be the key process governing leakage current flow. It is also unlikely that conduction along the dislocation line governs leakage current flow in these devices. While our prior work indicated that the temperature dependence of the

leakage current density could be adequately described using an expression for conductivity corresponding to a one-dimensional variable-range hopping model,[58] the characteristic temperature resulting from such an analysis is field-dependent and differs significantly for GaN compared to $Al_{0.25}Ga_{0.75}N$. In contrast, the Frenkel-Poole emission model yields a very accurate description of current density using clearly justifiable and realistic physical parameters.

Thus, we suggest that the process that governs leakage current flow is Frenkel-Poole emission from a state within the semiconductor – most likely a trap state near the metal-semiconductor interface – into a continuum of states associated with a conductive dislocation. Because the dependence of the current density on electric field and temperature is that of Frenkel-Poole emission rather than Schottky emission, carrier transport from the metal contact into the conductive dislocation must occur via a trap state rather than by direct thermionic emission from the metal. Furthermore, the trap state energy must be close to the metal Fermi level: if the trap level were significantly lower in energy, emission of carriers from the metal directly into conductive dislocation states would most likely dominate, while if the trap level were significantly higher in energy, emission of carriers from the metal into the trap state would also be a significant factor. Finally, the similarity of the emission barrier heights measured for GaN and $Al_{0.25}Ga_{0.75}N$ implies that the continua of states associated with conductive dislocations are approximately aligned in energy in GaN and $Al_{0.25}Ga_{0.75}N$ – as would be expected for states exhibiting deep-level behavior,[72] and required for conduction along dislocation lines across heterojunction interfaces.

If we assume for the sake of definiteness that the postulated trap state is at an energy equal to the metal Fermi level, the band-edge energies of GaN and $Al_{0.25}Ga_{0.75}N$ and the energies of the postulated trap and conducting dislocation states would be as shown in Fig. 3.6. As in our modeling of current flow, we have assumed Schottky barrier heights of 0.84eV and 1.17eV for GaN and $Al_{0.25}Ga_{0.75}N$,

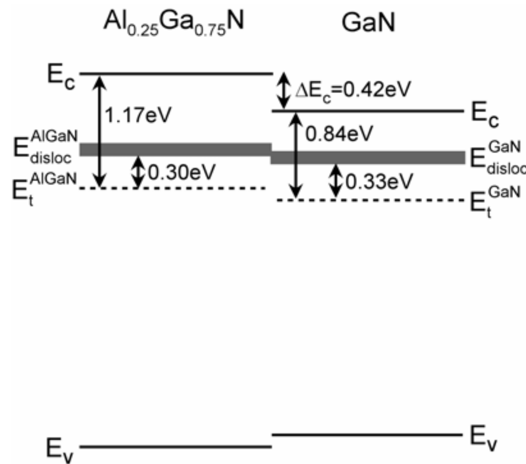

Fig. 3.6 Energy band diagram showing conduction- and valence-band-edge energies and postulated trap-state and dislocation-state energies for GaN and $Al_{0.25}Ga_{0.75}N$ based on measured emission barrier heights and reported Schottky barrier heights and band offsets.

respectively, and a conduction-band offset between GaN and $Al_{0.25}Ga_{0.75}N$ of 0.42eV based on reported experimental results of 0.37eV and 0.47eV.[73,74] As shown in the figure, based on these values the conducting dislocation states in GaN and AlGaN are aligned to within ~60meV or better, well within the experimental uncertainties of the energies used to derive the positions of the conducting dislocation states in each material. It should be noted that the alignment of these conducting dislocation states in GaN and $Al_{0.25}Ga_{0.75}N$ does not depend on the assumption that the postulated trap

state is aligned with the metal Fermi level; it is necessary only for the trap state energies in GaN and $Al_{0.25}Ga_{0.75}N$ to be similarly positioned relative to the metal Fermi level for Schottky contacts to each material, which is a very likely situation given the typical behavior of deep-level traps.

3.4 Conclusions

In summary, we have used measurements and analysis of temperature-dependent current-voltage characteristics for Schottky diodes fabricated from n-type GaN and $Al_{0.25}Ga_{0.75}N$/GaN HFET epitaxial layer structures grown by MBE to assess possible mechanisms of reverse-bias leakage current flow. At temperatures below approximately 150K, we find that tunneling is the dominant carrier transport mechanism, consistent with previously reported measurements performed on Schottky contacts to n-type GaN grown by MBE. At higher temperatures, reverse-bias leakage current flow is dominated by Frenkel-Poole emission in Schottky diodes fabricated from both GaN and $Al_{0.25}Ga_{0.75}N$/GaN epitaxial layer structures. Conductive AFM measurements performed on both epitaxial layer structures confirm that, at room temperature, carrier transport via conductive dislocations is the dominant source of reverse-bias leakage current, as expected for epitaxial material grown by MBE. A detailed analysis of the current-voltage behavior in both structures suggests that the key process in leakage current flow is emission of electrons from a trap state near the metal-semiconductor interface into a continuum of states associated with each conductive dislocation. In this model for leakage current flow, the emission barrier heights measured for the GaN and $Al_{0.25}Ga_{0.75}N$/GaN Schottky diode structures

indicate that the conductive dislocation states are aligned in energy between GaN and $Al_{0.25}Ga_{0.75}N$. This observation combined with the very accurate description of leakage current flow by Frenkel-Poole emission using realistic values for all physical parameters lends credence to the proposed model for leakage current flow in Schottky contacts formed to n-type nitride semiconductor material grown by MBE.

Most of this chapter was published in *Journal of Applied Physics* 2006, H. Zhang, E. J. Miller, and E. T. Yu. The dissertation author was the first author of this paper.

4. Demonstration and Analysis of Reduced Reverse-bias Leakage Current Via Design of Nitride Semiconductor Heterostructures Grown by Molecular-Beam Epitaxy

4.1 Motivation

As discussed Chapters 1 and 3, high levels of reverse-bias leakage current in Schottky contacts formed to n-type nitride semiconductor material grown by molecular-beam epitaxy (MBE) are a major concern in efforts to develop high-performance $Al_xGa_{1-x}N$/GaN heterostructure field-effect transistor (HFET) structures based on MBE-grown material.[54,75] A number of studies have helped to elucidate the nature of these leakage currents, which have been shown to arise due to the presence of highly conductive screw dislocations,[55-57,76] and guide the development of strategies for their mitigation based on selective suppression of current flow associated with these dislocations via local surface oxidation.[36,66]

In the previous chapter, studies of temperature-dependent current-voltage characteristics for Schottky diodes fabricated from MBE-grown n-type GaN and $Al_xGa_{1-x}N$/GaN HFET structures have revealed that, at temperatures of ~250K and above, Frenkel-Poole emission of electrons from near-surface traps in the nitride semiconductor material into conductive dislocation states is the key process governing reverse-bias leakage current flow.[77] The Frenkel-Poole emission process is a strong function of the electric field at the metal-semiconductor interface, suggesting that design of a nitride heterostructure in which the electric field at that interface is appropriately engineered could serve as a highly effective approach for suppressing

leakage current flow via conductive dislocations. This approach could be adopted in MBE-grown $Al_xGa_{1-x}N$/GaN HFET devices with little influence on threshold voltage and channel charge density.

In the following, we will show that incorporation of a thin GaN layer capping the conventional $Al_xGa_{1-x}N$ /GaN HFET epitaxial layer structure, by reversing the direction of the electric field at the metal-semiconductor interface compared to that present in the conventional HFET structure, serves to reduce the reverse-bias leakage current in Schottky contacts by suppressing carrier transport into conductive dislocation states. At low to moderate reverse-bias voltages, the presence of the GaN cap layer causes the electric field at the metal-semiconductor interface to oppose the flow of electrons into conductive dislocation states, thereby eliminating the primary source of reverse-bias leakage current. At large reverse-bias voltages, leakage current conduction via dislocations does occur, but is significantly suppressed due to the reduced magnitude of the electric field compared to that in a conventional HFET structure.

It should be noted that this mechanism for reverse-bias leakage current suppression in structures containing such a GaN capping layer is different from that reported in earlier studies of similar structures grown by metal organic vapor phase epitaxy (MOVPE).[78] In these earlier studies, the principal mechanism for reduction of Schottky contact leakage current was the increase in effective barrier height induced by the presence of negative polarization charge at the upper GaN/ $Al_xGa_{1-x}N$ interface, as highly conductive screw dislocations are not found to be present in nitride semiconductor material grown by techniques other than MBE.[79,80] The suppression of

leakage current flow in MBE-grown nitride material described here is associated specifically with the nature of the electric field at the metal-semiconductor interface and the suppression of the Frenkel-Poole emission process, and is not dependent on the barrier height itself.

4.2 Experiment Description

The samples used in these studies were grown by MBE, with the epitaxial layer structures and schematic energy-band-edge diagrams shown in Fig. 4.1. The conventional HFET structure, shown in Fig. 4.1(a), consisting of a 25nm $Al_{0.25}Ga_{0.75}N$ barrier layer atop a 1.3µm GaN channel layer, is from the previous study in the third chapter. Both layers are nominally undoped, and the structure was grown on an AlN nucleation layer deposited at 720°C on a 4H semi-insulating SiC substrate. We listed the structure here immediately adjacent to the GaN-capped HFET structure, shown in Fig. 4.1(b), as a direct comparison. The GaN-capped HFET consists of a 6nm GaN cap layer grown on a 23nm $Al_{0.25}Ga_{0.75}N$ layer atop a 1.2µm GaN channel layer. As in the first structure in Fig. 4.1(a), all layers are nominally undoped and were grown on an AlN nucleation layer deposited on a 4H semi-insulating SiC substrate. The two different structures have the same Al content, almost identical barrier thickness and very similar growth condition and doping, and therefore are characterized by very similar properties such as threshold voltage and channel charge density. Ohmic contact rings were formed using Ti/Al/Ti/Au metallization deposited by electron-beam evaporation and annealed at 800°C for 1 minute (GaN-capped HFET structure) or 3

minutes (conventional HFET structure). Schottky contacts consisting of 125μm-diameter dots were then formed within the Ohmic contact rings using Ni metallization

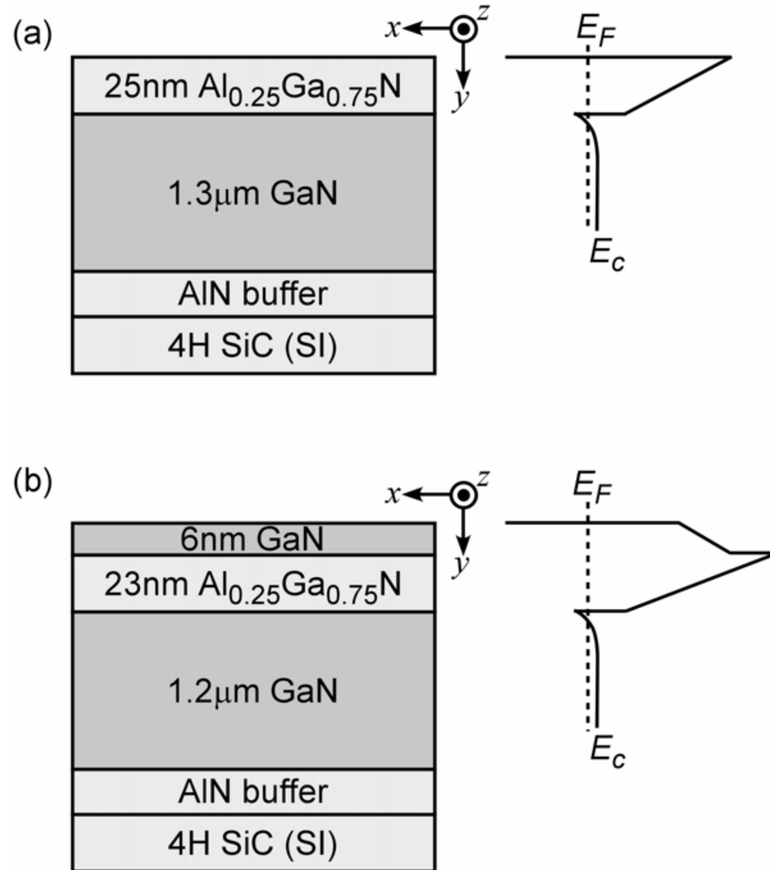

Fig. 4.1 Epitaxial layer structure and schematic energy-band-edge diagram for (a) conventional $Al_{0.25}Ga_{0.75}N$/GaN HFET structure, and (b) GaN/$Al_{0.25}Ga_{0.75}N$/GaN HFET structure incorporating a GaN cap layer. The two structures have the same Al content, almost identical barrier thickness and doping.

and a conventional liftoff process, same as described in the third chapter. Current-voltage characteristics were measured for all Schottky diodes fabricated in this manner at temperatures ranging from 250K to 400K.

Local conductivity measurements were carried out by conductive atomic force microscopy (c-AFM) in a modified Digital Instruments Nanoscope® IIIa

MultiMode™ microscope under ambient atmospheric conditions (~20°C with 50% relative humidity). The operation of c-AFM is the same as described in the third chapter.

Numerical modeling was used to determine the energy-band-edge profiles and electric field distributions in these structures as functions of bias voltage applied to the Schottky contact. Specifically, two-dimensional simulations of potential, carrier, and electric field distributions were performed using Silvaco simulation software. Two-dimensional simulations were required to enable us to model accurately the vertical electric field near the metal-semiconductor Schottky interface at bias voltages below the threshold voltage for accumulation of electrons in the two-dimensional electron gas (2DEG) formed at the lower GaN/ $Al_{0.25}Ga_{0.75}N$ interface.

4.3 Results and Discussion

4.3.1 Macroscopic Demonstration and Explanations

Fig. 4.2 shows reverse-bias current-voltage characteristics for Schottky diodes fabricated from the conventional (also see Chapter 3, Fig. 3.1(b)) and GaN-capped HFET structures at temperatures ranging from 250K to 400K. At 300K, the reverse-bias leakage currents are reduced by approximately one to three orders of magnitude, depending on the bias voltage, in the GaN-capped HFET structure compared to those in the conventional HFET; the reduction is most pronounced at bias voltages of 0V to -4V.

To elucidate the origin of the reduction in leakage current in the GaN-capped structure, we have used two-dimensional numerical simulations to determine the

energy-band-edge profiles, carrier distributions, and electric fields in both structures,

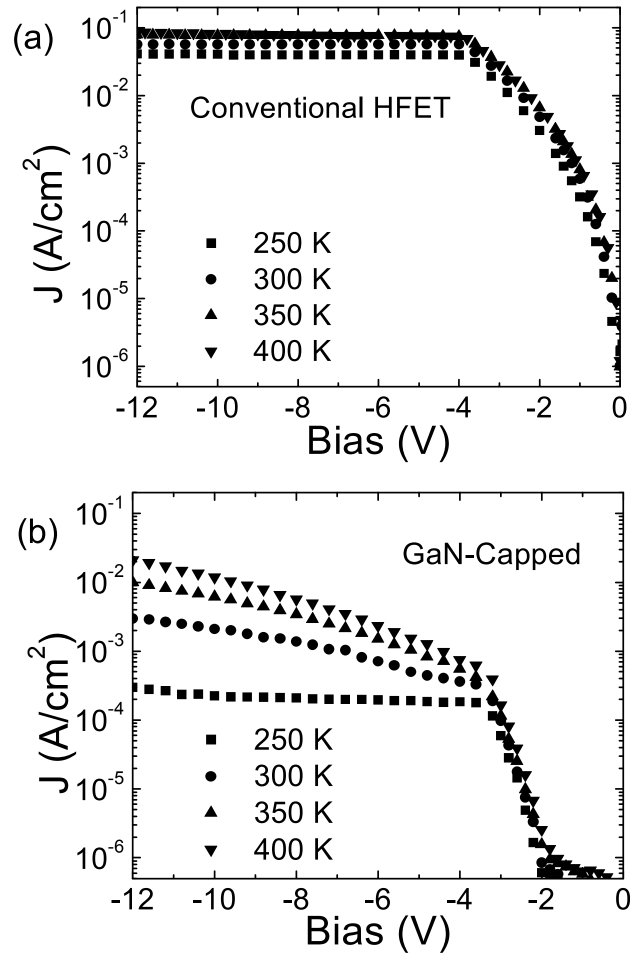

Fig. 4.2 Reverse-bias current-voltage characteristics at temperatures ranging from 250K to 400K for (a) conventional $Al_{0.25}Ga_{0.75}N$/GaN HFET structure, and (b) GaN/$Al_{0.25}Ga_{0.75}N$/GaN HFET structure incorporating a GaN cap layer. Leakage currents in GaN-capped HFET structure are reduced by approximately 3 to 4 orders of magnitude and the reduction is most prominent at biases between 0 V and -4 V.

as shown in Fig. 4.3. In the simulation, the Schottky contact dot was approximated by a 125μm wide metal strip with a work function of 5.0eV. The concentric Ohmic

contact ring was represented by two parallel metal strips 120μm in width located on each side of the Schottky contact, separated from the Schottky contact by 17.5μm as in the actual fabricated Schottky diodes. The epitaxial layer structures were as shown in Fig. 4.1, with a donor concentration of 5×10^{16}cm^{-3}, representing unintentional background doping, in each layer. A polarization charge density of 1.15×10^{13}cm^{-2} was assumed to be present at the GaN/$Al_{0.25}Ga_{0.75}N$ interfaces.[7, 27] These simulations enabled us to determine accurately the vertical electric field $E_{y,i}$ at the metal-semiconductor Schottky interface over the entire range of bias voltages studied experimentally.

Fig. 4.3(a) shows the conduction-band-edge energy profile for the GaN-capped structure at bias voltages of 0V, -2V, and -4V. At 0V and -2V, the electric field $E_{y,i}$ at the metal-semiconductor interface is positive, i.e., directed away from the interface into the semiconductor, whereas in the conventional HFET structure $E_{y,i}$ would point in the opposite direction. At -4V, however, $E_{y,i}$ at the interface is nearly zero, while at more negative bias voltages $E_{y,i}$ is in the same direction as in the conventional HFET structure. Fig. 4.3(b) shows the electron concentration in the 2DEG, n_s, as a function of bias voltage for the conventional and GaN-capped HFET structures. The threshold voltages for both structures are at approximately -4V, although the carrier concentrations in the GaN-capped structure are systematically slightly lower than in the conventional HFET structure due to partial depletion of electrons by the negative polarization charge at the upper GaN/$Al_{0.25}Ga_{0.75}N$ interface in the former.[78] Fig. 4.3(c) shows the vertical electric field, $E_{y,i}$, at the metal-semiconductor interface as a function of bias voltage. A comparison of Fig. 4.3(b) and Fig. 4.3(c) shows that the

"kinks" in $E_{y,i}$ as a function of bias voltage near -4V coincide with the threshold voltages for electron accumulation in the 2DEG in each structure; these "kinks" occur because at voltages below the threshold voltage, the field penetrates below the 2DEG channel and there is a substantial lateral component to the electric field between the Schottky and Ohmic contacts, reducing the dependence of $E_{y,i}$ on applied bias. For the conventional HFET structure, we see that $E_{y,i}$ is negative, i.e., the electric field is directed out of the semiconductor, at all bias voltages shown. For the GaN-capped structure, $E_{y,i}$ is negative only for bias voltages below approximately -4V, and in this range of voltages $E_{y,i}$ is much smaller in magnitude than in the conventional HFET structure.

The size and direction of $E_{y,i}$ at the metal-semiconductor interface is significant because of the nature of the Frenkel-Poole emission process that dominates reverse-bias leakage current flow in these structures at the temperatures shown here.[77] Specifically, the current density in the Frenkel-Poole emission model is given by Eq. (3.2) and repeated here:

$$J = CE_{y,i} \exp\left[-\frac{q(\phi_t - \sqrt{-qE_{y,i} / \pi\varepsilon_0\varepsilon_s})}{kT} \right], \qquad (4.1)$$

where C is a constant, q is the electron charge magnitude, ϕ_t is the electron emission barrier height, ε_s is the high frequency dielectric permittivity, ε_0 is the permittivity of free space, k is Boltzmann's constant, and T is the temperature. Our earlier studies established values for ϕ_t of 0.33±0.01V and 0.30±0.03V for GaN and $Al_{0.25}Ga_{0.75}N$, respectively, and for ε_s of 5.4±0.1 and 5.1±1.0 for GaN and $Al_{0.25}Ga_{0.75}N$,

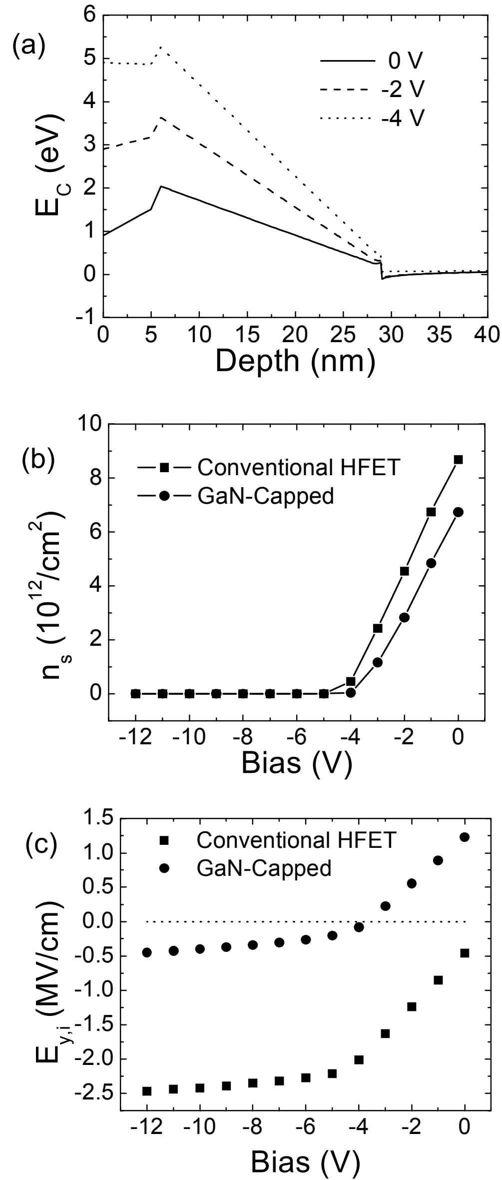

Fig. 4.3 (a) Conduction-band-edge energy profile for the GaN-capped HFET structure at bias voltages of 0V, -2V, and -4V. (b) Electron sheet concentration in the channel of the conventional and GaN-capped HFET structures, as functions of bias voltage. (c) Vertical electric field at the metal-semiconductor Schottky interface of the conventional and GaN-capped HFET structures, as functions of bias voltage.

respectively.[77] Because of the dependence of J on $E_{y,i}$ in the exponential function in Eq. (4.1), it is anticipated that reversal of the sign of $E_{y,i}$, as occurs in the GaN-capped structure for bias voltages above -4V, will dramatically suppress the Frenkel-Poole emission process and consequently leakage current flow via conductive dislocations; the reduction in magnitude of $E_{y,i}$ in the GaN-capped structure at more negative bias voltages should, while not eliminating dislocation-related leakage current, substantially reduce its magnitude.

Our previous studies[77] have established that, at moderate negative bias voltages, reverse-bias leakage current flow in the conventional HFET structure within the temperature range studied here is well described by the Frenkel-Poole emission model. For large negative bias voltages the Frenkel-Poole emission model is no longer physical, as the large magnitude of $E_{y,i}$ yields a negative emission barrier, for which the current should saturate rather than continue to increase exponentially. We believe this explains the very weak dependence of leakage current density on bias voltage, and correspondingly on electric field, for bias voltages below approximately -4V in the conventional HFET structure, which is in contrast to the significant dependence of leakage current density on bias voltage in this same voltage range for the GaN-capped structure, in which the magnitude of $E_{y,i}$ is much smaller.

To determine the applicability of the Frenkel-Poole emission model, and hence the influence of leakage current flow via conductive dislocations, in the GaN-capped structure, we consider the measured current density as a function of temperature for this structure, as shown in Fig.4.4. Fig. 4.4(a) shows current density as a function of inverse temperature at -8V bias; as predicted by Eq. (4.1), log J varies linearly with

$1/T$, with a slope determined by least-squares fitting to be 1000±70K. From this value

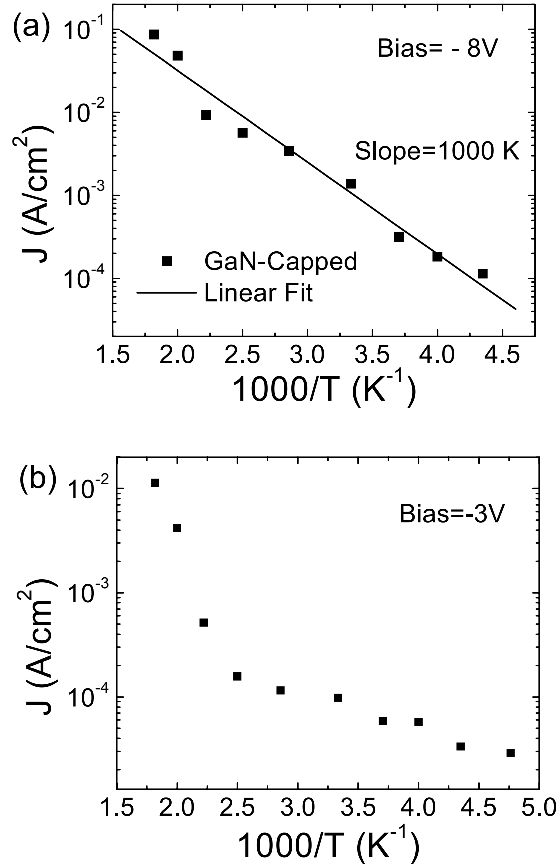

Fig. 4.4 Current density as a function of inverse temperature for the GaN-capped HFET structure at bias voltages of (a) -8V and (b) -3V.

for the slope, combined with an electric field determined from Fig. 4.3(c) of -3.4×10^5V/cm at -8V and ε_s=5.4 for GaN, we derive a barrier height ϕ_t=0.38±0.03V. Repeating this analysis for bias voltages ranging from -4V to -12V, we obtain an average value for ϕ_t of 0.37±0.1V, which is in good agreement with the value 0.33±0.01V determined independently in our earlier studies. This analysis confirms that in this range of bias voltages, the reverse-bias leakage current in the GaN-capped

structure is, as expected, dominated by the Frenkel-Poole emission process and carrier transport along conductive dislocations. However, due to the reduced magnitude of the electric field $E_{y,i}$ compared to that in a conventional AlGaN/GaN HFET structure at the same bias voltage, the reverse-bias leakage current is substantially reduced.

Fig. 4.4(b) shows current density as a function of inverse temperature for the GaN-capped structure at -3V bias. From Fig. 4.3(c), we see that at this bias voltage, the direction of the electric field is opposite to that at more negative bias voltages; consequently, the Frenkel-Poole emission process and current flow along conductive dislocation states are suppressed, and the linear dependence of log J on $1/T$ is not observed. At this bias voltage, and in general for bias voltages at which the electric field $E_{y,i}$ is directed towards the semiconductor, the dominant source of reverse-bias leakage current in conventional $Al_xGa_{1-x}N$/GaN HFET structures grown by MBE is therefore suppressed, leading to a large reduction in leakage current.

4.3.2 Microscopic Demonstration and Explanations

The applicability of the Frenkel-Poole emission model in describing, quantitatively, reverse-bias current flow over a wide range of bias voltages provides very clear evidence that the influence of the GaN cap layer on current flow occurs predominantly via suppression of Frenkel-Poole emission from near-surface trap states into dislocations, rather than through other possible effects such as a reduction in threading dislocation density, or some other improvement in structural quality, at the metal-semiconductor interface. However, to confirm further the effect of the GaN capping layer in suppressing current flow into and along conductive dislocations, we

examine AFM topographs and conductive AFM current images of both the

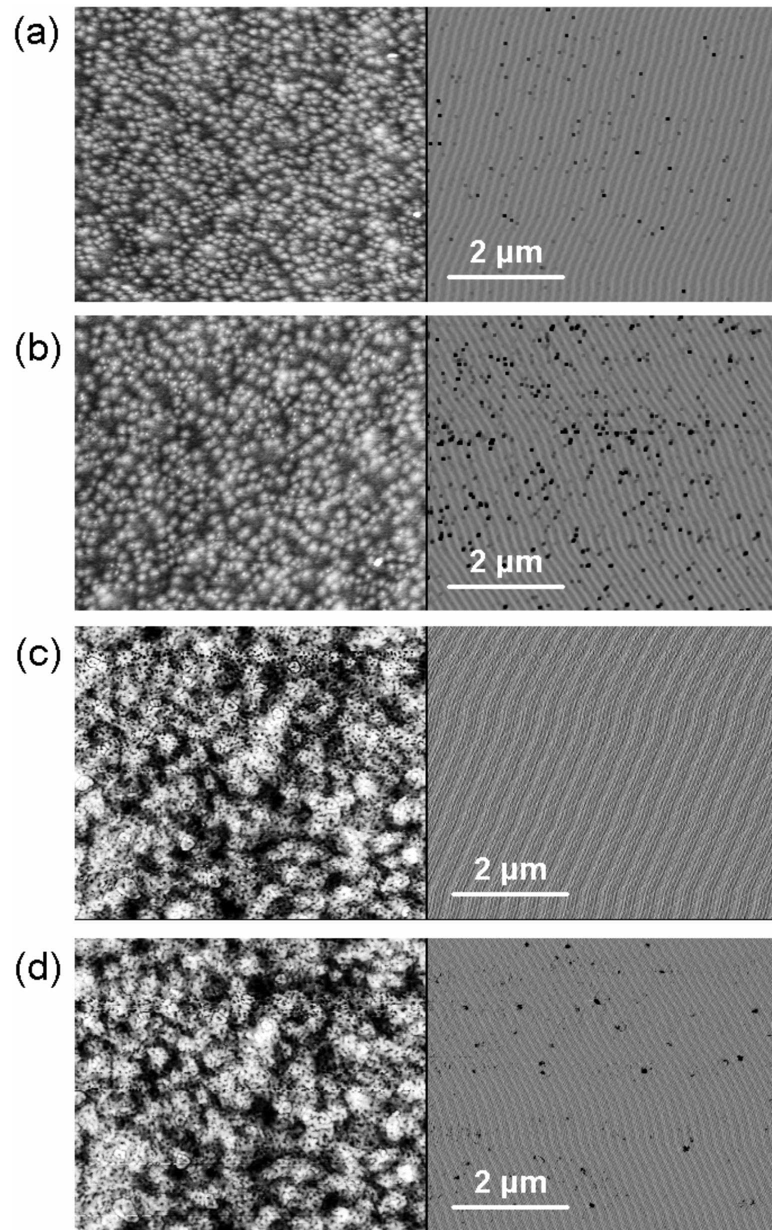

Fig. 4.5 Topographic (left) and current (right) images of conventional and GaN-capped HFET structures obtained via conductive atomic force microscopy. (a) conventional HFET structure at -8V bias. (b) conventional HFET structure at -12V bias. (c) GaN-capped HFET structure at -8V bias. (d) GaN-capped HFET structure at -12V bias.

conventional and GaN-capped HFET structures. Fig. 4.5(a)-(b) show topographic and

current images of the conventional HFET structure obtained at bias voltages of -8V and -12V, respectively, applied to the conducting probe tip. In both current images, highly conductive regions corresponding to screw dislocations are clearly visible as dark spots (negative current) in the images, with visible conductive dislocation densities of $3.6\times10^{8}cm^{-2}$ at -8V and $1.0\times10^{9}cm^{-2}$ at -12V. Fig. 4.5(c)-(d) shows topographic and current images of the GaN-capped HFET structure, also obtained at bias voltages of -8V and -12V, respectively. No conductive dislocations are visible in the image obtained at -8V, while at -12V a conductive dislocation density of approximately $1.5\times10^{8}cm^{-2}$ is evident.

We interpret the results shown in Fig. 4.5 as follows. In the conventional HFET sample, the localized current paths imaged at negative bias voltage confirm the prominence of conductive screw dislocations in giving rise to the leakage currents observed, as shown in Fig. 4.2(a), in macroscopic Schottky diodes fabricated from those structures. The observable leakage path density increases substantially between -8V and -12V, despite only a minimal change in macroscopic Schottky diode leakage current between these voltages. We attribute this to two factors. First, at -8V the current observed at each point near a conductive dislocation is near the threshold of detection in our system (approximately 0.1pA); as the bias voltage becomes more negative, probabilistically a greater number of conductive dislocations exceed the threshold for detection, causing the observable leakage path density to increase despite a minimal change in macroscopic leakage current. Second, the pixel spacing for the images shown in Fig. 4.5 is approximately 40nm, which combined with a typical tip radius of 10-20nm means that the probe tip often may not sample the location directly

above the dislocation core. The maximum electric field above the dislocation core will vary depending on the distance between the tip and the dislocation, but will increase in magnitude with increasing bias voltage magnitude. Thus, at more negative bias voltages the likelihood of the electric field above a dislocation core exceeding the value required for the current to exceed our detection threshold will increase, leading to a corresponding increase in observable leakage current density. However, the detection probability increases very rapidly with electric field $E_{y,i}$, and therefore fairly rapidly with bias voltage, eventually saturating at unity – at which point any further increase of the reverse bias voltage would not increase the concentration of detected leakage paths.

In the GaN-capped HFET sample, these same considerations apply, but due to the reduced magnitude of the electric field above the dislocation core at a given bias voltage, compared to that present for the conventional HFET structure, a substantially larger magnitude bias voltage is required to attain current levels in each leakage path that exceed our detection threshold. Thus, the conductive dislocations become visible in conductive AFM current images only at bias voltages of -12V and below in the GaN-capped HFET structure, corresponding to a vertical electric field $E_{y,i}$ of -5×10^5V/cm; this is consistent with our earlier studies of local current flow in n-type GaN epitaxial layers, in which the minimum electric field at which conductive dislocations were visible was similar in magnitude.[66] Thus we observe directly by conductive AFM that incorporation of the GaN capping layer in the HFET structure reduces the current flow associated with an individual conductive dislocation very substantially at a given bias voltage compared to that for a conventional HFET

structure, thereby confirming the role of the GaN capping layer in suppressing reverse-bias leakage currents associated with conductive dislocations in MBE-grown nitride material. More generally, these results indicate that the direction and magnitude of the electric field at a metal-semiconductor interface can be engineered in the design of MBE-grown nitride semiconductor heterostructures to suppress reverse-bias Schottky leakage currents arising from the presence of conductive dislocations.

4.4 Conclusions

In summary, we have demonstrated a strategy for reduction of leakage currents in Schottky contacts to MBE-grown nitride-based HFET structures based on engineering of the electric field near the metal-semiconductor Schottky interface to reduce Frenkel-Poole emission into conductive dislocations. Building upon prior studies in Chapter 3 that elucidated basic mechanisms of leakage current in MBE-grown nitride semiconductor material, we have compared temperature-dependent current-voltage characteristics and scanned probe imaging of a conventional HFET structure and an HFET structure incorporating a GaN capping layer. The reverse-bias leakage current is found to be reduced by approximately one to three orders of magnitude in the structure incorporating the GaN capping layer, with the reduction being most pronounced at small reverse bias voltages. Two-dimensional numerical simulations of these device structures are used to determine the electric field at the metal-semiconductor interface as a function of bias voltage, and the current-voltage characteristics of the GaN-capped HFET structure are analyzed in terms of the Frenkel-Poole emission mechanism shown in prior work to be the key process in

leakage current flow via conductive dislocations. At large negative bias voltages, for which the electric field is directed towards the semiconductor, the leakage current in the GaN-capped structure is well described by the Frenkel-Poole emission model, indicating that current flow via conductive dislocations dominates; however, the magnitude of current observed is much lower than in the conventional HFET structure, as predicted by the Frenkel-Poole emission model based on the reduced magnitude of the electric field in the GaN-capped structure. At smaller negative bias voltages, for which the electric field is directed away from the semiconductor, the leakage current in the GaN-capped structure is dramatically reduced compared to that in the conventional HFET, and the observed temperature dependence of the current is not consistent with Frenkel-Poole emission – indicating that a different physical mechanism is contributing to the current flow. AFM topographic images and conductive AFM current images confirm that current flow via dislocations dominates reverse-bias leakage in the conventional HFET structure and, at sufficiently large negative bias voltages, in the GaN-capped structure, while at smaller reverse-bias voltages the contribution of conductive dislocations to leakage currents in the GaN-capped structure is suppressed. These results also suggest an obvious, more general strategy that can be employed to reduce reverse-bias Schottky leakage currents in MBE-grown nitride semiconductor material and devices.

Most of this chapter was published in *Journal of Applied Physics* 2006, H. Zhang, and E. T. Yu. The dissertation author was the first author of this paper.

5. Conclusion

The successful characterization of the surface and interface properties of GaN and its alloys will be beneficial not only to scientific interests but also to their future application in electronic and opto-electronic applications. The work presented in this thesis addresses issues pertaining to both the fundamental materials sciences of nitride semiconductors, and their applications in electronic devices, most notably $Al_xGa_{1-x}N$/GaN HFET's. We have modified the conventional capacitance-voltage profiling method to derive a more precise result with high accuracy on polarization charge densities and conduction band offsets at $In_yGa_{1-y}N$/GaN heterojunction interfaces. The comprehensive measurement model, series resistance correction procedure and a more direct calculation algorithm can be readily applied in similar structural analysis. We obtain conduction band offsets of 0.09 ± 0.07 eV and 0.22 ± 0.05 eV, respectively for $In_{0.054}Ga_{0.946}N$/GaN and $In_{0.09}Ga_{0.91}N$/GaN heterojunction interface, which are in good agreement with other reported experimental results. The band offset ratio $\Delta E_C : \Delta E_V$ is inferred to be 58:42 in this range of indium composition. We obtain the polarization charge densities at the interfaces of $(1.80 \pm 0.32) \times 10^{12}$ e/cm^2 and $(4.38 \pm 0.36) \times 10^{12}$ e/cm^2, smaller than the theoretical predictions but in good agreement with values inferred from optical experimental data and consistent with the small-than-expected electric field existing in the multi-quantum well structures. The results of the work will be critical in the analysis, design and engineering of the GaN/$In_yG_{1-y}N$ heterojunction devices and quantum well devices.

We have used measurements and analysis of temperature-dependent current-voltage characteristics for Schottky diodes fabricated from n-type GaN and

$Al_{0.25}Ga_{0.75}N$/GaN HFET epitaxial layer structures grown by MBE to assess possible mechanisms of reverse-bias leakage current flow. We find that for both structures at temperatures below approximately 150 K, tunneling is the dominant carrier transport mechanism. At higher temperatures, reverse-bias leakage current flow is dominated by Frenkel-Poole emission. Conductive AFM measurements performed on both epitaxial layer structures confirm that, at room temperature, carrier transport via conductive dislocations is the dominant source of reverse-bias leakage current. The key process in leakage current flow is the emission of electrons from a trap state near the metal-semiconductor interface into a continuum of states associated with each conductive dislocation. The emission barrier heights measured for the GaN and $Al_{0.25}Ga_{0.75}N$/GaN Schottky diode structures indicate that the conductive dislocation states are aligned in energy between GaN and $Al_{0.25}Ga_{0.75}N$. This observation combined with the very accurate description of leakage current flow by Frenkel-Poole emission using realistic values for all physical parameters lends credence to the proposed model for leakage current flow in Schottky contacts formed to n-type nitride semiconductor material grown by MBE.

Finally, based on this knowledge, we have demonstrated a strategy for reduction of leakage currents in Schottky contacts to MBE-grown nitride-based HFET structures by engineering the electric field near the metal-semiconductor Schottky interface to reduce Frenkel-Poole emission into conductive dislocations. We have compared temperature-dependent current-voltage characteristics and conductive AFM imaging of an HFET structure incorporating a GaN capping layer with those of a conventional HFET structure. The reverse-bias leakage current is found to be reduced

by approximately one to three orders of magnitude in the structure incorporating the GaN capping layer, with the reduction being most pronounced at small reverse bias voltages due to the complete suppression of Frenkel-Poole emission at small reverse bias. At large negative bias voltages, the leakage current in the GaN-capped structure starts to follow the Frenkel-Poole emission model, however, the magnitude of current observed is much lower than in the conventional HFET structure, as predicted by the Frenkel-Poole emission model based on the reduced magnitude of the electric field in the GaN-capped structure. AFM topographic images and conductive AFM current images at room temperature confirm that current flow via dislocations dominates reverse-bias leakage in the conventional HFET structure and, at sufficiently large negative bias voltages, in the GaN-capped structure, while at smaller reverse-bias voltages the contribution of conductive dislocations to leakage currents in the GaN-capped structure is completely suppressed. These results provide an obvious, more general strategy that can be employed to reduce reverse-bias Schottky leakage currents in MBE-grown nitride semiconductor material and devices.

Appendix—Negative Index Material Application, Fabrication and Characterization

A.1 Introduction

Negative Index Material (NIM), also called Left Handed (LH) material, Double Negative Material (DNG), or backward wave medium, refers to material with both negative electric permittivity ε and negative magnetic permeability μ. The unique properties of NIM have sparked intense interest since the first lab demonstration by Smith, et al.[18]

The idea of NIM can be traced back to the 1960s when the Russian scientist V. G. Veselago[16] was investigating the then hypothetical properties of materials with simultaneous negative ε and negative μ. Negative ε was known to readily exist inside metals when electron plasmas were excited, but negative μ did not exist in nature and was generally regarded as extremely difficult to be achieved, if not totally impossible. So NIM had never attracted significant attention until it was reinvestigated by Pendry et. al. in 1999. Using the double split ring (DSR) resonator structure[17], Pendry was able to demonstrate mathematically that an effective negative μ could be obtained. Thus, Pendry offered the possibility of making NIM and he further discussed the benefits of using NIM in near-field amplification—namely, the “perfect lens”.[81] Based on this theory, Smith et al.[18] fabricated the first NIM structure in 2000 using the DSR structure and metal thin wires and observed negative refraction, one of the most striking properties of NIM, in a narrow spectrum range around 10 GHz. As the dimensions of the structure are scaled down, this negative refraction can be blue-shifted into a higher spectral range. Up to now, negative μ in the THz range has

already been demonstrated[82] and negative refraction in the optical region is also looking promising.[83]

NIM has been intensively studied in the microwave region because of its potential applications in the microwave components, circuits and systems. Itoh et. al. have pursued fabrication of NIM using a specially engineered transmission line structure.[19,20] Novel microwave devices such as coupled-line coupler with arbitrary coupling can actually be made based on this TL model and approach.[84] Other potential applications of NIM in microwave systems include antennas[21] or TL-based leaky wave antennas[22]. This appendix is devoted to yet another possible application—compact microwave resonator and associated practical issues. It is demonstrated that, by incorporating NIM in resonator cavities, the structure size can be greatly reduced.

An additional practical aspect of NIM is that the NIM fabricated by Smith is anisotropic, i.e., the negative refraction occurs only when the incident electromagnetic waves are polarized along certain directions, which would largely limit its application. Furthermore, the alignment of the unit cell structures is difficult and labor-intensive. Thus we also discuss a possible new way of fabricating isotropic NIM based on Pendry's and Smith's theory and on a new resonant structure design named single split ring resonator with overlapping arms (SSROA). Preliminary advances in fabrication will be described here and some potential characterization methods will be discussed as well.

A.2 Possible Application of Negative Index Material in Cavity Resonator

As mentioned in Section A.1, the possible applications of NIM in the microwave field have aroused a very broad interest. Recently, ideas for the application of NIM's in microwave resonators have been presented and analyzed theoretically[85]. These studies showed that the size of a one-dimensional (1-D) resonant structure does not explicitly depend on wavelength λ, and therefore it is possible to shrink the dimension of the microwave resonator below one half wavelength, the minimum size of a microwave resonator fabricated from conventional material. In this paper, we extend this analysis to more complex three dimensional (3-D) cavity structures and discuss the design rule.

A.2.1 Review of 1-D DPS-DNG Cavity

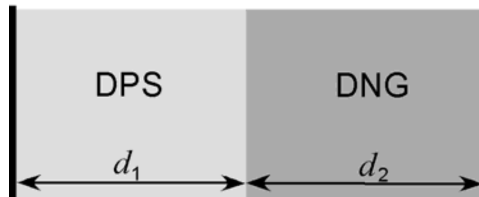

Fig. A.2.1 1-D DPS-DNG resonant structure

The 1-D DPS-DNG resonator structure described in Ref. 85 consists of one layer of double positive material (DPS) and one layer of double negative material (DNG) as shown in Fig. A.2.1. The electromagnetic (EM) field inside the structure is given by:

$$E_{x1}(z) = E_0 \sin(k_2 d_2)\sin(k_1 z)$$

$$H_{y1}(z) = -\frac{j}{Z_{TEM1}} E_0 \sin(k_2 d_2)\cos(k_1 z) \quad , \quad \text{for } 0 \le z \le d_1, \qquad \text{(A.2.1)}$$

$$E_{x2}(z) = E_0 \sin(k_1 d_1)\sin[k_2(d_1 + d_2 - z)]$$

$$H_{y2}(z) = \frac{j}{Z_{TEM2}} E_0 \sin(k_1 d_1) \cos[k_2(d_1 + d_2 - z)], \quad \text{for } d_1 \le z \le d_1 + d_2, \quad \text{(A.2.2)}$$

with

$$Z_{TEM1} = \eta_1 = \sqrt{\frac{\mu_1}{\varepsilon_1}},$$

$$Z_{TEM2} = \eta_2 = \sqrt{\frac{\mu_2}{\varepsilon_2}},$$

$$k_1 = \omega\sqrt{\varepsilon_1 \mu_1} = k_0 n_1,$$

$$k_2 = -\omega\sqrt{\varepsilon_2 \mu_2} = k_0 n_2, \quad \text{(A.2.3)}$$

where subscripts 0, 1, and 2 refer to free space, DPS, and DNG, respectively. Z_{TEM1} and Z_{TEM2} are the impedances, k_0, k_1, and k_2 are the wave vectors, d_1 and d_2 are the thicknesses of the corresponding layers, ε_1 and ε_2 are permittivity, μ_1 and μ_2 are permeability, and n_1 and n_2 are refractive indices. Standard boundary conditions for the electromagnetic fields require that:

$$H_{y1}(z)\big|_{z=d_1} = H_{y2}(z)\big|_{z=d_1}. \quad \text{(A.2.4)}$$

Combining Eq. (A.2.4) with Eq. (A.2.1), (A.2.2) and (A.2.3), one obtains:

$$\frac{\mu_1}{k_1}\tan(k_1 d_1) + \frac{\mu_2}{k_2}\tan(k_2 d_2) = 0. \quad \text{(A.2.5)}$$

For a conventional resonator structure, the resonator size must be an integer multiple of $\lambda/2$, where λ is the wavelength in the material. Consequently, there is a minimum length requirement for resonance. In the DPS-DNG structure of Ref. 85, choices of d_1 and d_2 are independent of wavelength, as evident from Eq. (A.2.5), and

the total thickness of the cavity $d = d_1 + d_2$ can be much less than $\lambda / 2$ if parameters such as ε_2, μ_2, or n_2 are chosen appropriately.

Results of representative numerical calculations are shown in Fig. A.2.2. The DPS material is chosen to be polyethylene with $\varepsilon_1 = 2.25\varepsilon_0$ and $\mu_1 = \mu_0$. If we choose $f = 10\text{GHz}$ (free space wavelength $\lambda_0 = 3\text{cm}$), corresponding to $\lambda_1 = 2\text{cm}$,

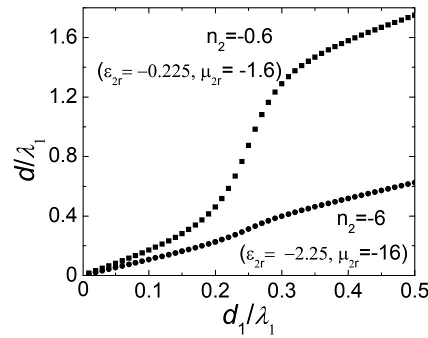

Fig. A.2.2 Total thickness *d* vs. DPS layer thickness d_1 for 1D DPS-DNG resonator structure. Large negative n_2 reduces system size.

then without employing a DNG material, the length of a resonator structure would be $d = \lambda_1 / 2 = 1\text{cm}$. However, with the inclusion of the DNG material, there is no restriction on the choice of d_1, and the total thickness $d = d_1 + d_2$ can be much less than $\lambda_1 / 2$. In general, the more negative n_2 is, the smaller the total thickness d is for a fixed d_1. For example, if we choose $d_1 = 0.20\lambda_1$, then we have $d = 0.46\lambda_1$ for $n_2 = -0.6$ while we have $d = 0.23\lambda_1$ for $n_2 = -6$.

In general, Eq. (A.2.5) must be solved numerically. Under certain conditions, however, Eq. (A.2.5) can be simplified. Under impedance matched conditions, i.e.,

$$Z_{TEM1} = \sqrt{\frac{\mu_1}{\varepsilon_1}} = \sqrt{\frac{\mu_2}{\varepsilon_2}} = Z_{TEM2}\,, \tag{A.2.6}$$

Eq. (A.2.5) becomes

$$\tan(k_1 d_1) + \tan(k_2 d_2) = 0\,, \tag{A.2.7}$$

and the fundamental solution is

$$k_2 d_2 = -k_1 d_1 \text{ or } \frac{d_2}{d_1} = -\frac{k_1}{k_2} = -\frac{n_1}{n_2}\,, \tag{A.2.8}$$

where n_1 and n_2 are the refractive indices for the DPS and DNG materials, respectively. Eq. (A.2.7) is called the phase compensation condition. The physical interpretation is self-evident: d_1 and d_2 must be such that any phase "delayed" inside the DPS region will be "gained back" inside the DNG region; the ratio of d_1 and d_2 is the inverse ratio of the wave vectors or refractive indices.

Another special situation is when the DPS material is one quarter wavelength long, i.e.

$$d_1 = \lambda_1 / 4 \text{ or } k_1 d_1 = \pi / 2\,. \tag{A.2.9}$$

From Eq. (A.2.5), we then obtain

$$d_2 = \lambda_2 / 4 \text{ or } k_2 d_2 = -\pi / 2\,. \tag{A.2.10}$$

As long as $n_2 > n_1$, the total thickness would be less than $\lambda_1 / 2$. In general, as is evident from Fig. A.2.2, we would like to have the DNG material possess a very large negative n_2 so that the total length of the resonator would be determined by the length of the DPS region, which can be considerably less than $\lambda_1 / 2$.

A.2.2 3-D DPS-DNG Cascaded Structure

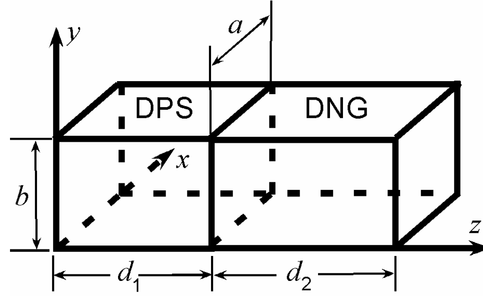

Fig. A.2.3 3-D cascaded DPS-DNG resonant cavity

In microwave circuits and systems, resonators can be constructed from structures such as rectangular cavities, which are basically closed sections of wave guide. Using ideas from the preceding section, we can miniaturize this cavity structure by including a NIM in its construction. For the 3-D cascaded resonant structure shown in Fig. A.2.3, for example, the existing fundamental mode is TE_{10m} (i.e., $k_x = \pi / a$, $k_y = 0$, and k_z to be determined). The EM field inside the resonator can be written as[86]

$$\begin{aligned} E_{y1}(x,z) &= E_0 \sin(k_{z2}d_2)\sin(\frac{\pi}{a}x)\sin(k_{z1}z) \\ H_{x1}(x,z) &= -\frac{j}{Z_{TEx1}} E_0 \sin(k_{z2}d_2)\sin(\frac{\pi}{a}x)\cos(k_{z1}z), \text{ for } 0 \le z \le d_1, \\ H_{z1}(x,z) &= \frac{j}{Z_{TEz1}} E_0 \sin(k_{z2}d_2)\cos(\frac{\pi}{a}x)\sin(k_{z1}z) \end{aligned} \tag{A.2.11}$$

$$\begin{aligned} E_{y2}(x,z) &= E_0 \sin(k_{z1}d_1)\sin(\frac{\pi}{a}x)\sin[k_{z2}(d_1+d_2-z)] \\ H_{x2}(x,z) &= \frac{j}{Z_{TEx2}} E_0 \sin(k_{z1}d_1)\sin(\frac{\pi}{a}x)\cos[k_{z2}(d_1+d_2-z)] \quad \text{, for } d_1 \le z \le d_1+d_2, \\ H_{z2}(x,z) &= -\frac{j}{Z_{TEz2}} E_0 \sin(k_{z1}d_1)\cos(\frac{\pi}{a}x)\sin[k_{z2}(d_1+d_2-z)] \end{aligned}$$

(A.2.12)

with

$$k_{z1} = \sqrt{k_1^2 - (\frac{\pi}{a})^2} = \sqrt{\omega^2 \varepsilon_1 \mu_1 - (\frac{\pi}{a})^2} \,,$$

$$k_{z2} = -\sqrt{k_2^2 - (\frac{\pi}{a})^2} = -\sqrt{\omega^2 \varepsilon_2 \mu_2 - (\frac{\pi}{a})^2} \,,$$

$$\eta_1 = \sqrt{\frac{\mu_1}{\varepsilon_1}} \,,\ Z_{TEx1} = \eta_1 \frac{k_1}{k_{z1}} \,,\ Z_{TEz1} = \eta_1 \frac{k_1}{\pi / a} \,,$$

$$\eta_2 = \sqrt{\frac{\mu_2}{\varepsilon_2}} \,,\ Z_{TEx2} = \eta_2 \frac{k_2}{k_{z2}} \,,\ Z_{TEz2} = -\eta_2 \frac{k_2}{\pi / a} \,, \tag{A.2.13}$$

where subscript 1 refers to the DPS material region and subscript 2 refers to the DNG region. a is the width and b is the height of the resonator structure; d_1 and d_2 are the the cavity lengths, and k_{z1} and k_{z2} are Z-component wave vectors in the DPS and DNG region, respectively. η_1 and η_2 are the impedances of the DPS and DNG materials for TEM waves, and Z_{TEx1} and Z_{TEx2} can be regarded as the impedances of the DPS and DNG materials for the x-component TE_{10} wave. Similarly, Z_{TEz1} and Z_{TEz2} can be regarded as the impedances of the DPS and DNG for the z-component TE_{10} wave.

Once again, the standard boundary conditions for the electromagnetic fields require that:

$$H_{x1}(x,z)\big|_{z=d_1} = H_{x2}(x,z)\big|_{z=d_1} \,. \tag{A.2.14}$$

Combining Eq. (A.2.14) with Eq. (A.2.11) to (A.2.13), we then obtain:

$$\frac{\mu_1}{k_{z1}}\tan(k_{z1}d_1)+\frac{\mu_2}{k_{z2}}\tan(k_{z2}d_2)=0\,. \qquad \text{(A.2.15)}$$

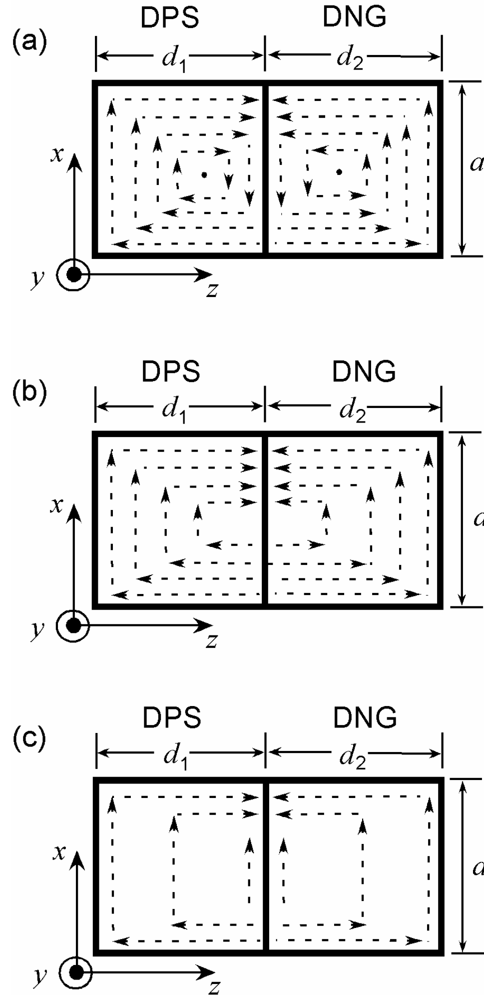

Fig. A.2.4 H-field distribution in x-z plane for 3D cascaded structure when (a) $k_{z1}d_1>\pi/2$; (b) $k_{z1}d_1=\pi/2$; (c) $k_{z1}d_1<\pi/2$.

As in the 1-D case, Eq. (A.2.15) imposes no requirement on d_1 or d_2; the cavity can therefore be made very short, as long as Eq. (A.2.15) is satisfied. Similarly, for the special situation in which

$$k_{z1}d_1=\pi/2\,, \qquad \text{(A.2.16)}$$

then we obtain

$$k_{z2}d_2 = 1/2\pi \text{ and } d_2/d_1 = -k_{z1}/k_{z2}. \qquad (A.2.17)$$

The H field distribution in the x-z plane is indicated in Fig. A.2.4 (a), (b) and (c) for $k_{z1}d_1 > \pi/2$, $k_{z1}d_1 = \pi/2$, and $k_{z1}d_1 < \pi/2$ respectively. The magnetic fields are coupled together in the DPS and DNG materials, forming a unified loop. At the boundary, the vertical fields are in the opposite direction while the parallel fields are in the same direction with the same magnitude. When condition Eq. (A.2.16) is met, the parallel fields at the boundary become zero.

A.2.3 3-D Partially Loaded Resonant Structure

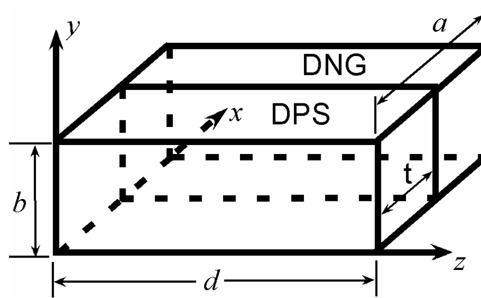

Fig. A.2.5 3-D partially-loaded DPS-DNG resonant cavity

In many cases of practical interest, such as impedance matching or phase-shifting sections, we have a partially filled waveguide. Assuming the filling material is composed of NIM, it is of interest to study its effect on the resonator dimensions shown in Fig. A.2.5. If we only consider the fundamental TE_{m01} mode (i.e., k_x is to be determined, $k_z = \pi/d$, and $k_y = 0$) inside this structure, the EM field can be expressed as:

$$E_{y1}(x,z) = E_0 \sin(k_{x1}x)\sin[k_{x2}(a-t)]\sin(\frac{\pi}{d}z)$$

$$H_{x1}(x,z) = -j\frac{E_0}{Z_{TEx1}}\sin(k_{x1}x)\sin[k_{x2}(a-t)]\cos(\frac{\pi}{d}z)$$

$$H_{z1}(x,z) = j\frac{E_0}{Z_{TEz1}}\cos(k_{x1}x)\sin[k_{x2}(a-t)]\sin(\frac{\pi}{d}z) \quad \text{for } 0 \le x \le t, \qquad \text{(A.2.18)}$$

$$E_{y2}(x,z) = E_0 \sin(k_{x1}t)\sin[k_{x2}(a-x)]\sin(\frac{\pi}{d}z)$$

$$H_{x2}(x,z) = j\frac{E_0}{Z_{TEx2}}\sin(k_{x1}t)\sin[k_{x2}(a-x)]\cos(\frac{\pi}{d}z)$$

$$H_{z2}(x,z) = -j\frac{E_0}{Z_{TEz2}}\sin(k_{x1}t)\cos[k_{x2}(a-x)]\sin(\frac{\pi}{d}z) \quad \text{for } t \le x \le a, \qquad \text{(A.2.19)}$$

where subscripts 1 and 2 refer to the DPS and DNG regions, respectively, t is the thickness of the DPS region, and $a-t$ is the thickness of the DNG region. k_{x1} and are the x-components of the wave vectors in the DPS and DNG materials, respectively, and are given by

$$k_{x1} = \sqrt{k_1^2 - k_{z1}^2} = \sqrt{\omega^2\varepsilon_1\mu_1 - (\pi/d)^2},$$

$$k_{x2} = -\sqrt{k_2^2 - k_{z2}^2} = -\sqrt{\omega^2\varepsilon_2\mu_2 - (\pi/d)^2},$$

$$\eta_1 = \sqrt{\frac{\mu_1}{\varepsilon_1}},\ Z_{TEz1} = \eta_1\frac{k_1}{k_{x1}},\ Z_{TEx1} = \eta_1\frac{k_1}{\pi/d},$$

$$\eta_2 = \sqrt{\frac{\mu_2}{\varepsilon_2}},\ Z_{TEz2} = \eta_2\frac{k_2}{k_{x2}},\ Z_{TEx2} = -\eta_2\frac{k_2}{\pi/d}, \qquad \text{(A.2.20)}$$

where k_{z1} and k_{z2} are the z-components of the wave vectors in the DPS and DNG materials, respectively.

We can see that the phase velocities in the DPS and DNG materials are the same by noting that $k_{z1} = k_{z2} = \pi / d$. Due to backwave propagation inside the NIM, energy actually flows in the opposite direction when the resonance is first excited. Once the standing waves form inside the cavity, energy flows back and forth in the z-direction while also exchanging between the DPS and DNG region. Standard boundary conditions require that

$$H_{z1}(x,z)\big|_{x=t} = H_{z2}(x,z)\big|_{x=t}, \tag{A.2.21}$$

which leads to the condition

$$\frac{\mu_1}{k_{x1}}\tan(k_{x1}t) + \frac{\mu_2}{k_{x2}}\tan[k_{x2}(a-t)] = 0, \tag{A.2.22}$$

which is similar to Eq. (A.2.5) and Eq. (A.2.15).

For this type of resonator, there is no limitation on width *t* or on *a-t* and the resonator can therefore be made very thin. Similarly, in the special case

$$k_{x1}t = \pi / 2, \tag{A.2.23}$$

then

$$k_{x1}t = 1/2\pi \text{ and } (a-t)/t = -k_{x1}/k_{x2}. \tag{A.2.24}$$

Similar to the situation illustrated in Fig. A.2.4, the *H* fields inside DPS and DNG are also incorporated together.

A.2.4 Mixed Double DPS-DNG 3-D Resonator

One of the implicit limitations on the 3-D cascaded resonator structure is that the width cannot be very small. Since $k_x = \pi / a < 2\pi / \lambda$, we have the width

requirement $a > \lambda/2$, where λ is the wavelength inside the DPS or DNG material.

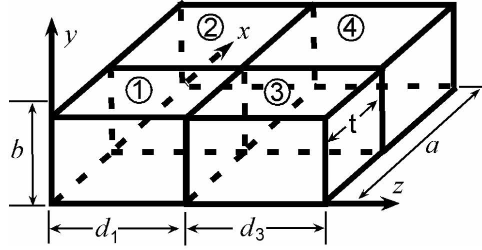

Fig. A.2.6 3-D mixed double DPS-DNG resonant cavity

Similarly, for the 3-D partially loaded structures, we have the length requirement $d > \lambda/2$. However, by combining the cascaded structure with the partially loaded structure, we can achieve resonators with both small length and small width at the same time, as indicated in Fig. A.2.6, in which materials 1 and 4 are DPS and material 2 and 3 are DNG. Similar to Eq. (A.2.15) and Eq. (A.2.22), from boundary condition requirements we obtain:

$$\frac{\mu_1}{k_{x1}}\tan(k_{x1}t)+\frac{\mu_2}{k_{x2}}\tan[(k_{x2}(a-t)]=0,$$

$$\frac{\mu_3}{k_{x3}}\tan(k_{x3}t)+\frac{\mu_4}{k_{x4}}\tan[(k_{x4}(a-t)]=0,$$

$$\frac{\mu_1}{\beta_1}\tan(k_{z1}d_1)+\frac{\mu_3}{\beta_3}\tan(k_{z3}d_3)=0,$$

$$\frac{\mu_2}{\beta_2}\tan(k_{z2}d_1)+\frac{\mu_4}{\beta_4}\tan(k_{z4}d_3)=0. \qquad \text{(A.2.25)}$$

The phase matching condition at $x = t$ then requires

$$k_{z1} = k_{z2},\ k_{z3} = k_{z4}, \qquad \text{(A.2.26)}$$

and the phase matching condition at $z = d_1$ requires

$$k_{x1} = k_{x3},\ k_{x4} = k_{x2}. \qquad \text{(A.2.27)}$$

Furthermore, the wave vector k_i must satisfy

$$k_{xi}^2 + k_{zi}^2 = k_i^2 = \omega^2 \mu_i \varepsilon_i, \qquad i = 1,2,3,4. \tag{A.2.28}$$

Combining Eq. (A.2.28) with Eq. (A.2.25) to Eq. (A.2.27), we can then obtain the material requirements as:

$$\frac{\mu_1}{\mu_2} = \frac{\mu_3}{\mu_4}, \tag{A.2.29}$$

$$\mu_1\varepsilon_1 - \mu_2\varepsilon_2 = \mu_3\varepsilon_3 - \mu_4\varepsilon_4. \tag{A.2.30}$$

The choices of DPS and DNG materials for such a resonator structure must satisfy Eq. (A.2.29) and Eq. (A.2.30). The resonator geometry can then be determined numerically from Eq. (A.2.25) to (A.2.27) as a function of resonant frequency. For example, suppose we assume the following values:

$\varepsilon_1 = \varepsilon_4 = 2.25\varepsilon_0$, $\mu_1 = \mu_4 = \mu_0$ (polyethylene), $\varepsilon_2 = -1.5\varepsilon_0$, $\mu_2 = -1.5\mu_0$, $\varepsilon_3 = -3.38\varepsilon_0$, $\mu_3 = -0.667\mu_0$ at $f = 10\text{GHz}$. If we assume $d_1 = 0.1\lambda_1$, $t = 0.1\lambda_1$ and $k_{x1} = 0.5k_1$ (k_1 is the wave vector in the DPS material), we then have $d_3 = 0.14\lambda_1$ and $a - t = 0.07\lambda_1$, and the overall dimensions are: length $d = d_1 + d_3 = 0.24\lambda_1$ and width $a = 0.17\lambda_1$, both much smaller than for a conventional cavity resonator and lead to a reduction in total resonator volume in the example by approximately a factor of 6.

A.2.5 Summary—Resonator Analysis

In summary, the possibility of applying NIM in DPS-DNG cavity resonators has been discussed and analyzed in different geometrical forms. For DPS-DNG resonator structures, the cavity dimension is largely independent of the wavelength. To

reduce the system size, the magnitude of the refractive index of the DNG should be much larger than that of the DPS. These results show that NIM materials offer very intriguing possibilities for very substantially reducing microwave resonator volumes. However, the quality factor Q of the resonators, after including NIM, remains to be investigated.

A.3 Negative Index Material Design, Fabrication and Characterization

A.3.1 Design of Single Split Ring With Overlapping Arms Structure

As mentioned in the introduction, the composite metamaterial fabricated by Smith et al. is anisotropic and requires careful alignment with the polarization of the incident EM field, which impedes its application and presents a great challenge to its mass production. Therefore, an isotropic NIM structure with easy fabrication method is much desired.

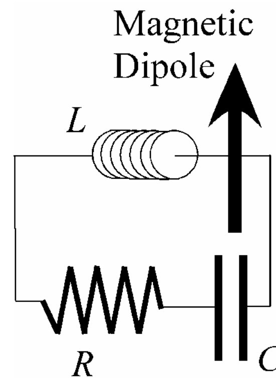

Fig. A.3.1 Equivalent *LCR* resonant circuit for split ring

In Pendry and Smith's structure, the negative μ comes from the resonance of two split rings (SR). At resonance, these two rings represent an equivalent *LCR* resonant circuit,[87] forming a strong magnetic dipole, as shown in Fig. A.3.1. When the

dipole response can no longer follow the variation of the EM field and is out of phase, an effective negative μ would be generated in space.

Based on this concept, we have designed a single split ring with overlapping arms (SSROA), as shown in Fig. A.3.2, which also forms an equivalent resonant *LCR* circuit. Capacitance *C* comes from the two overlapping arms, inductance *L* comes from the nearly-enclosed ring and resistance *R* comes from the resistance of the metal. The value of *L*, *C* and *R* can be roughly estimated from the geometry of the structure as follows:

$$L = \mu_0 \frac{A}{h} = \mu_0 \frac{(b-2a)(b-3a-d)}{h}, \quad \text{(A.3.1)}$$

$$C = \varepsilon_0 \frac{S}{d} = \varepsilon_0 \frac{bh}{d}, \quad \text{(A.3.2)}$$

$$R = \rho \frac{l}{s} = \rho \frac{3b}{ah}, \quad \text{(A.3.3)}$$

where μ_0 is the vacuum permeability, *A* is the area enclosed by the ring, *b* is the arm

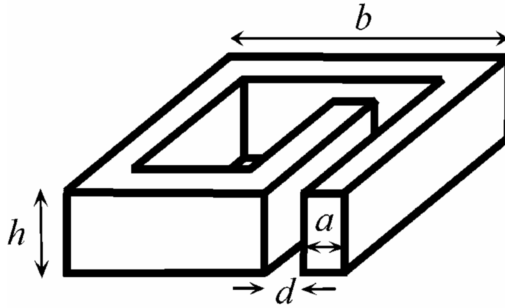

Fig. A.3.2 Structure of single split ring with overlapped arms (SSROA)

length, *a* is the arm thickness, *d* is the arm spacing, and *h* is the arm height; ε_0 is the vacuum permittivity, *S* is the facing area of the two overlapping arms; ρ is the

resistivity of the metal, l is the total length of the arm and s is the cross-sectional area of the arm.

In the following analysis, for simplicity, we assume the SSROA structures are fabricated on one single planar surface in periodic arrays, as shown in Fig. A.3.3, then, following the derivation described in Ref. 87, when the incident magnetic field is perpendicular to the surface, we can calculated the effective permeability in space as follows:

$$\mu = \mu_0 \left(1 - \frac{Ff^2}{f^2 - f_0^2 - jf\gamma_m} \right), \tag{A.3.4}$$

where

$$F = \mu_0 \frac{A^2}{L \cdot V}, \tag{A.3.4a}$$

$$f_0 = \frac{1}{2\pi\sqrt{LC}}, \tag{A.3.4b}$$

$$\gamma_m = \frac{R}{2\pi L}, \tag{A.3.4c}$$

with V being the space occupied by one unit cell. For a planar array structure, V is given as:

$$V = L_a^2 \cdot h, \tag{A.3.4d}$$

where L_a is the unit cell lattice constant.

In the metamaterial constructed by Smith et al., negative ε is due to the plasmon response from the metal thin wires. Because the conduction electrons are constrained and confined in the thin metal wires, the plasmon resonant frequency is reduced from optical to microwave frequencies. The effective ε is given as:[88,89]

$$\varepsilon = \varepsilon_0\left(1 - \frac{f_p^2}{f(f + j\gamma_e)}\right), \qquad \text{(A.3.5)}$$

where

$$f_p = \frac{1}{2\pi}\sqrt{\frac{n_{eff}}{n s_w L_w \varepsilon_0}}, \qquad \text{(A.3.5a)}$$

$$\gamma_e = \frac{\rho}{2\pi s_w L_w}, \qquad \text{(A.3.5b)}$$

with n being the electron density in the metal, n_{eff} being the effective electron density, s_w being the cross-sectional area of the wire for electron conduction, and L_w being the inductance of the wire due to electron movement.

For the ring structure arrays shown in Fig. A.3.3, each arm can be regarded as a segment of thin wires. However, it restricts the movement of electrons in different ways depending on the direction of the electron movement. Therefore, the effective electrical permittivity ε is a function of the electric field polarization. When the electric field is parallel to the planar surface and the arms, electrons are excited to move along the arms and the parameters in Eq. (A.3.5) can be approximated as follows:

$$n_{eff} = \frac{2ab}{L_a^2} n, \qquad \text{(A.3.6a)}$$

$$s_w = 2ah, \qquad \text{(A.3.6b)}$$

$$L_w = \frac{\mu_0}{2\pi}\ln\left(\frac{L_a}{\sqrt{s_w / \pi}}\right). \qquad \text{(A.3.6c)}$$

When the electric field is perpendicular to the surface and when the ring structure is thick (but still $h << \lambda$), electrons would be excited to move vertically inside the metal rings and we would expect the existence of some plamon resonance with the parameters in Eq. (A.3.5) being estimated as:

$$n_{eff} = \frac{5(b-a)a}{L_a^2} n , \tag{A.3.7a}$$

$$s_w = 5(b-a)a , \tag{A.3.7b}$$

$$L_w = \frac{\mu_0}{2\pi} \ln\left(\frac{L_a}{\sqrt{s_w / \pi}} \right). \tag{A.3.7c}$$

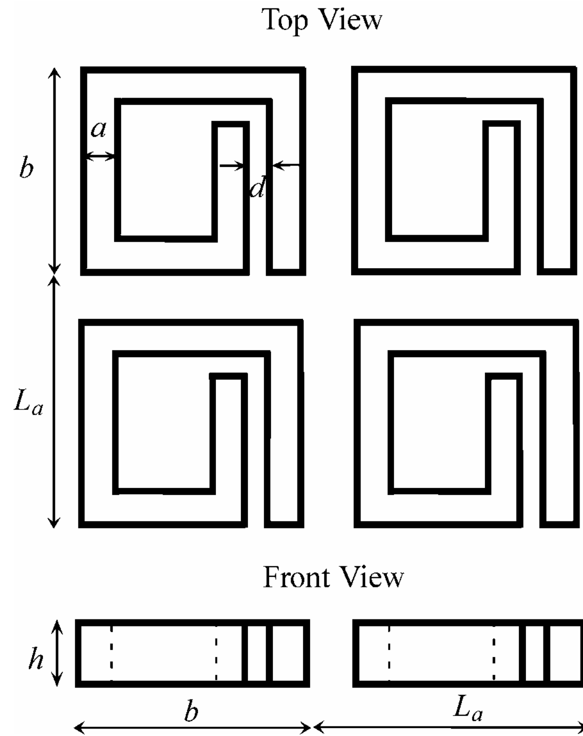

Fig. A.3.3 Top view and front view of the SSROM arrays on planar structure

We should note that the above equations (A.3.1) to (A.3.7) can only provide a picture of the relevant physics and qualitative approximations, and precise results can only be obtained from full scale numerical simulations tools such as High-Frequency Structure Simulator (HFSS).

When geometrical parameters are carefully chosen, it is very possible that negative ε and negative μ could be generated simultaneously, saving us the space and trouble to include thin wires in the unit cell. This SSROA structure is still anisotropic, but since periodicity is not required for NIM,[90,91] by randomly distributing this SSROA structure in space with different orientations, we can therefore achieve an isotropic response to the incident EM field. As opposed to the double split ring (DSR) structure, which requires the alignment of the two rings within one unit cell, thick single split ring structures with overlapping arms (SSROA) only involve one ring to generate the desired electrical and magnetic responses and therefore it is much easier to randomly distribute them in the space.

A.3.2 Electroplating Fabrication

The basic goal is to fabricate the randomly distributed SSROA structures in space. But first, we would like to fabricate them in arrays on the planar structure to characterize its electrical and magnetic response. To generate a strong magnetic response and a strong electrical response from the SSROA structure, thick metal arms are desired. Traditional photolithography and E-beam deposition or sputtering processes cannot satisfy this requirement, especially for mass production. Electroplating has been tried in this research and has achieved some quite good results.

First, a thin metal seed layer was sputtered on a glass substrate using a Denton Discovery 18 Sputtering system. The seed layer consists of 20 nm Ti for good adhesion with glass and 30 nm Au for protection from oxidation. Then a layer of photoresist SU-8 25 was spun on at 1000 rpm, which leads to a thickness of about 40 µm. After prebaking at 65 ºC for 5 minutes and soft bake at 95 ºC for 15 minutes, the masked sample was exposed with 320 nm UV for 50 seconds. Post baking was set at 65 ºC for 1 minute and 95 ºC for 4 minutes. After photoresist development, we then performed the electroplating in a Kissler electroplating machine. Two metals were tried--Ni and Au, and both turned out to be successful. The Ni bath is commercially available from Technic Inc., and it is a mixture of nickel sulfamate and nickel bromide. The bath temperature T was set at 52 ºC, pH was set at 4.8, tank level at 55%, flow rate at 12 L/min, and deposition current I set at 200mA to achieve a balance between the deposition speed and the deposition quality. The deposition continued for about 8 minutes for each sample set. Au bath is also commercially available from Technic Inc.deposition with product code TG-25E RTU. The bath temperature T was set at 60 ºC (140 ºF) , pH was set at around 6.5, tank level at 50%, and flow rate at 10 L/min. The deposition current density I is about 20 mA and deposition time t is about 180 minutes. After the deposition, Remover PG was used to lift off the photoresist and O_2 plasma etching was also used to remove any residue photoresist if necessary. Then a quick dip about 5 to 10 seconds in Au etchant (10g KI, 2.5 g I_2 and 100 ml DI water) and a quick dip about 10 to 20 seconds in Ti etchant (50 parts of DI water, 1 part of HNO_3 and 1 part of HF) was performed to remove the seed layer. The finished Ni pattern has a thickness h of about 20 µm on the glass substrate and the finished Au

pattern has a thickness h of about 10 μm. The conditions and results are summarized in Table A.3.1. Thickness measurement is performed using Sloan Dektak 3030ST.

The deposition current density used for Au is much smaller than that used for Ni, because Au has a much stronger tendency to precipitate. Au can even grow on the photoresist if the sample is biased such that a certain threshold electric field exists on the surface of the photoresist layer.

Deposition time t can be calculated according to the charge transfer relationship:

$$Ni^{++} + 2e^{-} \leftrightarrow Ni \,, \qquad \text{(A.3.8a)}$$

$$Au^{+} + e^{-} \leftrightarrow Au \,, \qquad \text{(A.3.8b)}$$

and is given explicitly by:

$$t = \frac{\rho S h}{A_w} \times N_A \times V_A \times \frac{e}{I} \,, \qquad \text{(A.3.9)}$$

where ρ is the metal density in g/cm^3, S is the area exposed during electroplating in cm^2, h is the targeted thickness in cm, A_w is the atomic weight in g/mol, N_A is the Avogadro constant 6.02×10^{23}, V_A is the valence number, e is electron charge unit $1.602 \times 10^{-19}\,\mathrm{C}$, and I is the deposition current density in A. Eq. (A.3.11) turns out to be quite accurate, meaning the competitive reactions showing below at the electrodes have been greatly suppressed:

$$2H^{+} + 2e^{-} \leftrightarrow H_2 \uparrow \,, \qquad \text{(A.3.10a)}$$

$$4OH^{-} - 4e^{-} \leftrightarrow 2H_2O + O_2 \uparrow \,. \qquad \text{(A.3.10b)}$$

For example, for metal Ni, $\rho = 8.9\text{g/cm}^3$, $A_w = 58.7\text{g/mol}$, $V_N = 2$, $I = 200\text{mA} = 0.2\text{A}$, and $S \approx 1.5\text{cm}^2$. Then for a thickness of 20 µm, the deposition time needed, according to Eq. (A.3.11), is t=7.3 min. For Au, $\rho = 19.3\text{g/cm}^3$, $A_w = 197.2\text{g/mol}$, $V_N = 1$, and $I = 20\text{mA} = 0.02\text{A}$. Due to the equipment setup restriction, the exposed area is about 2 inches in diameter (D=2 inches) and so $S \approx \pi \times (D/2)^2 \approx 20.27\text{cm}^2$. Then the required deposition time to achieve h=10 µm is t=160min. The calculations agree quite well with results from Table A.3.1, considering the area and the thickness measurement uncertainties.

Table A.3.1 Electroplating conditions and measured results

Metal (Bath)	T (ºC)	pH	Flow Rate (L /min)	Tank Level	S (cm^2)	I (mA)	Dep. Density (ASF)[1]	t (min)	h (µm)	Dep. Rate (µm /min)
Ni (Nickel Sulfamate , Nickel Bromide)	52	4.8	12	55%	1.2-1.6	200	~120	8	~20	2.5
Au (TG-25E RTU[2])	60	6.5	10	50%	~20[3]	20	~1	180	~10	0.056

The fabricated patterns are shown in Fig. A.3.4a and Fig. A.3.4b for Au and Ni, respectively, and the parameters in the figures are as follows:

$a = 60\mu\text{m}$, $b = 360\mu\text{m}$, $d = 20\mu\text{m}$, $h = 10\mu\text{m}$, $L_a = 600\mu\text{m}$ for Fig. A.3.4a with Au;

$a = 30\mu\text{m}$, $b = 180\mu\text{m}$, $d = 10\mu\text{m}$, $h = 20\mu\text{m}$, $L_a = 250\mu\text{m}$ for Fig. A.3.4b with Ni.

[1] Ampere per Square Foot, a unit commonly used in electroplating industry
[2] Please visit the website of Technic Inc. for more detailed information: www.technic.com
[3] Restricted by sample holder size (2 inch diameter metal holder)

And the expected resonance occurs at 0.2 THz and 0.1 THz, respectively for parameters chosen above.

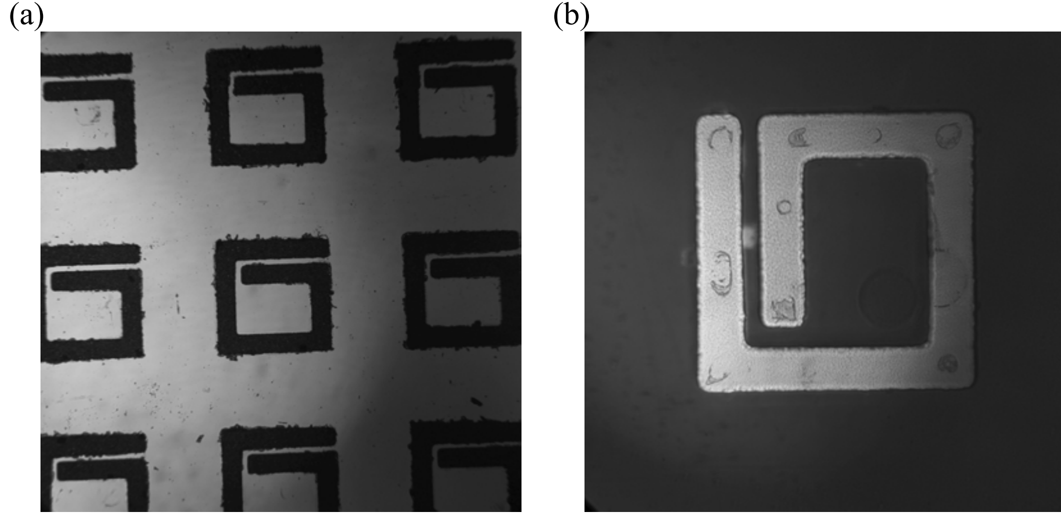

Fig. A.3.4a Electroplated Au (magnification: 10X), with a=60 μm, b=360 μm, d=20 μm, h= 10 μm, and L_a=600 μm; A.3.4b electroplated Ni (magnification: 50X) with a=30 μm, b=180 μm, d=10 μm, h= 10 μm, and L_a=250 μm.

Because of the thick photoresist (~40 μm) and the UV light (320nm) we used, there is a fundamental diffraction limit as regarding to the minimum geometry D (in this particular case, it refers to arm spacing d) that can be achieved in this photolithographic process, as indicted from Fig. A.3.5:

Since

$$\Delta x = 0.61 \frac{\lambda}{D} h \,, \tag{A.3.11}$$

the diffraction limit is reached when

$$\Delta x = D / 2 \,. \tag{A.3.12}$$

Combining Eq. (A.3.11) with Eq. (A.3.12), we calculate that the minimum D allowed for this process is:

$$D = \sqrt{1.22\lambda h} = 4\mu m\,. \tag{A.3.13}$$

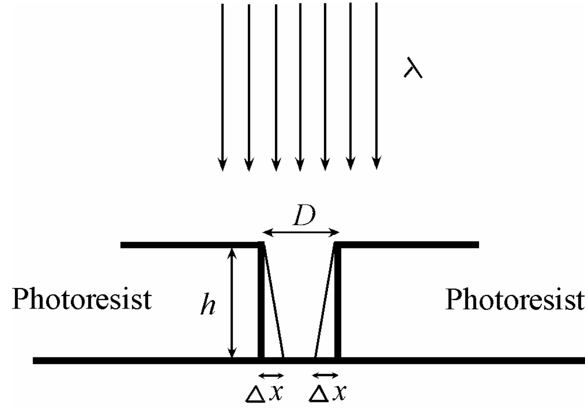

Fig. A.3.5 The fundamental limit on D is when Δx=D/2

A.3.3 Possible Characterization Method

We suggest characterization of the electromagnetic response of this thick planar SSROA arrays using spectroscopic ellipsometry, which has been applied before by Yen et. al. to detect the THz magnetic response of the 3 μm thick planar SSR[82] arrays fabricated on the quartz substrate using photo proliferated process (PPP)[92].

The measurement is based on the different reflections of s-wave and p-wave by the planar structure, as indicated in Fig. A.3.6.

The reflection and refraction of s-wave and p-wave can be calculated as following:

$$r^s = \frac{\frac{1}{\eta_i}\cos\theta_i - \frac{1}{\eta_t^s}\cos\theta_t^s}{\frac{1}{\eta_i}\cos\theta_i + \frac{1}{\eta_t^s}\cos\theta_t^s}, \qquad t^s = \frac{\frac{2}{\eta_i}\cos\theta_i}{\frac{1}{\eta_i}\cos\theta_i + \frac{1}{\eta_t^s}\cos\theta_t^s},$$

$$r^p = \frac{\eta_i \cos\theta_i - \eta_t^p \cos\theta_t^p}{\eta_i \cos\theta_i + \eta_t^p \cos\theta_t^p}, \quad t^p = \frac{2\eta_t^p \cos\theta_i}{\eta_i \cos\theta_i + \eta_t^p \cos\theta_t^p}, \tag{A.3.14}$$

where

$$\eta_i = \sqrt{\mu_i / \varepsilon_i}\ , \tag{A.3.14a}$$

$$\eta_t^s = \sqrt{\mu_t^s / \varepsilon_t^s}\ , \tag{A.3.14b}$$

$$\eta_t^p = \sqrt{\mu_t^p / \varepsilon_t^p}\ , \tag{A.3.14c}$$

subscript i represents incident medium, and t represents transmitted medium. Superscript s represents s-wave, and p represents p-wave. η_i is the impedance in the incident medium, and θ_i is the incident angle with respect to the incident normal. η_t^s and η_t^p are the impedances in the transmitted medium for s-wave and p-wave, respectively. θ_t^s and θ_t^p are the refracted angles for s-wave and p-wave, respectively.

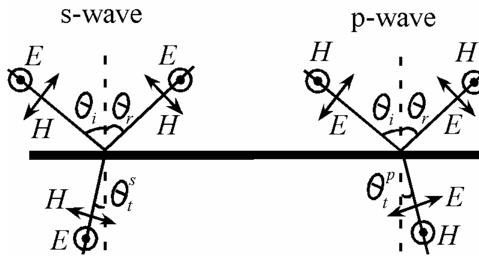

Fig. A.3.6 Reflection of s-wave and p-wave by planar structure

Normally, in the isotropic material, η_t^s and η_t^p are the same, so are θ_t^s and θ_t^p. However, the planar SSROA array is anisotropic and it has a strong magnetic response only to the incident s-wave, when there exists a perpendicular H field component. Beside, the electrical responses of planar SSROA structure are also different to s-wave and p-wave, according to Eq. (A.3.6) and Eq. (A.3.7), when the parallel and vertical

components of the E-field vary with s and p polarization. So, the refracted s-wave and p-wave will experience different electric permittivity ε_t^s , ε_t^p 's and magnetic permeability μ_t^s, μ_t^p's, depending on the refracted angle θ_t, which is determined by Snell's law. If the material response can be decomposed into vertical responses $\mu_\perp$, $\varepsilon_\perp$ and the parallel responses $\mu_{//}$, $\varepsilon_{//}$, in reference to the reflection surface, then similar to the index-ellipsoid construction,[93] we can express the effective ε_t and effective μ_t in the following way:

For s-wave, the transmitted electric field experiences only $\varepsilon_{t//}$, while magnetic field experiences both $\mu_{t//}$ and $\mu_{t\perp}$, and the effective μ_t is given by:

$$\frac{1}{\mu_t(\theta_t)} = \frac{\cos^2\theta_t}{\mu_{t//}} + \frac{\sin^2\theta_t}{\mu_{t\perp}}. \tag{A.3.15}$$

For p-wave, the transmitted magnetic field experiences only $\mu_{t//}$, while electric field experiences both $\varepsilon_{t//}$ and $\varepsilon_{t\perp}$, and the effective ε_t is given by:

$$\frac{1}{\varepsilon_t(\theta_t)} = \frac{\cos^2\theta_t}{\varepsilon_{t//}} + \frac{\sin^2\theta_t}{\varepsilon_{t\perp}}. \tag{A.3.16}$$

Combining with Snell's law (choosing the negative sign in the equation when both $\mu_t(\theta_t)$ and $\varepsilon_t(\theta_t)$ are negative),

$$\pm\sqrt{\mu_t(\theta_t)\varepsilon_t(\theta_t)}\sin\theta_t = \sqrt{\mu_1\varepsilon_1}\sin\theta_1, \tag{A.3.17}$$

we can calculate the refracted angle θ_t for s-wave and p-wave, respectively:

$$\theta_t^s = \pm\tan^{-1}\left(\sqrt{\frac{\mu_{t\perp}}{\mu_{t\perp}\mu_{t//}\varepsilon_{t//}/\left(\mu_i\varepsilon_i\sin^2\theta_i\right) - \mu_{t//}}}\right), \tag{A.3.18}$$

$$\theta_t^p = \pm \tan^{-1}\left(\sqrt{\frac{\varepsilon_{t\perp}}{\varepsilon_{t\perp}\varepsilon_{t//}\mu_{t//}/\left(\mu_i\varepsilon_i \sin^2\theta_i\right) - \varepsilon_{t//}}}\right). \quad \text{(A.3.19)}$$

The signs in these two equations should be chosen such that Eq. (A.3.17) is satisfied. The values for $\mu_{t\perp}$ can be obtained from Eq. (A.3.4), the value for $\varepsilon_{t//}$ can be obtained from Eq. (A.3.5) and Eq. (A.3.6), and the value for $\varepsilon_{t\perp}$ can be obtained from Eq. (A.3.5) and Eq. (A.3.7) once we know all the geometrical parameters. $\mu_{t//}$ can be generally regarded as being μ_0 since the magnetic response is trivial under this condition. Once θ_t^s and θ_t^p can be calculated from Eq. (A.3.18) and Eq. (A.3.19), the reflection coefficient r^s and r^p can be derived according to Eq. (A.3.14).

In the spectroscopic ellipsometry measurement, the SSROA structure, about 10~20 μm thick, can be regarded as an anisotropic thin film and multi-reflections are expected to occur at the different boundaries, as shown schematically in Fig A.3.7. The first layer is air, denoted by 1 with infinite thickness; second layer is this SSROA-formed thin film, denoted by 2 with thickness about 10~20 μm; third layer is glass substrate, denoted by 3 with thickness about 5 *mm*; fourth and last layer is still air, denoted by 4 with infinite thickness. Multiple reflections can be calculated according to the following:[94]

$$r_{1234} = r_{123} + \frac{t_{123} r_{31} t_{321} e^{2j\delta_3}}{1 - r_{321} r_{31} e^{2j\delta_3}}, \quad \text{(A.3.20)}$$

$$t_{1234} = \frac{t_{123} t_{31} e^{j\delta_3}}{1 - r_{321} r_{31} e^{2j\delta_3}}, \quad \text{(A.3.21)}$$

with

$$r_{123} = r_{12} + \frac{t_{12} r_{23} t_{21} e^{2j\delta_2}}{1 - r_{21} r_{23} e^{2j\delta_2}}, \tag{A.3.22}$$

$$t_{123} = \frac{t_{12} t_{23} e^{j\delta_2}}{1 - r_{21} r_{23} e^{j\delta_2}}, \tag{A.3.23}$$

$$\delta_2 = \frac{2\pi n_2 d_2 \cos(\theta_2)}{\lambda_0}, \tag{A.3.24}$$

$$\delta_3 = \frac{2\pi n_3 d_3 \cos(\theta_3)}{\lambda_0}. \tag{A.3.25}$$

r_{ij} and t_{ij} refer to single reflection and single transmission at interface between medium i and j, and can be calculated according to Eq. (A.3.14) for s-wave and p-wave, respectively. θ_2 θ_3 are the refractive angles inside medium 2 and medium 3, respectively and they are different for s-wave and p-wave, according to Eq. (A.3.18) and Eq. (A.3.19). δ_2 and δ_3 are the phase variations inside medium 2 and medium 3, respectively. Again, different values should be applied for s-wave and p-wave.

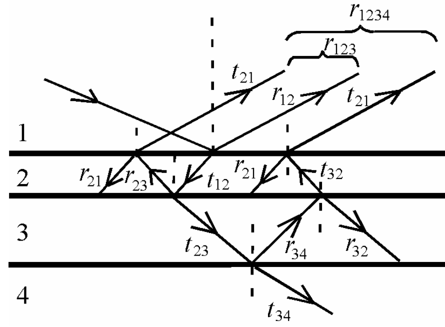

Fig. A.3.7 Schematic plot of multireflection at each interfaces

Total reflected power will then be calculated as:

$$R_{1234} = \left| r_{1234}^2 \right|. \tag{A.3.26}$$

By measuring the difference in the reflected power by s-wave and p-wave, the electromagnetic response from the SSROA structure can be inferred.

Now, once the electromagnetic properties of this SSROA can be determined and well characterized, we can mass-fabricate it on a soluble substrate, such as organic polymer or SiO_2, using electroplating method. Then after the deposition, this substrate can be removed, leaving tiny structures standing alone. By mixing them with adequate supporting materials, we can apply them as paint or spray onto the surfaces we are interested in, and the random distribution and different orientation of SSROA structures can give an isotropic property desired in situations such as near-field amplification, impedance matching and coupling. We can also mix the structures with different sizes together, achieving a broad band response. The averaged response from these structures would be smaller than the averaged response from single-size structure in periodic arrays. The behavior of the mixture can also be characterized using spectroscopic ellipsometry by looking at either the transmission or reflection properties. As said by N. Engheta et al.,[95] the future of NIM will be positive.

A.4 Conclusion

In summary, we have discussed the possible application of NIM in resonators and its effect on resonator Q. The inclusion of NIM can reduce the size of the resonant cavities. We also concluded that the stored energy inside NIM appears to have the opposite properties as opposed to the energy inside DPS. At resonance, the total electrical energy balances the total magnetic energy in the system, but within each material, the net reactive energy is not zero. The cancellation of the reactive energy

reduces the quality factor, but this reduction can be minimized if the structural and material properties are carefully chosen. We have also designed a SSROA structure with the benefits of easy fabrication and the potential of achieving isotropic properties. Some preliminary fabrication results are presented with the discussion of possible characterization method.

References

[1] G. Parish, S. Keller, P. Kozodoy, J. P. Ibbetson, H. Marchand, P. T. Fini, S. B. Fleischer, S. P. DenBaars, U. K. Michra, and E. J. Tarsa, Appl. Phys. Lett. **75**, 247 (1999)

[2] U. V. Bhapkar and M. S. Shur, J. Appl. Phys. 82, 1649 (1997); D. Walker, V. Kumar, K. Mi, P. Sandvik, P. Kung, X. H. Zhang, and M. Razeghi, Appl. Phys. Lett. **76**, 403 (2000)

[3] Q. Chen, M. Asif Khan, J. W. Yang, C. J. Sun, M. S. Shur, and J. Appl. Phys. **82**, 1649 (1997)

[4] L. S. McCarthy, P. Kozodoy, M. J. W. Rodwell, S. P. DenBaars, and U. K. Mishra, IEEE Electron Device Lett. **35**, 277 (1997)

[5] S. Yoshida and J. Suzuki, Jpn. J. Appl. Phys., Part 2 **38**, L851 (1999)

[6] J. Wu, W. Walukiewicz, K. M. Yu, J. W. Ager III, E. E. Haller, H. Lu, W. J. Schaff, Y. Saito, and Y. Nanishi, Appl. Phys. Lett. **80**, 3967 (2002)

[7] O. Ambacher, J. Majewski, C. Miskys, A. Link, M. Hermann, M. Eickhoff, M. Stutzmann, F. Bernardini, V. Fiorentini, V. Tilak, B. Schaff, and L. F. Eastman, J. Phys.: Condens. Matter **14**, 3399 (2002)

[8] S. C. Jain, M. Willander, J. Narayan, and R. Van Overstraceten, J. Appl. Phys. **81**, 726 (1997)

[9] J. Kolnik, I. H. Oguzman, K. F. Brennan, Wang Rongping, and P. P. Ruden, J. Appl. Phys. **81**, 726 (1997)

[10] Y. F. Wu, D. Kapolnek, J. P. Ibbetson, P. Parikh, B. Keller and U. K. Mishra, IEEE Trans. Electron. Dev. **48**, 586-590 (2001)

[11] V. Tilak, B. Green, V. Kaper, H. Kim, T. Prunty, J. Smart, J. Shealy, and L. Eastman, IEEE Electron. Dev. **22**, 504 (2001)

[12] S. Tomiya, E. Morita, M. Ukita, H. Okuyama, S. Itoh, K. Nakano, and A. Ishibashi, Appl. Phys. Lett. **66**, 1208 (1995)

[13] M. J. Manfra, presented at 2000 Fall Mater. Res. Soc. Meeting, 17 November-1 December, Boston, MA

[14] C. R. Elsass, C. Poblenz, B. Heying, P. Fini, P. M. Petroff, S. P. DenBaars, U. K. Mishra, and J. S. Speck, J. Crystal Growth **233**, 709 (2001)

---

[15] J. W. P. Hsu, M. J. Manfra, S. N. G. Chu, C. H. Chen, L. N. Pfeiffer, and R. J. Molnar, Appl. Phyus. Lett. **78**, 3980 (2001)

[16] V. G. Veselago, Sov. Phys.—Usp. **47**, 509 (1968)

[17] J. B. Pendry, A. J. Holden, D. J. Robbins, and W. J. Stewart, “Magnetism from conductors and enhanced nonlinear phenomena,” IEEE Trans. Microw. Theory Tech. vol. **47**, no. 11, pp. 2075—2081, Nov. 1999

[18] D. R. Smith, W. J. Padilla, D. C. Vier, S. C. Nemat-Nesser, and S. Schultz, “Composite medium with simultaneously negative permeability and permittivity,” Phys. Rev. Lett., vol. **84**, pp. 4184—4187, May 2000

[19] Y. Horii, C. Caloz, and T. Itoh, “Super-Compact Multilayered Left-Handed Transmission Line and Diplexer Application,” IEEE Trans. Microw. Theory and Tech., vol. **53**, no. 4, pp. 1527—1534, Apr. 2005

[20] C. Caloz and T. Itoh, “Transmission Line Approach of Left-Handed (LH) Materials and Microstrip Implementation of an Artificial LH Transmission Line,” ITTT Tans. Antennas Propagat., vol. **52**, no. 5, pp. 1159—1166, May 2004

[21] R. W. Ziolkowski, and A. D. Kipple, “Application of Double Negative Materials to Increase the Power Radiated by Electrically Small Antennas,” IEEE Trans. Antennas Propagat., vol. **51**, no. 10, pp. 2626—2640, Oct. 2003

[22] S. Lim, C. Caloz and T. Itoh, “Metamaterial-Based Electronically Controlled Transmission-Line Structure as a Novel Leaky-Wave Antenna With Tunable Radiation Angle and Beamwidth,” IEEE Trans. Microw. Theory Tech., vol. **52**, no. 12, pp. 2678—2690, Dec. 2004

[23] S. N.Mohammad, and H. Morkoc, J. Appl. Phys., **78**, 4200 (1995).

[24] T. Makimoto, K. Kumakura, and N. Kobayashi, Appl. Phys. Lett., **83**, 1035 (2003).

[25] S. Nakamura, G. Fasol, *The Blue Laser Diode*, Springer, Berlin, 1997.

[26] E. T. Yu, "Spontaneous and piezoelectric polarization effects in nitride heterostructures," in *III-V Nitride Semiconductors: Applications and Devices*, E. T. Yu and O. Manasreh, eds. (Taylor & Francis, 2003), pp. 161-191.

[27] E. J. Miller, E. T. Yu, C. Poblenz, C. Elsass, and J. S. Speck, *Appl. Phys. Lett.* **80**, 3551 (2002).

[28] D. Schroder, *Semiconductor Material and Device Characterization*, 2nd ed. (Wiley, Toronto, 1998).

[29] H. Kroemer, Wu-Yi Chien, J. S. Harris, and D. D. Edwall, Appl. Phys. Lett., **36**, 295 (1980).

[30] C. Poblenz, T. Mates, M. Craven, S. P. DenBaars, and J. S. Speck, Appl. Phys. Lett. **81**, 2767 (2002).

[31] M. J. Murphy, B. E. Foutz, K. Chu, H. Wu, W. Yeo, W. J. Schaff, O. Ambacher, L. F. Eastman, T. J. Eustis, R. Dimitrov, M. Stutzmann, and W. Rieger, MRS Internet J. Nitride Semicond. Res. 4S1, G8.4 (1999)

[32] O. Ambacher, J. Smart, J. R. Shealy, N. G. Weimann, K. Chu, M. Murphy, W. J. Schaff, L. F. Eastman, R. Dimitrov, L. Wittmer, M. Stutzmann, W. Rieger and J. Hilsenbeck, J. Appl. Phys. **85**, 3222 (1999)

[33] F. Sacconi, A. D. Carlo, P. Lugli and H. Morkoc, IEEE Trans. Electron. Dev. **48**, 450 (2001)

[34] M. Ershov, H. C. Liu, L. Li, M. Buchanan, Z. R. Wasilewski, and A. K. Jonscher, IEEE Trans. Electron Devices, **45**, 2196 (1998).

[35] E. J. Miller, D. M. Schaadt, E. T. Yu, C. Poblenz, C. Elsass, and J. S. Speck, J. Appl. Phys., **91**, 9821 (2002).

[36] E. J. Miller, D. M. Schaadt, E. T. Yu, P. Waltereit, C. Poblenz, and J. S. Speck, Appl. Phys. Lett., **82**, 1293 (2003)

[37] R. Nakasaki, T. Hashizume, and H. Hasegawa, Physica E **7**, 953 (2000).

[38] S. F. Chichibu, A. C. Abare, M. S. Minsky, S. Keller, S. B. Fleischer, J. E. Bowers, E. Hu, U. K. Mishra, L. A. Coldren, and S. P. DenBaars, T. Sota, Appl. Phys. Lett. **73**, 2006 (1998).

[39] T. Takeuchi, C. Wetzel, S. Yamaguchi, H. Sakai, H. Amano, and I. Akasaki, Y. Kaneko, S. Nakagawa, Y. Yamaoka, and N. Yamada, Appl. Phys. Lett. **73**, 1691 (1998).

[40] P. Lefebvre, A. Morel, M. Gallart, T. Taliercio, J. Allègre, B. Gil, and H. Mathieu, B. Damilano, N. Grandjean, and J. Massies, Appl. Phys. Lett. **78**, 1252 (2001).

[41] Y. D. Jho, J. S. Yahng, E. Oh, and D. S. Kim, Appl. Phys. Lett. **79**, 1130 (2001).

[42] F. Renner, P. Kiesel, and G. H. Döhler, M. Kneissl, C. G. Van de Walle, and N. M. Johnson, Appl. Phys. Lett. **81**, 490 (2002).

[43] C. Y. Lai, T. M. Hsu, W.-H. Chang, and K.-U. Tseng, J. Appl. Phys. **91**, 531 (2002).

[44] G. L. Snider, computer program 1D Poisson/Schrödinger: A band diagram calculator, University of Notre Dame, Notre Dame, IN, 1995.

[45] L. Jia, E. T. Yu, D. Keogh, and P. M. Aspeck, Appl. Phys. Lett. **79**, 2916 (2001).

[46] J. Liu, Y. Zhou, J. Zhu, K. M. Lau, IEEE Electron Device Lett. **27**, 10 (2006).

[47] S. f. Chichibu, T. Sota, K. Wada, O. Brandt, K. H. Ploog, S. P. DenBaars, and S. Nakamura, Phys. Stat. Sol. (a) **183**, 91 (2001)

[48] L. T. Romano, B. S. Krusor, M. D. McCluskey, and D. P. Bour, Appl. Phys. Lett. **73**, 1757 (1998).

[49] C. Wetzel, T. Takeuchi, S. Yamaguchi, H. Katoh, H. Amano, and I. Akasaki, Appl. Phys. Lett. **73**, 1994 (1998).

[50] Ch. Manz, M. Kunzer, H. Obloh, A. Ramakrishnan, and U. Kaufmann, Appl. Phys. Lett. **74**, 3993 (1999).

[51] G. Martin, A. Botchkarev, A. Rockett, and H. Morkoc, Appl. Phys. Lett. **68**, 2541 (1996).

[52] G. Martin, S. Strite, A. Botchkarev, A. Agarwal, A. Rockett, and H. Morkoc, Appl. Phys. Lett., **65**, 610 (1994) .

[53] T.Makimoto, K. Kumakura, T. Nishida, and N. Kobayashi, Journal of Electronic Materials, **31**, 313 (2002).

[54] S. Rajan, P. Waltereit, C. Poblenz, S. J. Heikman, D. S. Green, J. S. Speck and U. K. Mishra, IEEE Electron Device Letters **25**, 247 (2004).

[55] J. W. P. Hsu, M. J. Manfra, R. J. Molnar, B. Heying and J. S. Speck, Appl. Phys. Lett. **81**, 79 (2002).

[56] J. W. P. Hsu, M. J. Manfra, D. V. Lang, S. Richter, S. N. G. Chu, A. M. Sergent, R. N. Kleiman, L. N. Pfeiffer and R. J. Molnar, Appl. Phys. Lett. **78**, 1685 (2001).

[57] J. E. Northrup, Appl. Phys. Lett. **78**, 2288 (2001).

[58] E. J. Miller, E. T. Yu, P. Waltereit and J. S. Speck, Appl. Phys. Lett. **84**, 535 (2004).

[59] B. Heying, I. Smorchkova, C. Poblenz, C. Elsass, P. Fini, S. DenBaars, U. Mishra, and J. S. Speck, Appl. Phys. Lett. **77**, 2885 (2000).

[60] E. Danielsson, C-M. Zetterling, M. Östling, A. Nikolaev, I. Nikitina, and V. Dmitriev, IEEE Trans. Electron. Dev. **48**, 444 (2001)

[61] J. M. Redwing, M. A. Tischler, J. S. Flynn, S. Elhamri, M. Ahoujja, R. S. Newrock, and W. C. Mitchel, Appl. Phys. Lett. **69**, 963 (1996)

[62] M. Lenzlinger and E. H. Snow, J. Appl. Phys. **40**, 278 (1969).

[63] Z. Weinberg, J. Appl. Phys. **53**, 5052 (1982).

[64] A. M. Witowski, K. Pakula, J. M. Baranowski, M. L. Sadowski and P. Wyder, Appl. Phys. Lett. **75**, 4154 (1999).

[65] Y. N. Xu and W. Y. Ching, Phys. Rev. B **48**, 4335 (1993).

[66] E. J. Miller, D. M. Schaadt, E. T. Yu, X. L. Sun, L. J. Brillson, P. Waltereit, and J. S. Speck, J. Appl. Phys. **94**, 7611 (2003).

[67] C. Chaneliere, J. L. Autran, S. Four, R. A. B. Devine, and B. Balland, J. Non-Crystalline Solids **245**, 73 (1999).

[68] J. R. Yeargan, and H. L. Taylor, J. Appl. Phys. **39**, 5600 (1968).

[69] J. G. Simmons, Phys. Rev. **155**, 657 (1967).

[70] A. S. Barker, Jr. and M. Ilegems, Phys. Rev. B **7**, 743 (1973).

[71] V. W. L. Chin, T. L. Tansley, and T. Osotchan, J. Appl. Phys. **75**, 7365 (1994).

[72] J. M. Langer and H. Heinrich, Phys. Rev. Lett. **55**, 1414 (1985).

[73] C. T. Foxon, S. V. Novikov, L. X. Zhao and I. Harrison, Appl. Phys. Lett. **83**, 1166 (2003).

[74] D. R. Hang, C. H. Chen, Y. F. Chen, H. X. Jiang, and J. Y. Lin, J. Appl. Phys. Lett. **90**, 1887 (2001).

[75] S. L. Rumyantsev, N. Pala, M. S. Shur, R. Gaska, M. E. Levinshtein, M. Asif Khan, G. Simin, X. Hu and J. Yang, J. Appl. Phys. **88**, 6726 (2000)

[76] B. S. Simpkins, E. T. Yu, P. Waltereit, and J. S. Speck, J. Appl. Phys. **94**, 1448 (2003)

[77] H. Zhang, E. J. Miller, and E. T. Yu, *J. Appl. Phys.* **99**, 023703 (2006).

[78] E. T. Yu, X. Z. Dang, L. S. Yu, D. Qiao, P. M. Asbeck, S. S. Lau, G. J. Sullivan, K. S. Boutros, and J. M. Redwing, *Appl. Phys. Lett.* **73**, 1880 (1998).

[79] D. M. Schaadt and E. T. Yu, unpublished.

[80] K. Shimojima and T. Suemitsu, J. Vac. Sci. Technol. B **21** (2), 698 (2003)

[81] J. B. Pendry, "Negative refraction makes a perfect lens", Phys. Rev. Lett. **85**, 3966 (2000)

[82] T. J. Yen, W. J. Padilla, N. Fang, D. C. Vier, D. R. Smith, J. B. Pendry, D. N. Basov, and X. Zhang, "Teraherz magnetic response from artificial materials", science **303**, 1494 (2004)

[83] V. M. Shalaev, W. Cai, U. K. Chettiar, H-K Yuan, A. K. Sarychev, V. P. Drachev, and A. V. Kildishev, "Negative index of refraction in optical metamaterials", Opt. Lett. **30**, 3356 (2005)

[84] C. Caloz and T. Itoh, "Novel microwave devices and structures based on the transmission line approach of meta-materials", IEEE MTT-S Int. Symp., Philadelphia, PA, June 2003, pp. 195-198

[85] N. Engheta, "An idea for thin subwavelength cavity resonators using metamaterials with negative permittivity and permeability," IEEE Antennas Wireless Propag. Lett., vol. 1, no. 1, pp.10—13, 2002.

[86] D. M. Pozar, "Microwave Engineering" Second Edition, chapter 1, 3, and 6, John Wiley and Sons, Inc., 1998.

[87] D. R. Smith and D. C. Vier, "Design of Metamaterials with Negative Refractive Index," Quantum Sensing and Nanophotonic Devices, Proc. Of SPIE Vol. 5359, pp. 52--63, 2004

[88] S. A. Ramakrishna, "Physics of negative refractive index materials," Rep. Prog. Phys. **68**, 449--251 (2005)

[89] J. B. Pendry, A. J. Holdent, D. J. Robbins, and W. J. Stewart, "Low frequency plasmons in thin-wire structures," J. Phys: Condens. Matter **10**, 4785--4809 (1999)

[90] J. Xiong and R. Janaswamy, "Is periodicity required for negative index materials," Antennas and Propagation Society International Symposium, vol. 3, 2004. IEEE pp. 3143--3146 (2004)

[91] H. Chen, L. Ran, D. Wang, J. Huangfu, Q. Jiang, and J. A. Kong, „Meatamaterial with randomized patterns for negative refraction of electromagnetic waves", Appl. Phys. Lett. **88**, 031908 (2006)

[92] T. J. Yen, W. J. Padilla, N. Fang, D. C. Vier, D. R. Smith, J. B. Pendry, D. N. Basov, and X. Zhang, "Supporting online materials," http://www.sciencemag.org/cgi/content/full/303/5663/1494/DC1

---

[93] B. E. A. Saleh, and M. C. Teich, “Fundamentals of Photonics,” chapter 6, John Wiley & Sons, Inc. 1991

[94] O. Stenzel, “The Physics of Thin Film Optical Spectra”, chapter 6, Springer-Verlag Berlin Heidelberg 2005

[95] N. Engheta, and R. W. Ziolkowski, “A positive future for double-negative materials,” IEEE Trans. Microw. Theory Tech., vol. 53, no. 4, pp. 1535—1556, April 2005